UC Santa Barbara
UC Santa Barbara Electronic Theses and Dissertations

Title

Water, energy, and carbon fluxes in dryland riparian ecosystems

Permalink

https://escholarship.org/uc/item/34s146f3

Author

Kibler, Christopher Linscott

Publication Date

2023

Peer reviewed|Thesis/dissertation

University of California
Santa Barbara

Water, energy, and carbon fluxes in dryland riparian ecosystems

A dissertation submitted in partial satisfaction
of the requirements for the degree

Doctor of Philosophy

in

Geography

by

Christopher Linscott Kibler

Committee in charge:

       Professor Dar A. Roberts, Chair
       Professor Kelly K. Caylor
       Professor Anna T. Trugman
       Professor Michael B. Singer, Cardiff University
       Professor John C. Stella, SUNY College of Environmental Science and Forestry

June 2023

The Dissertation of Christopher Linscott Kibler is approved.

_____

Professor Kelly K. Caylor

_____

Professor Anna T. Trugman

_____

Professor Michael B. Singer, Cardiff University

_____

Professor John C. Stella, SUNY College of Environmental Science and Forestry

_____

Professor Dar A. Roberts, Committee Chair

May 2023

Water, energy, and carbon fluxes in dryland riparian ecosystems

Copyright © 2023

by

Christopher Linscott Kibler

Acknowledgements

I would also like to thank my friends, family, and colleagues who have supported me throughout my doctoral research.

Curriculum Vitæ
Christopher Linscott Kibler

Education

2023	Ph.D. in Geography (Expected), University of California, Santa Barbara
2019	M.A. in Geography, University of California, Santa Barbara
2014	B.A. in Geography and International Affairs, The George Washington University

Professional Appointments

2018-2023	Graduate Student Researcher, University of California, Santa Barbara
2016-2023	Teaching Assistant, University of California, Santa Barbara
2014-2016	Environmental Protection Specialist, Government of the District of Columbia
2013-2014	Stormwater Management Intern, Government of the District of Columbia
2012	Legislative and Constituent Affairs Intern, National Oceanic and Atmospheric Administration

Publications

2021	Kibler, C.L., Schmidt, E.C., Roberts, D.A., Stella, J.C., Kui, L., Lambert, A.M., Singer, M.B. (2021). A brown wave of riparian woodland mortality following groundwater declines during the 2012–2019 California drought. *Environmental Research Letters*, 16(8), 084030.
2019	Kibler, C.L., Parkinson, A.M.L., Peterson, S.H., Roberts, D.A., D'Antonio, C.M., Meerdink, S.K., Sweeney, S.H. (2019). Monitoring Post-Fire Recovery of Chaparral and Conifer Species Using Field Surveys and Landsat Time Series. *Remote Sensing*, 11(24), 2963.

Research Grants

2021	Drought sensitivity of evapotranspiration and carbon uptake in riparian woodlands. *Future Investigators in NASA Earth and Space Science Technology*. Future Investigator. ($90,000)
2019	Satellite-based monitoring of water table dynamics and meteorological controls on groundwater recharge. *Groundwater Resources Association of California*. Principal Investigator. ($2,955)

Honors and Awards

2022	Jack Estes Memorial Award
2019	AGU Outstanding Student Presentation Award
2014	Phi Beta Kappa
2014	Gamma Theta Upsilon

Fields of Study

Major Field: Geography and Remote Sensing

Studies in Remote Sensing with Professor Dar Roberts

Studies in Ecological Modeling with Professor Anna Trugman

Studies in Ecohydrology with Professors Kelly Caylor, Michael Singer, and John Stella

Abstract

Water, energy, and carbon fluxes in dryland riparian ecosystems

by

Christopher Linscott Kibler

Riparian woodlands are hotspots of productivity and biodiversity on dryland landscapes, yet riparian tree species are also extremely vulnerable to catastrophic hydraulic damage caused by hydroclimatic change. Root zone water subsidies from shallow groundwater facilitate the high levels of productivity seen in riparian woodlands. Shallow groundwater provides a persistent source of root zone soil moisture that is somewhat decoupled from the local precipitation regime. As a result, riparian tree species are able to avoid water stress and maximize productivity throughout the prolonged summer dry seasons that are common in the southwestern United States. Groundwater declines caused by extreme drought conditions threaten the health and function of dryland riparian woodlands. If groundwater elevations drop below the root zones of riparian tree species, it is likely that riparian woodlands will experience widespread stress and mortality. However, the sensitivity of riparian tree species to changes in root zone water availability remains poorly constrained. This dissertation combines remote sensing, flux tower measurements, and ecological modeling to examine vegetation cover, evapotranspiration, and photosynthesis in riparian woodlands under changing environmental conditions. It also identifies critical physiological thresholds that are needed to maintain ecosystem structure and function under anthropogenic climate change.

In the first chapter, I combine remote sensing data with measurements from groundwater monitoring wells to identify critical groundwater thresholds that are needed to maintain the health and function of riparian woodlands. The analysis examines the

Santa Clara River in southern California, which experienced widespread groundwater declines during an extreme drought from 2012 to 2019. Spectral mixture analysis was used to estimate the fractional cover of green vegetation and non-photosynthetic vegetation (i.e., dead and woody plant material) in six riparian woodlands. The groundwater depth was characterized for each woodland using data from groundwater monitoring wells. The analysis revealed that riparian woodlands experience substantial decreases in green vegetation cover and substantial increases in dead/woody vegetation cover when the depth to groundwater exceeds *ca.* 5 m. The analysis also revealed a coherent spatial and temporal trend of riparian woodland mortality that proceeded downstream over six years and mirrored trends in groundwater elevation over space and time. The findings reveal that riparian woodlands depend on shallow groundwater access to maintain health and function, and that they experience substantial stress and mortality when they lose access to root zone water subsidies from shallow groundwater aquifers.

In the second chapter, I develop a novel theoretical model to predict leaf temperature as a function of evapotranspiration. The model reveals that the difference between leaf temperature and air temperature varies as a linear function of the evaporative fraction. The model also reveals that leaf temperature converges to air temperature when the evaporative fraction equals one. The model predictions were validated using flux tower measurements from a riparian woodland and an upland savanna in southeastern Arizona. The flux tower measurements reveal that evaporative cooling reduced leaf temperature by *ca.* 1-5 °C in the middle of the growing season. Evaporative cooling also resulted in a *ca.* 15% reduction in leaf respiration. The impact of evaporative cooling on leaf carbon cycling represents a novel connection between plant water and carbon cycles via leaf energy balance that has received little attention in literature.

In the third chapter, I develop a novel modeling framework to predict the vertical profiles of radiation and wind speed within forest canopies based on known physical

principles. The predictions are then used to estimate the vertical profiles of leaf temperature and net photosynthesis for five flux tower sites spanning a large latitudinal gradient in North and South America. The model predictions reveal that leaf temperature decreases exponentially downward through forest canopies, and that the difference between top-of-canopy leaf temperature and bottom-of-canopy leaf temperature can exceed 7 ℃. Unexpectedly, in many forest biomes, the highest levels of net photosynthesis often occur in the middle of the canopy. The analysis helps uncover the mechanistic basis for this behavior. The analysis also identifies the combinations of environmental conditions that result in critical leaf temperatures that cause irreversible damage to leaf photosynthetic infrastructure. Two different data sets provide evidence of trait coordination between leaf size and stomatal conductance to avoid critical leaf temperatures across global forest biomes.

Contents

Introduction

Dryland riparian tree species pose an interesting paradox in plant function: they are extremely vulnerable to water stress and drought-induced mortality, and they often grow in regions where there is no precipitation throughout the summer growing season, yet they are also among the most productive plant communities in semi-arid and arid ecosystems (Leffler et al., 2000; Lite and Stromberg, 2005; Dybala et al., 2019). Access to groundwater plays a critical role in maintaining the structure and function of dryland riparian woodlands (Shafroth et al., 2000). Riparian corridors form in zones of hydrological convergence where hillslope runoff accumulates in shallow groundwater aquifers that drive streamflow (Jencso and McGlynn, 2011). Groundwater aquifers then provide riparian trees with a persistent source of root zone moisture that is somewhat decoupled from the local precipitation regime (Sargeant and Singer, 2016). Consistent groundwater access enables riparian tree species to maintain relatively high levels of water and carbon uptake, even under stressful climate conditions when upland plants are forced to downregulate their physiological function (Singer et al., 2013). As a result, riparian woodlands typically exhibit higher levels of leaf area index, vegetation cover, and canopy height than comparable upland vegetation (Swetnam et al., 2017; Dybala et al., 2019). For these reasons, dryland riparian woodlands are biodiversity hotspots (Stromberg et al., 1996), and riparian trees themselves create microclimates that enhance the biodiversity of other plant and animal species (e.g., Kus, 1998; Bateman and Merritt, 2020).

While many dryland plant species are well adapted to seasonal and inter-annual drought conditions, dryland riparian tree species are especially vulnerable to hydroclimatic change (Pivovaroff et al., 2018). Riparian tree species experience catastrophic xylem cavitation at relatively mild levels of water stress (i.e., xylem water potentials close to zero), so they can experience whole-plant mortality if water subsidies from groundwater are no longer available (Leffler et al., 2000). Riparian tree species have developed several adaptations to cope with water stress. Over short time scales, they can close their stomata to reduce transpirational water loss and relieve pressure gradients in the xylem (Pivovaroff et al., 2018). Over longer time scales they can also reduce leaf area, shed branches, and reduce canopy size, which have similar effects but incur substantial carbon costs during post-drought recovery (Rood et al., 2003). If the functional and structural responses to drought stress are inadequate to raise xylem water potentials above critical values, or if photosynthetic assimilation cannot keep pace with the construction costs of new tissue during post-drought recovery, trees are likely to experience whole-plant mortality (Tai et al., 2018; Trugman et al., 2018). Riparian woodlands are comprised of co-occurring species that have similar functional traits, and groundwater declines often occur across entire subbasins, so the mortality of riparian trees often does not occur in isolation (Stromberg et al., 1996). Rather, entire woodlands are vulnerable to simultaneous mortality as soon as critical subsurface water subsidies are no longer available (Amlin and Rood, 2003).

Extreme drought conditions are becoming more prevalent in the southwestern United States due to anthropogenic climate change, which will likely increase the frequency of water stress in riparian woodlands (Diffenbaugh et al., 2015; Williams et al., 2020). Climate change-type droughts are characterized by higher air temperatures, which increases the vapor pressure deficit and accelerates the flux of water from the land surface into the atmosphere(Breshears et al., 2005; Williams et al., 2020). Shifts in the frequency

and intensity of precipitation events can also affect ecosystem water availability, but the impacts of climate change on precipitation regimes are less well constrained (Berg and Hall, 2015; Diffenbaugh et al., 2015). Increased upland evapotranspiration depletes soil moisture more quickly, which reduces hillslope runoff and ultimately reduces groundwater recharge (Meixner et al., 2016; Warter et al., 2021). Dry upland conditions can cause widespread depletion of groundwater aquifers, which causes the water table to decline and reduces the subsurface water subsidy that is available to riparian trees (Tai et al., 2018). Under extreme drought conditions, the root zones of riparian tree species can become completely disconnected from the water table, which would likely cause widespread tree mortality in riparian woodlands (Lite and Stromberg, 2005). Even at intermediate levels of water stress, reduced root zone water availability can cause declines in evapotranspiration and photosynthesis that reduce ecosystem productivity (Cooper et al., 2003; Pettit and Froend, 2018). Persistent drought conditions may also cause gradual shifts in ecosystem structure and function, which could compromise the ability of riparian woodlands to serve as productivity hotspots and foster plant and animal biodiversity on dryland landscapes (Stromberg et al., 1996; Stromberg and Merritt, 2016).

Several attributes of dryland riparian woodlands have made them difficult to study. First, the spatial extent of riparian woodlands is often limited to narrow strips of floodplain immediately adjacent to active river channels. Many riparian woodlands are only tens of meters wide, which makes it difficult to isolate signals from riparian trees species in observational data sets. For example, many spaceborne remote sensing platforms have spatial resolutions of *ca.* 30 m in the visible-infrared wavelengths and *ca.* 100 m in the thermal wavelengths. Native spatial resolutions can be even coarser when an image is acquired off-nadir. As a result, many remote sensing images of riparian woodlands contain mixed pixels that are affected by land cover from adjacent upland vegetation and riparian alluvium. Likewise, eddy covariance sensors typically have fetches that are

3

ca. 200 m wide (Chu et al., 2021). This limits the utility of eddy covariance sensors in riparian ecosystems, where the water and carbon flux signals would often be affected by adjacent upland vegetation and evaporation directly off of the river channel (but see Scott et al. 2004; Missik et al. 2021). Riparian woodlands are also difficult to study because the interaction between tree root systems and shallow groundwater aquifers plays a critical role in regulating physiological function, yet subsurface root and water dynamics are notoriously difficult to measure. Many studies have relied on opportunistic measurements such as cut banks to estimate the rooting depths of riparian trees species (Rood et al., 2011; Stromberg, 2013), but riparian tree species exhibit a substantial amount of intraspecific plasticity in rooting depth in response to local groundwater conditions (Stella and Battles, 2010; Williams et al., 2022). Similarly, shallow groundwater elevation can exhibit a substantial amount of variability over very fine spatial and temporal scales. Subsurface groundwater fluxes are affected by hillslope runoff, anthropogenic and natural groundwater abstraction, basin geomorphology, localized bedrock intrusions, river regulation, and floodplain soil properties (Downs et al., 2013; Singer et al., 2014). The interactions between these factors can result in dramatic changes in shallow groundwater elevation over spatial scales as small as hundreds of meters (e.g., Amlin and Rood, 2003; Cooper et al., 2003).

Despite the functional importance of riparian woodlands and their well-established dependence on shallow groundwater availability, the sensitivity of riparian tree species to groundwater declines remains poorly constrained. Additional research is needed to identify the critical groundwater thresholds that cause the mortality of riparian tree species. Likewise, little is known about how the evapotranspiration and photosynthesis of riparian tree species change under stressful but not lethal environmental conditions. This dissertation will fill these research gaps. It will primarily examine two riparian ecosystems in the southwestern United States, which have contrasting hydroclimatic

4

regimes. The first study system is the Santa Clara River, which flows through Los Angeles and Ventura counties in southern California. It is a large multi-use watershed that supports agriculture, urban development, and remnant natural ecosystems. The region receives most of its annual precipitation in the winter, when winter deciduous riparian tree species are dormant. Shallow groundwater aquifers are thus critical for facilitating root zone water availability during the dry summer growing season (Downs et al., 2013; Beller et al., 2016). The second study system is the San Pedro River, which has its headwaters in northern Mexico and primarily flows through southeastern Arizona. The river's water resources are also subject to anthropogenic influences, but a large portion of the river's ecosystems are protected from development by the San Pedro River National Conservation Area (Lite and Stromberg, 2005). The region has two wet seasons that provide water for riparian woodlands during both the dormant and growing seasons. The first wet season occurs in December and January as a result of cyclonic Pacific frontal storms. The second wet season occurs from July through September as a result of the North American monsoon. The driest period of the year often occurs in May and June before the onset of the monsoon (Higgins et al., 1997; Arizpe et al., 2020). Nonetheless, groundwater still serves an important water source for riparian tree species throughout the growing season (Scott et al., 2004; Mayes et al., 2020). I will also examine data from several other ecosystems, including an upland savanna, a boreal aspen forest, two temperature deciduous forests, and a tropical rainforest, in order to constrain the mechanistic drivers of plant physiological function under varying climatic conditions.

The goals of the research presented in this dissertation are twofold. The first goal is to quantify the sensitivity of vegetation cover, evapotranspiration, and photosynthesis in dryland riparian woodlands to changes in root zone water availability. This is achieved by synthesizing spaceborne, airborne, and tower-based remote sensing with *in situ* sensor measurements of groundwater elevation, soil moisture, and ecosystem energy fluxes. The

second goal is to develop generalizable theoretical models that connect ecosystem energy fluxes with plant physiological function. Specifically, I analyze the relationship between evapotranspiration and leaf temperature, which serves as a critical control on the rates of leaf biochemical reactions, including photosynthesis and respiration. The models are validated, where possible, with flux tower measurements, and they reveal a novel connection between plant water and carbon cycles via leaf energy balance that has not been extensively explored in literature.

The dissertation is organized as follows. In the first chapter, I quantify the sensitivity of dryland riparian tree species to groundwater declines during extreme drought conditions. The work aims to identify a critical threshold of groundwater depth below which riparian tree species cannot survive. The analysis examines riparian woodlands in the floodplain of the Santa Clara River, which experienced an extreme drought from 2012 to 2019 that caused pronounced groundwater declines. The analysis combines remote sensing data about plant health with groundwater depth data from groundwater monitoring wells. Spectral mixture analysis was used to estimate the fractional cover of green vegetation, dead/woody vegetation, and soil in six riparian woodlands. The land cover fractions were then compared to spatially and temporally explicit estimates of groundwater depth in each woodland, which revealed the sensitivity of woodland vegetation cover to groundwater declines.

In the second chapter, I examine how transpiration regulates leaf temperature and respiration in dryland tree species. The first part of the analysis develops a novel theoretical model to predict leaf temperature as a function of leaf energy fluxes. The model is then validated using measurements from two eddy covariance towers in Arizona, USA, which measure stands of *Prosopis velutina* growing in a riparian woodland and an upland savanna. The leaf temperature model is then used to estimate changes in leaf respiration that are attributable to evapotranspiration variability.

In the third chapter, I develop a novel model to predict the vertical profiles of leaf temperature and net photosynthesis within forest canopies. The vertical profiles of radiation and wind speed are modeled as a function of cumulative leaf area index based on known physical principles. The radiation and wind speed data are then used to force the leaf temperature model developed in the second chapter and a mechanistic model of net photosynthesis. The model predictions reveal the estimated vertical profiles of leaf temperature and net photosynthesis based on top-of-canopy measurements. The novel modeling framework is used to analyze data from five flux towers spanning global forest biomes, including a dryland riparian woodland, a boreal aspen forest, two temperature deciduous forests, and a tropical rainforest. The model predictions are also compared to published data sets of leaf size and leaf temperature to assess the feasibility of the model predictions.

Collectively, the three chapters provide new insights into the mechanistic basis for changes in plant physiological function in riparian woodlands, especially in response to shifting root zone water availability. Many of the insights and models are also generalizable to other forest biomes, and they can be used to improve predictions of water and carbon cycling in terrestrial ecosystems under anthropogenic climate change.

Chapter 1

A brown wave of riparian woodland mortality following groundwater declines during the 2012-2019 California drought

1.1 Introduction

Riparian trees often rely on shallow groundwater to meet their water needs, so water table declines during increasingly frequent and severe drought conditions threaten the health and function of riparian woodlands (Diffenbaugh et al., 2015; Meixner et al., 2016; Rohde et al., 2017; Williams et al., 2020). Though many studies have examined the sensitivity of individual species to drought and local groundwater availability (e.g., Stromberg et al., 1996; Singer et al., 2014; Sargeant and Singer, 2016; Pettit and Froend, 2018; Skiadaresis et al., 2021), few studies have considered the landscape-scale responses of riparian woodlands to drought across space and time, and even fewer in relation to

direct groundwater measurements (but see Rohde et al., 2017). These knowledge gaps are relevant to dryland watersheds around the globe, where convergent pressures on water resources from agriculture, urban development, and climate change are increasing (Taylor et al., 2013; Rohde et al., 2017; Rateb et al., 2020).

Riparian woodlands are ecologically important plant communities that provide habitat for sensitive animal species (Kus, 1998; Merritt and Bateman, 2012; Bateman and Merritt, 2020), promote plant biodiversity (Stromberg et al., 1996; Stromberg and Merritt, 2016), and contain a disproportionately large amount of the biomass in dryland watersheds (Swetnam et al., 2017; Matzek et al., 2018; Dybala et al., 2019). They form in convergent topographic zones, which serve as hydrologic refugia and are somewhat buffered from normal climatic variability (Brooks et al., 2015; Hoylman et al., 2019). Riparian tree species are typically phreatophytes, which have taproot systems that extend up to 5 m down to the capillary fringe above perennial water tables (Stromberg, 2013; Rohde et al., 2017). Phreatophytes are extremely sensitive to water availability at all life stages (Mahoney and Rood, 1998; Stella et al., 2010; Singer et al., 2013). If their root systems lose contact with the alluvial water table, phreatophytes commonly exhibit stomatal closure, leaf abscission, branch dieback, and xylem cavitation (Scott et al., 1999; Leffler et al., 2000; Rood et al., 2000). Prolonged water table declines, for example during extreme drought conditions, can lead to whole-plant mortality if a tree's hydraulic system cannot maintain a favorable water balance as groundwater supply declines (Scott et al., 1999; Cooper et al., 2003).

From 2012 to 2019, California experienced the most severe drought in its paleoclimate record (Robeson, 2015). Meteorological drought conditions first emerged in northern California around January 2012 and then spread southward (U.S. Drought Monitor, 2021). The meteorological drought propagated into hydrological (Van Loon, 2015) and ecological (Kovach et al., 2019; Munson et al., 2020) droughts in dryland regions throughout

southern California (Okin et al., 2018; Dong et al., 2019; Warter et al., 2021). Record low precipitation and record high temperatures (Diffenbaugh et al., 2015) substantially reduced soil moisture (Warter et al., 2021), streamflow (Konrad et al., 2021), groundwater storage (Thomas et al., 2017), and upland canopy water content (Asner et al., 2016) throughout the region. While the drought is known to have generated mass die-off of upland trees (e.g., Goulden and Bales, 2019), there is a notable lack of quantitative assessments of drought-induced mortality of lowland riparian phreatophytes, particularly within dryland regions. Documenting large-scale ecological die-offs, particularly in ecosystems that are buffered from climate impacts by their hydrogeomorphic setting, is important for identifying global signals of forests being pushed past their tolerance for environmental change (Allen et al., 2010; Anderegg et al., 2013; Allen et al., 2015; McDowell et al., 2016).

Remote sensing is a powerful tool for analyzing the sensitivity of vegetation health to changes in the water availability, but few remote sensing studies have quantified the sensitivity of groundwater-dependent ecosystems to water table declines (e.g., Barron et al., 2014; Huntington et al., 2016). In this study, we combined time series remote sensing imagery with data from groundwater monitoring wells to investigate the fate and trajectory of riparian woodlands in southern California during the unprecedented 2012-2019 California drought. We used spectral mixture analysis to discriminate between healthy and dead vegetation cover in remote sensing imagery. We then analyzed the relationship between vegetation cover and depth to groundwater (DTG) in a range of woodland stands that represent a gradient of groundwater availability. These data enabled us to characterize the trajectory and the spatial progression of drought impacts across an ecologically and economically important river corridor, and to monitor the initial drought recovery in the riparian woodlands.

1.2 Methods

1.2.1 Study area

The Santa Clara River flows 132 km from the Mojave Desert to the Pacific Ocean and has a catchment covering 4,200 km^2 in Ventura and Los Angeles Counties, California (Beller et al., 2016). Mean annual precipitation ranges from 200–800 mm, with the wettest regions at high elevations (catchment relief 2,700 m) and near the coast (Downs et al., 2013). The basin has a Mediterranean climate with cool, wet winters and warm, dry summers, and many reaches of the Santa Clara River are ephemeral (i.e., flowing only part of most years). Winter rainfall produces flashy flows, and more than half of the annual discharge occurs during a small number of precipitation events (Downs et al., 2013; Beller et al., 2016). The river corridor has been subject to extensive urban and agricultural development over the last century, but the main stem of the river has not been severely controlled by engineering structures, making it the largest river in southern California that is mostly free flowing (Downs et al., 2013; Beller et al., 2016).

The native riparian woodlands along the Santa Clara River are discontinuous, existing at locations where groundwater is close to the surface under normal conditions (Beller et al., 2016). The riparian woodlands are dominated by phreatophytic tree and shrub species, including *Populus fremontii*, *P. trichocarpa*, *Salix laevigata*, *S. lasiolepis*, and *S. exigua*. The roots for these species are typically concentrated in the top 2 m of the soil profile (Table 1; TNC, 2021), although phreatophytes exhibit a considerable degree of plasticity in rooting depth in response to local groundwater conditions (Shafroth et al., 2000; Rood et al., 2011).

Table 1.1: Rooting depths for tree and shrub species that are prevalent in riparian woodlands in the Santa Clara River floodplain.

Species	Rooting Depth (m)	Source
Populus fremontii	1.4 (max)	Shafroth et al. (2000)[a]
Populus fremontii	2.1+ (max)	Zimmerman (1969)
Populus fremontii	0.8 (max)	Rood et al. (2011)
Populus trichocarpa	0.65 (max)	Rood et al. (2011)
Salix laevigata	1+ (max)	Stover et al. (2018)
Salix exigua	0.51 (min)	(USDA, 2021)
Baccharis salicifolia	0.3 (min)	(USDA, 2021)
Baccharis salicifolia	0.6 (max)	Gary (1963), Stromberg (2013)

[a] Study that measured three-year-old saplings

1.2.2   Study sites

We identified six stands of *Populus-Salix* riparian woodlands in the lower Santa Clara River floodplain that are thought to be supported by perennial shallow aquifers (Figure 1.1; Beller et al., 2016). The woodlands range in area from 7-120 ha, and they represent the most substantial woodlands that were present before the 2012-2019 drought (Beller et al., 2016). The study sites are distinguished by transitions in hydrology or river management that facilitate shallow groundwater depths. Site boundaries were manually digitized in GIS software using 2012 aerial imagery acquired by the National Agricultural Imagery Program (USDA, 2012).

1.2.3   Depth to groundwater

We calculated DTG at each of the study sites using measurements from nearby wells acquired from the California Department of Water Resources, United Water Conservation District, and the County of Ventura. We also used unpublished data from shallow monitoring wells that were installed by members of our team at two of the study sites (Tables S1-S2; Figures S1-S4). The shallow wells are 3 m deep and were installed between 2015 and 2020. They are manually measured twice per month. We used two different
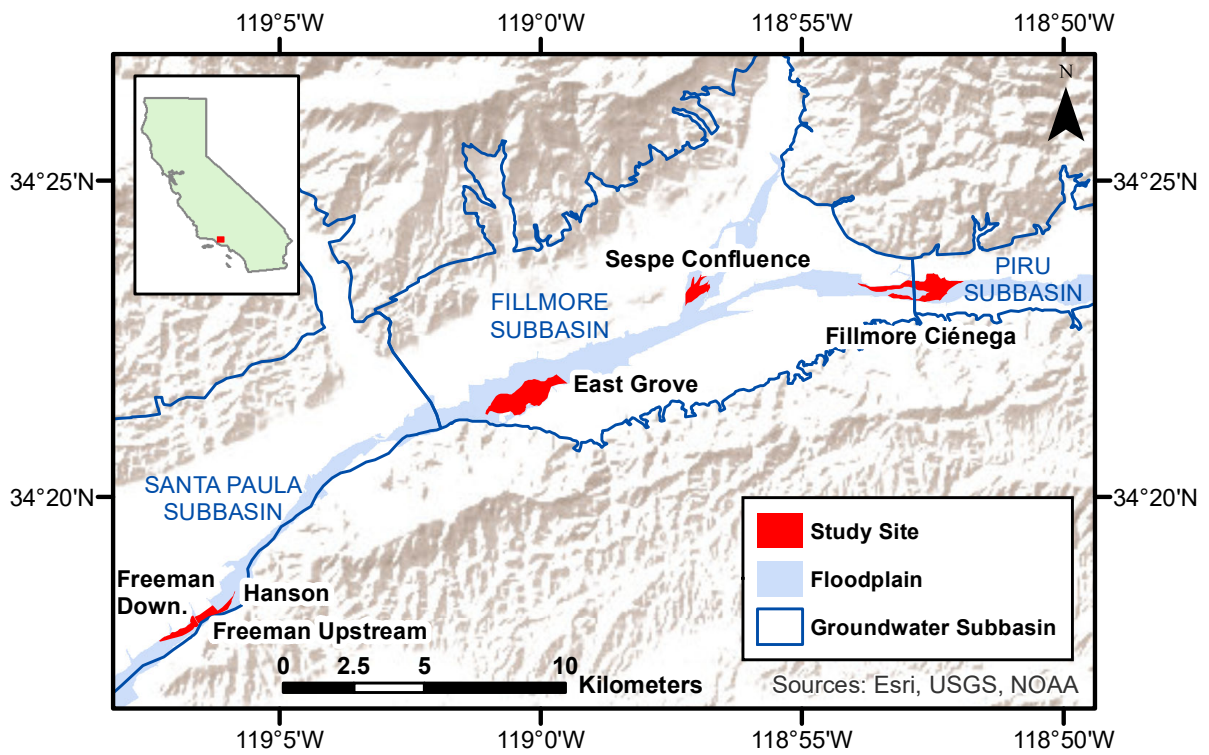
Figure 1.1: Location of the study sites in the floodplain of the Santa Clara River, California, USA. The river flows from east to west.

protocols to calculate DTG at the study sites, depending on the well data availability for each site (see Appendix A).

1.2.4 Remote sensing data acquisition and processing

Spectral mixture analysis (SMA) was used to map the fractional cover of green vegetation (GV), non-photosynthetic vegetation (NPV; i.e., dead and woody plant material), and soil in the Santa Clara River floodplain (Smith et al., 1990; Roberts et al., 1998). The SMA model was calibrated using data from the Airborne Visible/Infrared Imaging Spectrometer (Green et al., 1998) and in situ spectra (see Appendix A). We analyzed Landsat images (spatial resolution of 30 m) acquired every June between 2011 and 2018. The June 2011 image provides a pre-drought baseline (U.S. Drought Monitor, 2021). The June 2012-2018 images capture all of the growing seasons during the drought. Data from 2012 were omitted because of the scan line corrector failure on Landsat 7 (Markham et al., 2004). The SMA model generated estimates of the fractional cover of GV, NPV, and soil within each pixel for each image. While the SMA method did not classify species cover, qualitative observations of species cover were made during field visits to the sites between 2017 and 2021, and by manually examining high resolution aerial imagery captured before, during, and after the drought.

1.2.5 Analysis of drought effects on vegetation

The fractional cover data and the groundwater data were used to conduct two analyses. First, the GV and NPV fractions were used to examine the spatial and temporal trends of woodland mortality along the river corridor. Mortality was indicated by a decrease in GV fractions and an increase in NPV fractions (Huang et al., 2019). Significant differences in land cover fractions for each study site across time were identified using a

Kruskal-Wallis test and a post-hoc Dunn's test with a Holm adjustment ($\alpha = 0.05$).

Second, we quantified the sensitivity of GV and NPV fractions to DTG. The median GV and NPV fractions were calculated for each study site and each year. We used the DTG measurements that were closest in time to the Landsat image acquisition dates. The difference between the well measurement dates and the image acquisition dates ranged from 0 days to 36 days with a median of 13 days. The sensitivity analyses were divided into two distinct time spans. The first time span was limited to data from 2011 to 2016, representing the period when the drought became progressively more severe, as evidenced by increasing DTG, below-average soil moisture (Warter et al., 2021), and decreasing SPEI. The 2011-2016 observations were pooled across sites and years, and mixed effect logistic-binomial regression (Gelman and Hill, 2007) was used to determine if DTG is a significant predictor of GV and NPV fractions. Site was included as a random effect in the models to account for local influences on the vegetation unrelated to groundwater (see Appendix A).

The second time span was limited to data from 2017 and 2018, which represents a period of early drought recovery in the riparian woodlands. Substantial rainfall in the winter of 2016-2017 reduced DTG and increased soil moisture in the region (Warter et al., 2021). As a result, the ecological drought began to subside, even though meteorological drought conditions persisted until 2019. The sensitivity of an ecological response to an environmental driver often differs based on the direction of the change. Differing sensitivities during decline and recovery phases can result in hysteresis in ecological systems (Beisner et al., 2003; Andersen et al., 2009). The 2017-2018 data were used to determine if there were differences in the sensitivity to DTG during the early stages of drought recovery as compared to the drought onset years of 2011-2016. The observed land cover fractions from 2017 and 2018 were compared to the values predicted by the regression model that was calibrated using data from 2011-2016. This indicated whether sensitivity
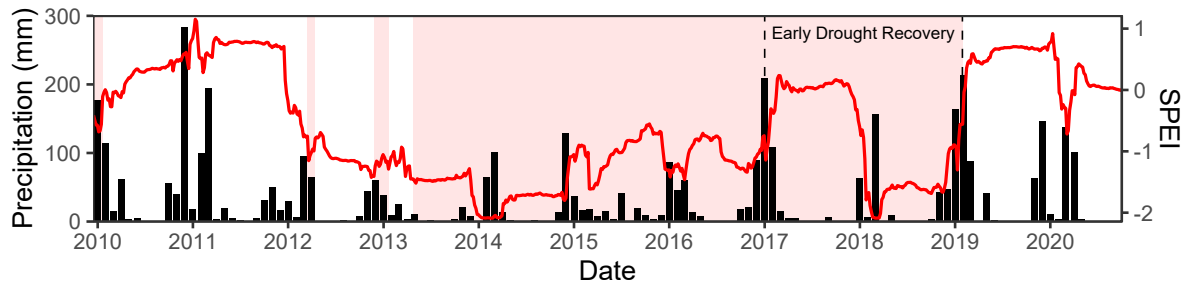
Figure 1.2: Mean monthly precipitation (black bars) and 12-month Standardized Precipitation Evaporation Index (SPEI; red line) in the Santa Clara River watershed (Abatzoglou, 2013; Huntington et al., 2017). The red shading indicates periods of drought according to the U.S. Drought Monitor (2021). The date labels indicate January 1 of each year.

to DTG differed during the two phases. Mean absolute error (MAE) was used to quantify the difference between the observed and predicted values during the two phases.

1.3 Results

1.3.1 Drought timeline

The Santa Clara River watershed experienced moderate drought conditions throughout much of 2012 and consistently experienced severe drought conditions starting in June 2013 (Figure 1.2; U.S. Drought Monitor, 2021). Rainfall in the winter of 2016-2017 provided some drought relief, but severe drought conditions returned in 2018 (U.S. Drought Monitor, 2021). Persistent rainfall from a series of atmospheric rivers (Sumargo et al., 2021) ended the drought in the winter of 2018-2019. Standardized Precipitation Evaporation Index (Vicente-Serrano et al., 2010) values generally remained positive after February 2019, and the U.S. Drought Monitor, a composite drought index, also indicated that the drought ended in February 2019.

1.3.2   Groundwater level changes during and after drought

In 2011, maximum DTG at the six study sites ranged from 1.1 to 4.4 m. The DTG increased (i.e., the water table declined) at all six study sites between 2011 and 2016, but there was substantial spatial and temporal variability in DTG along the river corridor (Figure 1.3; Table S3). The changes in DTG were mediated by the interaction between climatic forcings and basin geomorphology. The Fillmore Ciénega site sits at the boundary of the Piru and Filmore groundwater subbasins (Figure 1.1), where the deposits of permeable alluvium become substantially narrower and shallower and force groundwater to the surface (Mann, 1958; Reichard et al., 1999). Surface flow between the Piru and Fillmore subbasins decreased between 2011 and 2013 and stopped between 2014 and 2016 (United Water Conservation District, 2017). As a result, shallow lateral recharge of the Fillmore subbasin was likely reduced or eliminated during the peak of the drought. Maximum DTG at Fillmore Ciénega and Sespe Confluence increased by 11.9 m and 12.7 m, respectively, between 2011 and 2016 as groundwater in the Fillmore subbasin was depleted. At the downstream end of the Fillmore subbasin, groundwater elevations were more stable. The East Grove site sits at the boundary of the Fillmore and Santa Paula subbasins, where constrictions in the deposits of unconsolidated alluvium again force groundwater to the surface (Reichard et al., 1999). Maximum DTG at the East Grove site only increased by 0.9 m between 2011 and 2016. Surface flow at the boundary between the Fillmore and Santa Paula subbasins did not approach zero until 2016 (UWCD, 2017). The Hanson, Freeman Upstream, and Freeman Downstream sites are located in the Santa Paula subbasin, where the shallow aquifer sits on top of impermeable deposits that prevent groundwater from percolating into deeper aquifers (Reichard et al., 1999; Hanson et al., 2003). Groundwater elevations in the Santa Paula subbasin remained relatively stable throughout the drought. At Hanson, Freeman Up-

stream, and Freeman Downstream, maximum DTG increased by 3.5 m, 3.0 m, and 5.0 m (respectively) between 2011 and 2016. In 2016, maximum DTG at the six sites ranged from 2.0 to 17.1 m. Substantial rainfall in the winter of 2016-2017 reversed groundwater trends and caused DTG to decrease (i.e., the water table rose) at all study sites, but some sites did not approach pre-drought DTG until 2019.

1.3.3 Vegetation cover change during drought

Several riparian woodlands exhibited large decreases in GV cover and large increases in NPV cover from 2011 to 2016, indicating widespread drought-induced mortality (Figure 1.4, Tables S4-S6). Fillmore Ciénega and Sespe Confluence exhibited the largest decreases in GV fractions and the largest increases in NPV fractions. Sites farther downstream were less affected by the drought and experienced smaller changes in land cover.

There was a distinct spatial pattern and temporal trend of woodland mortality that occurred both within and across study sites in the Fillmore subbasin (Figure 1.5). Widespread mortality first occurred in 2013 at the most upstream study site, Fillmore Ciénega (Figure S5). A wave of mortality then traveled 13 km west (downstream) across the Fillmore subbasin between 2013 and 2016. The wave of mortality can be seen within and across individual study sites, and it is especially distinct within the Fillmore Ciénega site. By 2015, the wave of mortality reached the area immediately upstream of the East Grove site (Figure S6). By 2016, all three areas had experienced widespread mortality, and the Fillmore Ciénega and Sespe Confluence sites experienced near-complete mortality of their riparian woodlands. Sites in the downstream Santa Paula subbasin were relatively stable throughout the drought, and no distinct spatial pattern of woodland mortality in the Santa Paula subbasin was observed (Figure S7).
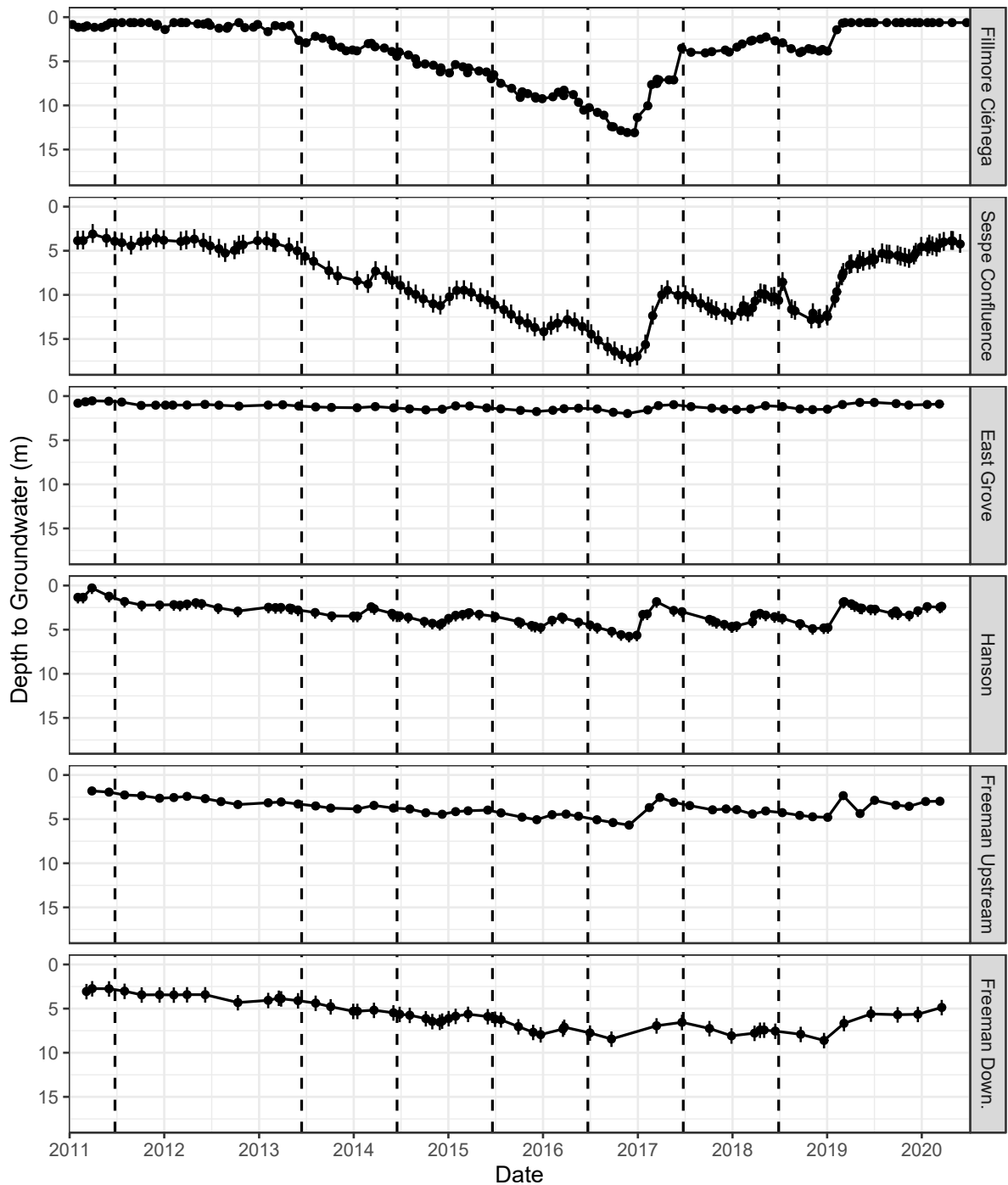
Figure 1.3: Mean DTG from 2011 to 2020 for each study site. The vertical bars represent the interquartile range of DTG for sites where DTG was measured by a single shallow well (see Appendix A). The dashed vertical lines indicate the remote sensing image acquisition dates. The date labels indicate January 1 of each year.
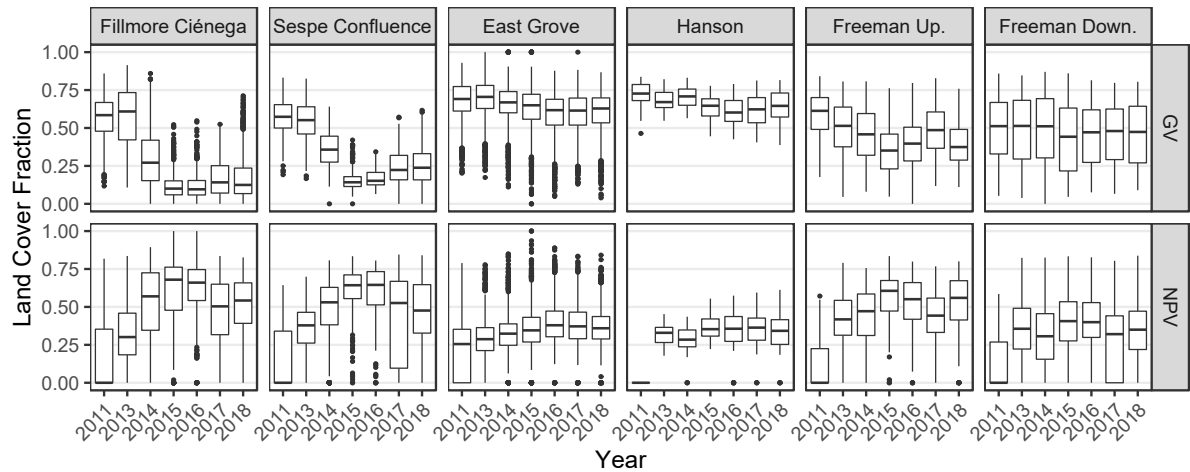
Figure 1.4: Box plots of green vegetation (GV) fractions and non-photosynthetic vegetation (NPV) fractions for each study site from 2011 to 2018. Note that 2012 data are omitted (see text).

1.3.4 Groundwater declines and plant health

DTG was significant predictor of the GV and NPV fractions for 2011-2016 (Table 2). There was a significant negative relationship between DTG and the GV fractions (p <0.001; Figure 1.6a), indicating that green vegetation decreased as the water table declined. There was also a significant positive relationship between DTG and the NPV fractions (p <0.001; Figure 1.6b), indicating that dead and woody plant cover increased as the water table declined. Taken together, these remote sensing metrics indicate leaf shedding, increased litter, exposed branches, and, in some cases, complete mortality as the drought progressed (Adams et al., 1995).

1.3.5 Site-based differences in early drought recovery

We also compared the 2017-2018 GV fractions to the values that were predicted by the regression model, which was calibrated using data from 2011-2016. This revealed whether the sensitivity to DTG differed during the decline and recovery phases. The 2017-2018
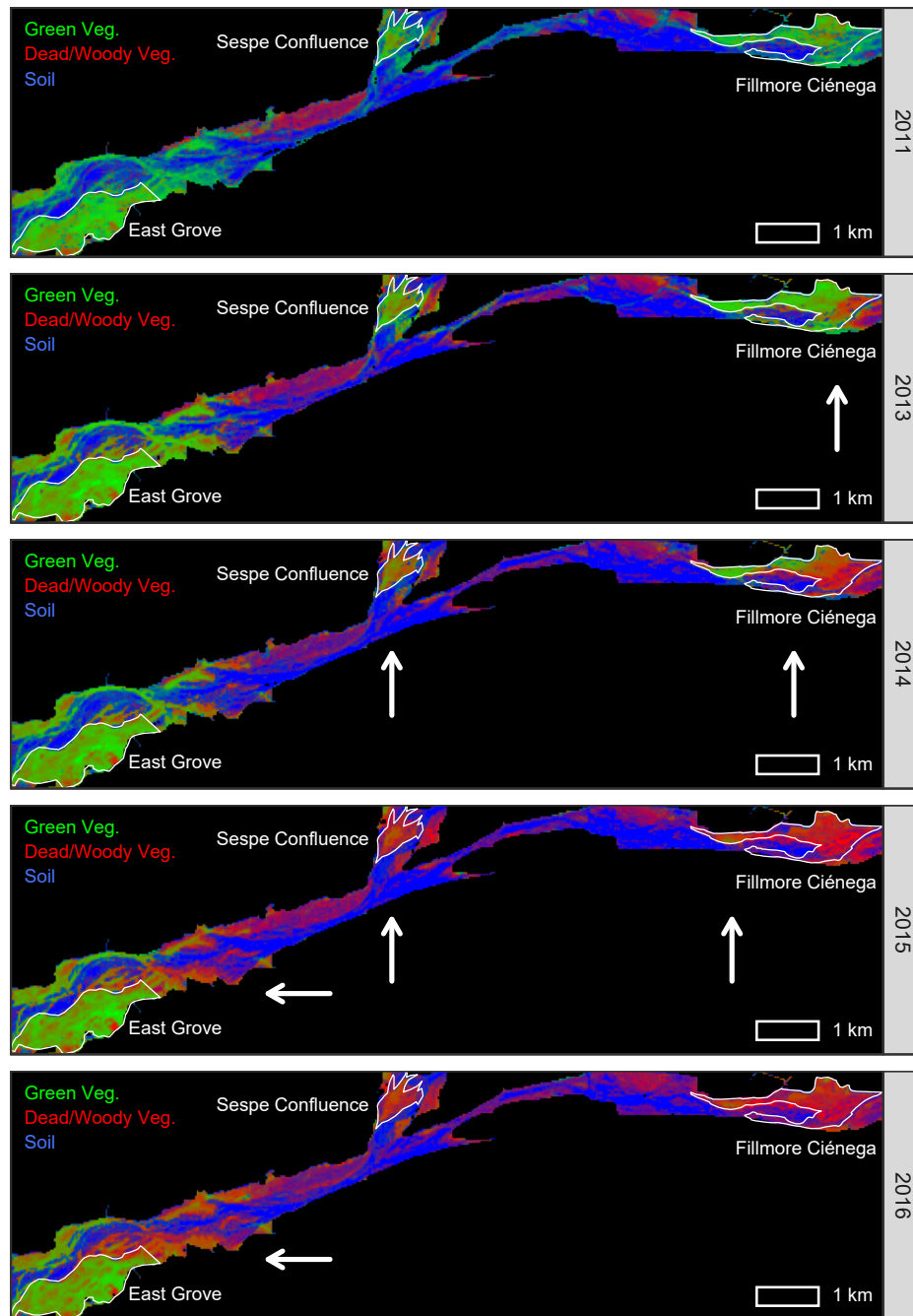
Figure 1.5: Remote sensing model outputs of floodplain land cover in the Fillmore subbasin from 2011 to 2016. The study sites are outlined in white, and the white arrows indicate areas experiencing notable dieback in particular years. The river flows from right to left. A comparable figure for the Hanson, Freeman Upstream, and Freeman Downstream sites is included in Appendix A (Figure S7).

21

Table 1.2: Mixed effect logistic-binomial regression results for models assessing the relationship between DTG and GV fractions and between DTG and NPV fractions from 2011 to 2016. Site was included as a random effect in the models. The values in parentheses indicate the standard errors of the regression coefficients.

	GV	NPV
FIXED EFFECTS		
Intercept	1.02 ***	-2.09 ***
	(0.16)	(0.28)
DTG	-0.24 ***	0.33 ***
	(0.01)	(0.01)
RANDOM EFFECTS		
	Std. Dev	Std. Dev
Site (Intercept)	0.38	0.68
MODEL		
N	30	30
N (site)	6	6
Pseudo-R^2 (fixed)	0.16	0.24
Pseudo-R^2 (total)	0.19	0.33
		*** $p < 0.001$
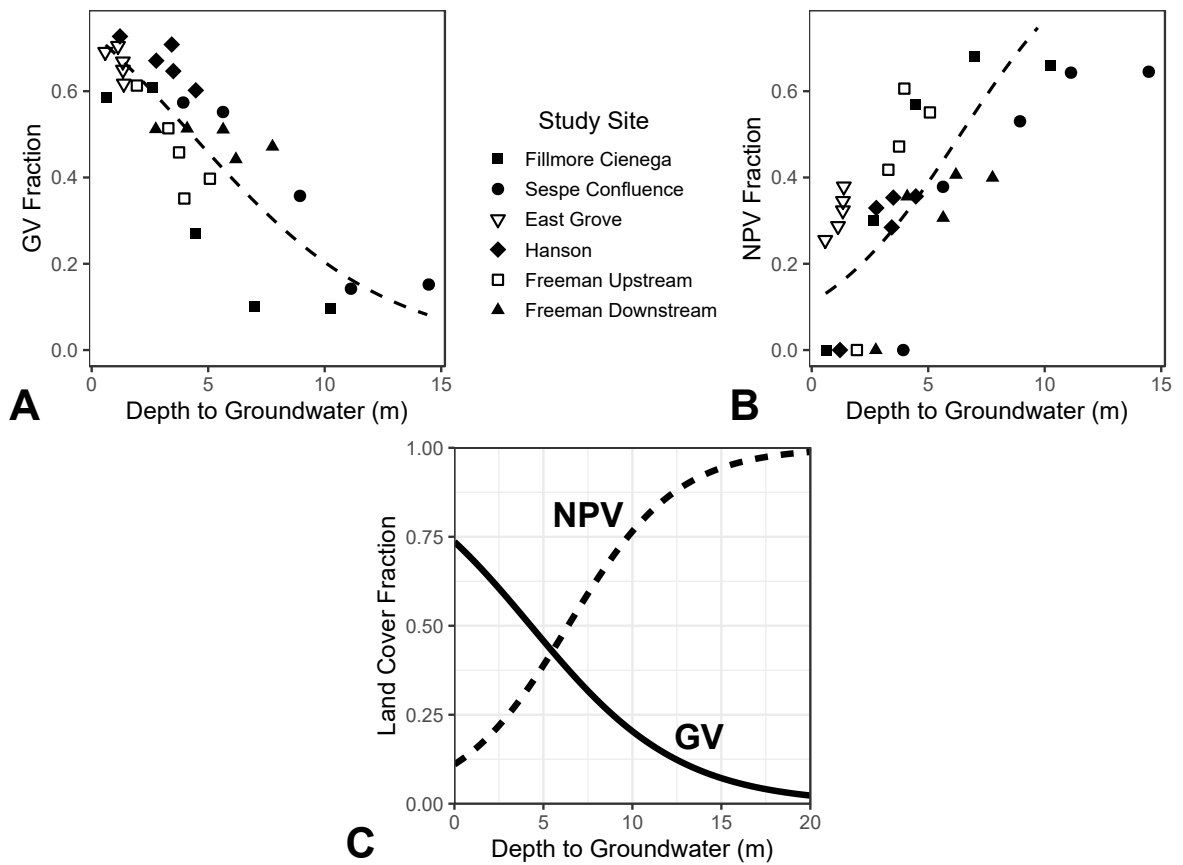
Figure 1.6: Scatterplots of mean DTG and median GV fractions (a) or median NPV fractions (b) from 2011 to 2016. The lines represent the modeled fixed effect of DTG on GV fractions (a,c) and NPV fractions (b,c).

GV fractions for Fillmore Ciénega deviated substantially from the values predicted by the model (decline MAE = 0.08; recovery MAE = 0.28). Fillmore Ciénega demonstrated a clear hysteresis signal, whereby groundwater rose by over 7 m (i.e., a reduced DTG), but there was only a modest increase in GV fractions (Figure 1.7). The lack of response to rising groundwater can be explained by dead vegetation covering the site. The DTG at Sespe Confluence remained relatively deep in 2017 and 2018, and the GV fractions did not deviate substantially from the values predicted by the model (decline MAE = 0.05; recovery MAE = 0.02). The modest increase in GV fractions is likely due to the invasion of *Arundo donax* after the widespread mortality of native phreatophytes, which is a common consequence of drought conditions affecting native plants (e.g., Merritt and Poff, 2010). Field observations indicate that A. donax now dominates the site (Figure S8). The other sites, where the native woodlands remained largely intact (e.g., Figure S9), exhibited consistent sensitivity to DTG during the decline (MAE = 0.02-0.07) and recovery (MAE = 0.03-0.09) phases.

1.4   Discussion

During the 2012-2019 California drought, riparian woodland mortality in the Santa Clara River floodplain followed a coherent spatial pattern and temporal trend that occurred across the river corridor and mirrored the apparent trend in DTG. Mortality first occurred at the upstream side of the Fillmore Ciénega site as flow between the Piru and Fillmore subbasins decreased around 2013. A distinct "brown wave" of mortality then traveled west (i.e., upstream to downstream) between 2013 and 2016 as groundwater in the Fillmore subbasin was progressively depleted. The brown wave stopped just upstream of the East Grove site, where groundwater elevations were relatively stable and surface flow was maintained throughout most of the drought (United Water Conservation Dis-
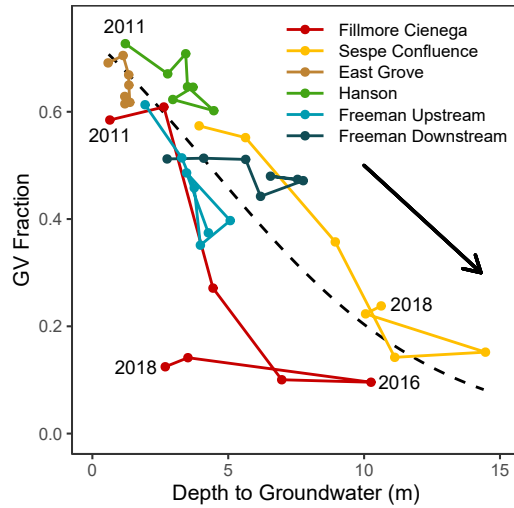
Figure 1.7: Scatterplot of DTG and median GV fractions from 2011 to 2018. The line segments connect observations from consecutive years. The observations from 2011 are generally in the upper left and the observations from 2018 are generally in the lower right. Observations from 2012 are omitted (see text). The dashed line represents the modeled fixed effect of DTG on GV fractions for data from 2011-2016.

trict, 2017). The brown wave reveals that riparian phreatophytes are extremely sensitive to DTG over both space and time, and that localized DTG trends play an important role in determining the fate of riparian woodlands during extreme drought conditions. Few studies have quantified the sensitivity of groundwater-dependent ecosystems to DTG (e.g., Lite and Stromberg, 2005), and only recently has it become possible to conduct spatially and temporally extensive analyses at a corridor scale (e.g., Huntington et al., 2016). Such analyses were historically limited by the available remote sensing data, which were too expensive (e.g., Zhu et al., 2019) or too coarse to resolve narrow stands of riparian woodlands (Dufour et al., 2012). Likewise, groundwater records have only recently been aggregated and made available in comprehensive data sets.

Groundwater serves as a crucial link in the chain of drought propagation from meteorological drying to plant responses by riparian phreatophytes. The 2012-2019 California drought was caused by record low precipitation and record high temperatures, which re-

duced water inputs to ecosystems and increased evaporative demand (Diffenbaugh et al., 2015; Warter et al., 2021). The drought generally reduced groundwater recharge (Harlow and Hagedorn, 2018) and caused groundwater elevations to decline, but subsurface water fluxes are spatially variable and are mediated by several factors including agricultural water use and runoff, river regulation, soil texture, and bedrock geology. During drought conditions, the hydrological drivers of groundwater elevation interact with meteorological trends to produce distinct spatial patterns and temporal trends of groundwater change (Jencso and McGlynn, 2011; Harlow and Hagedorn, 2018).

The spatiotemporal variability in groundwater elevation caused varying physiological responses in the riparian woodlands in the Santa Clara River floodplain. When water tables decline by several meters, the root systems of riparian trees can lose access to groundwater (Stromberg, 2013). Riparian tree species are poorly adapted to drought and can experience catastrophic xylem cavitation at relatively high (i.e., close to zero) vapor pressure deficits (Fichot et al., 2015). To mitigate and prevent this often-irreversible change, trees undergo a series of physiological changes to maintain a favorable water balance in the face of declining water supply (Rood et al., 2003). Within minutes, they can regulate stomatal conductance to limit transpirational water loss (Horton et al., 2001; Amlin and Rood, 2003; Pivovaroff et al., 2018). Leaf abscission and branch dieback, though detrimental to woody plants in the short term, can serve as long-term survival strategies that help trees reduce water demand and prevent the loss of xylem water conductance (Scott et al., 1999; Rood et al., 2000; Cooper et al., 2003). These physiological responses may not be adequate to mitigate water stress from large and sudden water table declines, which often cause hydraulic failure and whole-plant mortality (Scott et al., 1999; Lite and Stromberg, 2005; Tai et al., 2018).

The brown wave is likely an emergent property of individual plants responding to localized changes in DTG, as evidenced by the fine-scale changes in plant health and the

26

strong statistical relationships between the land cover fractions and DTG. Few studies have examined the spatial evolution of riparian woodland responses to water table declines (but see Stromberg et al., 1996; Scott et al., 1999, 2000; Tai et al., 2018). The current understanding of phreatophyte sensitivity to DTG is largely derived from field measurements (e.g., Horton et al., 2001; Rood et al., 2011), laboratory experiments (e.g., Leffler et al., 2000; Stella and Battles, 2010), and models based on phreatophyte physiology (e.g., Tai et al., 2018). These data have resulted in a conceptual model that suggests that there is a highly non-linear relationship between DTG and plant health, whereby plant health degrades rapidly when DTG increases beyond some critical threshold (e.g., Shafroth et al., 2000; Horton et al., 2001; Lite and Stromberg, 2005). In contrast with previous studies, our observations indicate that there is a mostly linear relationship between DTG and plant health at a stand scale when DTG is less than 10 m (i.e., Figure 1.6c). The difference in the shape of the observed relationships may indicate a scale dependence of the analysis. While many field and laboratory-based studies examine individual plants belonging to selected species, remote sensing data detects many plants belonging to many species within a pixel (Kibler et al., 2019). The observed plants that compose riparian woodlands likely have varying structures, life histories, and tolerances for groundwater decline (Stromberg et al., 1996; Stromberg and Merritt, 2016). Nonetheless, the observed sensitivity to absolute DTG and DTG change (Table S3) were generally consistent with previously reported values. At Fillmore Ciénega and Sespe Confluence, vegetation cover stopped changing as a function of DTG between 2015 and 2016, which may indicate a fundamental limit beyond which phreatophytes experience complete mortality and the health of the surviving non-phreatophytic vegetation becomes decoupled from DTG. The recovery of phreatophytes at these sites depends on the water table returning to shallow depths and seed sources for the germination of new seedlings (Stella et al., 2006).

1.5 Conclusion

The statistical analyses presented here provide some of the first robust estimates of the sensitivity of riparian woodlands to DTG. Our findings also reveal that DTG trends can be highly variable during extreme drought conditions, even within the same river corridor, which can result in distinct spatial patterns and temporal trends of plant mortality in riparian woodlands. Quantifying the sensitivity of riparian ecosystems to groundwater change will become increasingly important as anthropogenic climate change increases the frequency and severity of drought conditions across the western United States (Diffenbaugh et al., 2015; Rohde et al., 2017; Williams et al., 2020). The widespread mortality observed during the brown wave mirrors the dynamics of mass die-offs that have occurred in upland forest ecosystems (e.g., Allen et al., 2010; Goulden and Bales, 2019). Anthropogenic climate change, shifts in water availability, and other environmental forcings are overwhelming the resiliency of ecosystems that are typically buffered from climatic variability (Allen et al., 2015). Quantifying the sensitivity of both upland and lowland forests to hydroclimatic change will improve our ability to predict critical shifts in ecosystem structure and function in the coming decades.

Chapter 2

Evapotranspiration regulates leaf temperature and respiration in dryland vegetation

2.1 Introduction

Leaves serve as a critical nexus between water, energy, and carbon fluxes in terrestrial ecosystems, and leaf temperature (T_L) plays an important role in regulating the rates of mass and energy fluxes at the leaf surface (Still et al., 2021; Vinod et al., 2023). T_L directly influences several physical processes that drive mass and energy exchange, including leaf-to-air vapor pressure deficit (VPD; Grossiord et al., 2020), thermal conductance and emittance (Jones, 2014), net photosynthetic assimilation (Medlyn et al., 2002), and leaf respiration (R_L; Heskel et al., 2016). High values of T_L can also cause thermal stress and damage to leaf biochemical systems, which may permanently inhibit leaf physiologic function (O'Sullivan et al., 2017). T_L is thus a critical variable that regulates several aspects of terrestrial ecosystem function, and it is important to constrain the drivers of

T_L to better predict the sensitivity of terrestrial ecosystems to anthropogenic climate change.

Generally speaking, T_L is regulated by environmental conditions and energy fluxes at the leaf surface. Empirical observations have demonstrated that T_L is often close to air temperature (T_a), but the mechanistic relationship between T_L and T_a remains poorly constrained. Some studies have argued that leaves exhibit limited homeothermy, whereby the slope of the relationship between T_L and T_a is less than 1 (Michaletz et al., 2015, 2016; Blonder and Michaletz, 2018; Cook et al., 2021). Other studies have argued that leaves exhibit megathermy, whereby the slope of the relationship between T_L and T_a is greater than 1 (Salisbury and Spomer, 1964; Pau et al., 2018; Still et al., 2019b, 2022). Observations where $T_L \cong T_a$ (i.e., poikilothermy) have also been reported (Drake et al., 2020; Miller et al., 2021; Uni et al., 2022). The terminology for leaf thermal regimes follows the convention described by Cavaleri (2020). In practice, T_L observations are often normalized by T_a (i.e., $T_L - T_a$) to control for environmental variability and analyze other drivers of T_L.

Surface energy flux partitioning between latent (λE) and sensible (H) heat flux also plays an important role in regulating T_L. Surface energy balance must be preserved at the leaf scale, so leaf-level λE consumes energy that would otherwise increase T_L. Surface energy flux partitioning can be quantified using the evaporative fraction (f_E), which measures the proportion of available energy (Q_a) that is consumed by λE:

$$f_E = \frac{\lambda E}{Q_a} \tag{2.1}$$

Thus, there is a direct physical relationship between f_E and T_L, which results in evaporative cooling of the leaf surface.

Evaporative cooling has important functional implications for plant carbon cycling

and leaf physiologic function, particularly in hot and dry ecosystems (Hultine et al., 2020; Uni et al., 2022). Photosynthetic assimilation of carbon is highly dependent on T_L at the leaf scale (Medlyn et al., 2002). Maintaining lower T_L also reduces R_L (Heskel et al., 2016; Mathias and Trugman, 2022) and can prevent thermal damage to leaves (O'Sullivan et al., 2017). Indeed, several recent studies have speculated that plants may decouple photosynthesis and transpiration during extreme heat waves to maintain high levels of λE, which keeps T_L below critical thresholds that would result in damage to the leaf tissue (Drake et al., 2018; Krich et al., 2022; *cf.* De Kauwe et al., 2019). Likewise, water availability for evaporative cooling may limit the distributions of some plant species in dryland ecosystems when they cannot maintain physiologic function at ambient temperatures (Hultine et al., 2020). Improving mechanistic models of T_L will enhance our understanding of the feedbacks between water, energy, and carbon fluxes at the leaf surface and improve our ability to predict shifts in ecosystem function under anthropogenic climate change. It will also improve our ability to map ecosystem water fluxes at broad spatial scales using thermal remote sensing data (Mallick et al., 2022).

Many models predict T_L or $T_L - T_a$ by combining energy balance theory with the Penman-Monteith equation (e.g., Monteith and Unsworth, 2013). However, implementing these models requires empirical assumptions about stomatal conductance, which is difficult to constrain. Here, we present an alternate modeling framework that predicts T_L as a linearized function of f_E. Our mechanistic model requires fewer surface parameters than previous formulations, which improves our ability to isolate and examine the environmental variables that drive T_L. The simplified model also yields fundamental insights into the relationship between T_L and T_a under varying environmental conditions, and the resulting impacts on plant physiologic function.

The paper is organized as follows. First, we present the new model. Then, we validate the model predictions using T_L measurements from infrared radiometers mounted on two

flux towers in Arizona, USA, which measure stands of *Prosopis velutina* with contrasting water availability. We also examine the environmental variables that are most important for predicting T_L in the observational data set. Finally, we force the model with flux tower measurements to estimate the change in R_L that is attributable to evaporative cooling of the leaf surface, which may reveal an important link between evaporative cooling and net carbon uptake. In doing so, we address the following research questions:

1. How sensitive is T_L to changes in surface energy flux partitioning between λE and H?

2. Which environmental variables directly regulate T_L? Which of those variables is most important for regulating T_L in dryland ecosystems?

3. How much is R_L reduced by evaporative cooling of the leaf surface?

2.2 Methods

2.2.1 Leaf temperature model

Steady-state surface energy balance can be modeled as the difference between Q_a, H, and λE:

$$Q_a - H - \lambda E = 0 \qquad (2.2)$$

When modeling the energy balance of individual leaves, the Q_a term is equivalent to leaf-level net radiation (R_n), which is the sum of downwelling ($\downarrow$) and upwelling ($\uparrow$) shortwave (SW) and longwave (LW) radiation fluxes:

$$R_n = SW\!\downarrow - SW\!\uparrow + LW\!\downarrow - LW\!\uparrow \qquad (2.3)$$

32

The $LW\uparrow$ term can be calculated as a function of T_L measured in K:

$$LW\uparrow = k\varepsilon_L \sigma T_L^4 \tag{2.4}$$

where ε_L is leaf emissivity ($\varepsilon_L = 0.98$), σ is the Stefan-Boltzmann constant (5.67×10^{-8} W m^{-2} K^{-4}), and k is a coefficient that indicates whether it is a one-sided ($k = 1$) or two-sided ($k = 2$) leaf model. The H term in Equation 2.2 can be calculated as:

$$H = k\frac{\rho c_p (T_L - T_a)}{r_H} \tag{2.5}$$

where ρ is air density, c_p is the specific heat of air, and r_H is the aerodynamic resistance to H. We combined Equations 2.1, 2.2, and B.6 and rearranged to produce a novel linearized equation for $T_L - T_a$:

$$
\begin{aligned}
T_L - T_a &= \frac{Q_a r_H}{k\rho c_p}(1 - f_E) \\
&= \frac{Q_a r_H}{k\rho c_p} - \frac{Q_a r_H}{k\rho c_p}f_E
\end{aligned}
\tag{2.6}
$$

The expanded version of Equation 2.6 contains two additive terms: a radiative heating term that is proportional to Q_a and an evaporative cooling term that is proportional to f_E. Importantly, Equation 2.6 reveals that $T_L - T_a$ is a linear function of f_E and that the slope and intercept are functions of Q_a and r_H. Because the slope and intercept negate each other (i.e., slope = intercept $\times$ -1), $T_L - T_a = 0$ °C when $f_E = 1$, which reveals that T_L converges at T_a when λE consumes all of the energy incident on the leaf surface. It follows that:

$$T_L = T_a + \frac{Q_a r_H}{k\rho c_p} - \frac{Q_a r_H}{k\rho c_p} f_E \tag{2.7}$$

Equation 2.7 provides a framework to examine the competing roles of T_a, radiative heating, and evaporative cooling in regulating T_L. It also provides a framework to examine the resulting impacts on plant physiologic function.

It is worth noting that T_L appears on both sides of Equation 2.7 because T_L regulates R_n and thus Q_a (i.e., Equation 2.4). If R_n is not measured directly, Equation 2.7 can be solved numerically, as is discussed below in Section 2.2.3. Alternatively, the R_n term can be approximated using isothermal net radiation ($R_{n,i}$) following Jones (2014):

$$R_{n,i} = SW\!\downarrow - SW\!\uparrow + \varepsilon_L LW\!\downarrow - k\varepsilon_L \sigma T_a^4 \tag{2.8}$$

We used direct measurements of R_n throughout our analysis, except as noted in Section 2.2.3.

2.2.2 Leaf temperature sensitivity analysis

We modeled the sensitivity of $T_L - T_a$ to environmental drivers by forcing Equation 2.6 with simulated values of Q_a (250, 500, and 750 Wm^{-2}), r_H (1, 10, 20, 30, and 40 sm^{-1}), and f_E (0-1). The ρ term was held constant at 1.006 kg m^{-3}, and the c_p term was held constant at 1010 J K^{-1} kg^{-1}, which are representative values for the study area. A one-sided model ($k = 1$) was used to facilitate intercomparison with subsequent analyses.

2.2.3 Flux tower observations

We compared the modeled sensitivities from Equation 2.6 to measurements from two eddy covariance flux towers in Arizona, USA, where T_L was measured by infrared

radiometers mounted on the towers. The infrared radiometers measured the average temperature of many leaves on the outside of the *P. velutina* canopies, so we use the term T_c to describe the radiometer measurements of "canopy-scale leaf temperature" following Still et al. (2021). However, we generally assume that $T_c \cong T_L$, and we use T_c and T_L interchangeably. The flux tower data set contains 17 site-years of growing season measurements under varying environmental conditions. We also used the flux tower data to analyze the environmental drivers of T_c and to quantify the impact of T_c on R_L.

The T_c measurements by the infrared radiometers represent leaves on the outside of a single *P. velutina* canopy, while the eddy covariance measurements represent the average fluxes within the fetch of the sensors (*ca.* 50-200 m). We acknowledge the scale mismatch between the canopy-scale T_c measurements and the fetch-scale flux measurements, but we contend that novel insights can still be gleaned from the measurements using a "big leaf" assumption, whereby the entire fetch is assumed to behave like a single leaf in order to link leaf-scale theoretical models with canopy-scale measurements (e.g., Sellers et al., 1992; Amthor, 1994). In this context, Equation 2.7 can be used to predict the average surface temperature of an entire canopy or stand. Canopy-scale processes are arguably more important than leaf-scale processes for understanding terrestrial ecosystem function, but they are also more difficult to constrain (Bonan, 2016). The temperature and fluxes of individual leaves can be measured using *in situ* sensors, but they may not be representative of the canopy as a whole (Miller et al., 2021; Vinod et al., 2023). We believe that the big leaf assumption is a reasonable approach to glean insights into the theoretical drivers of canopy-scale processes. To connect the leaf-scale theoretical model with the canopy-scale measurements, we included a ground heat flux (G) term when calculating Q_a, such that:

$$Q_a = R_n - G \tag{2.9}$$

35

Equation 2.9 helps control for the loss of available energy through the bottom of the canopy. We also used a one-sided model ($k = 1$) for all analyses.

Study sites

We analyzed data from two flux towers located in stands of *P. velutina* in southeastern Arizona, USA. Southeastern Arizona has a semi-arid climate with monsoonal precipitation that is delivered in brief, spatially restricted storms that dominate total annual rainfall and runoff (Thomas and Pool, 2006; Singer and Michaelides, 2017). The summer growing season encompasses both the driest and wettest parts of the year. The first part of the growing season is very dry, but ecosystems receive intense precipitation after the onset of the monsoon around early July. The monsoonal precipitation and accompanying humidity typically decrease after August, but generally remain above pre-monsoon levels through the end of the growing season (Higgins et al., 1997). The two stands that we analyzed have contrasting physiographic positions resulting in differences in plant water availability, particularly during the dry months before the onset of the monsoon. The differences in water availability create ideal conditions for a natural experiment to quantify the sensitivity of T_c to λE and environmental conditions, while holding regional climatic variables relatively constant.

The first flux tower is in a riparian woodland approximately 16 km northeast of Sierra Vista, Arizona (31.6637°N, 110.1777°W). The riparian woodland is located on an old alluvial terrace above the San Pedro River, where the depth to groundwater is approximately 10 m (Sabathier et al., 2021). The flux tower is located *ca.* 225 m from the river channel, and the alluvial terrace is *ca.* 10 m above the river channel, so we assume that evaporation from the river channel does not affect the λE measurements. The mean summer air temperature is 25 °C and the mean annual precipitation is 319 mm (PRISM Climate Group, 2021; Huntington et al., 2017). The woodland is dominated by

a canopy of *P. velutina* (canopy cover ∼70%) with a mean height of 7 m and a maximum height of 10 m. Leaf emergence for the deciduous *P. velutina* trees typically occurs in April, and plant hydraulic function increases in late May. The understory is dominated by the perennial grass *Sporobolus wrightii* but annual forbs and herbs are common during the summer monsoon season (Scott et al., 2004). Rooting depths of *P. velutina* can exceed 10 m (Stromberg, 2013), and the pre-monsoon fluxes reveal that overstory vegetation accesses groundwater. Because groundwater provides a stable source of water that is somewhat decoupled from the local precipitation regime, evapotranspiration (ET) consistently exceeds precipitation on an annual basis (Missik et al., 2021; Scott et al., 2021). Groundwater is an important water source for maintaining vegetation structure and function in many dryland riparian plant communities (Kibler et al., 2021). The understory vegetation has a maximum rooting depth of 2-3 m, so it does not have access to groundwater and is dependent on water inputs from local precipitation (Scott et al., 2004).

The second flux tower is in an upland savanna at the Santa Rita Experimental Range, approximately 45 km south of Tucson, Arizona (31.8214°N, 110.8661°W). The site is a semi-desert grassland that has been encroached by *P. velutina*. The mean summer air temperature is 26 °C and the mean annual precipitation is 368 mm (PRISM Climate Group, 2021; Huntington et al., 2017). Scott et al. (2009) reported that the *P. velutina* canopy ranges in height from 0.25 to 6 m (mean height 2.5 m) and covers ∼35% of the ground area. Leaf emergence for *P. velutina* typically occurs in April (Seyednasrollah et al., 2019). The *P. velutina* plants at the upland savanna likely had lower leaf area index and smaller average leaf size than those at the riparian woodland (Stromberg et al., 1993). Perennial grasses, forbs, and subshrubs cover ∼22% of the ground area (Scott et al., 2009). Depth to groundwater exceeds 100 m, so the overstory and understory vegetation do not have access to groundwater and are dependent on water inputs from

local precipitation.

Both flux towers contain an array of eddy covariance, meteorological, and soil sensors, along with infrared radiometers (IRT-P, Apogee Instruments, Logan, UT) pointed 45° off-nadir at the *P. velutina* canopies. This study primarily relied on flux measurements of λE, H, R_n, G, SW$\downarrow$, SW$\uparrow$, and LW$\downarrow$; meteorological measurements of T_a, wind speed (u), and relative humidity (RH); measurements of soil temperature (T_s) and soil water content (SWC); and T_c measurements from the infrared radiometers. In the riparian woodland, λE and H were measured at 14 m. G was quantified for the surface using soil heat flux plate measurements at 5 cm depth along with the change in heat storage from 0-5 cm depth. Canopy-level T_a, u, and RH were measured at 8 m. T_s was measured at 5 cm depth and SWC was measured at 22.5 cm depth. The infrared radiometer was mounted at 10 m. A four-component net radiometer measured individual SW$\downarrow$, SW$\uparrow$, LW$\uparrow$, and LW$\downarrow$ fluxes from 2001-2003, but it was replaced by a two-channel SW and LW net radiometer from 2004-2006. The four-channel radiometer was mounted at 14 m, and the sensors for the two-channel radiometer were mounted at 10 m and 14 m. In the upland savanna, λE and H were measured at 7.8 m; SW$\downarrow$, SW$\uparrow$, LW$\uparrow$, and LW$\downarrow$ were measured at 7.1 m; and G was quantified for the surface. Canopy-level T_a and RH were measured at 2 m. Canopy-level u was measured at 3.5 m. T_s was measured at 5 cm depth and SWC was measured at 20 cm depth. The infrared radiometer was mounted at 7 m. Atmospheric transmittance and emittance were assumed to have a negligible impact on the radiometer measurements over the short distances (*ca.* 5 m) between the radiometers and the canopies (Aubrecht et al., 2016). We also assumed that the differences in T_a between the meteorological sensors and the canopies were negligible, given that the T_a sensors were at approximately the same heights as the measured leaves. All flux tower data were acquired from Ameriflux (sites US-CMW and US-SRM, respectively). See Scott (2021a,b) and Scott et al. (2004, 2009) for additional details about the collection

and processing of the flux tower data.

Several criteria were used to filter the half-hourly flux tower measurements:

- growing season observations between May and September

- daytime observations between 8:00 and 16:00 local time

- removed days with any measured precipitation and the day after any measured precipitation

- observations with friction velocity $(u_*) > 0.2$

We also removed years that did not have complete records of growing season measurements and years where there were apparent shifts in the infrared radiometer view angle due to a loose mounting bracket, as evidenced by sudden changes in the relationship between T_c and T_s at 5 cm depth. Based on these criteria, two site-years of data were removed for the riparian woodland (2007 and 2008), and four site-years of data were removed for the upland savanna (2014, 2015, 2020, and 2021). The resulting data set contained six site-years of data for the riparian woodland (2001-2006) and eleven site-years of data for the upland savanna (2007-2019, excluding 2014 and 2015). The R_L analysis relied on individual measurements of SW↓, SW↑, and LW↓ fluxes, which were only available from 2001-2003 at the riparian woodland. They were available for all years at the upland savanna. The flux tower measurements were used to force Equation 2.7 and analyze the sensitivity of T_c to λE and environmental conditions. All of the other terms in Equation 2.7 can be directly derived from the flux tower measurements, except for r_H.

Resistance to sensible heat flux

Following Young et al. (2021), the canopy-scale r_H is the sum of the resistance to momentum transfer (r_{am}) and the excess resistance (r_{bh}):

$$r_H = r_{am} + r_{bh} \tag{2.10}$$

The r_{am} term can be estimated as a function of u and the friction velocity (u_*):

$$r_{am} = \frac{u}{u_*^2} \tag{2.11}$$

The r_{bh} term is a function of the roughness lengths for momentum (z_{0m}) and heat (z_{0h}) as well as stability functions for momentum (ψ_m) and heat (ψ_h) exchange:

$$r_{bh} = \frac{1}{\kappa u_*} \left[ln \left(\frac{z_{0m}}{z_{0h}} \right) - \psi_h + \psi_m \right] \tag{2.12}$$

where κ is the Von Kármán constant ($\kappa = 0.41$). Equation 8 can be simplified to ignore the stability functions, which have a negligible impact on the predicted values of r_{bh} at a canopy scale (Young et al., 2021):

$$r_{bh} = \frac{1}{\kappa u_*} ln \left(\frac{z_{0m}}{z_{0h}} \right) \tag{2.13}$$

The z_{0m} and z_{0h} terms are often represented by the parameter kB^{-1} such that:

$$kB^{-1} = ln \left(\frac{z_{0m}}{z_{0h}} \right) \tag{2.14}$$

$$r_{bh} = \frac{1}{\kappa u_*} kB^{-1} \tag{2.15}$$

At an ecosystem scale, the parameter kB^{-1} varies as a function of land cover, leaf area, vegetation structure, and environmental conditions (Yang and Friedl, 2003). Various empirical formulations for kB^{-1} have been developed. We estimated kB^{-1} as an empirical function of u_* following Thom (1972), which yielded the most parsimonious predictions of r_H out of 12 formulas described by Verhoef et al. (1997) and Hong et al. (2012). The comparison of the formulas is described in Appendix B.

$$kB^{-1} = 1.35\kappa(100u_*)^{1/3} \tag{2.16}$$

Model validation

The flux tower measurements were used to validate the model described in Equation 2.7. We compared the T_c measurements from the infrared radiometers to T_c predictions that were generated by forcing Equation 2.7 with concurrent flux tower measurements. The MAE, R^2, slope, and bias were used to quantify the model performance at each site.

Energy balance closure

The model presented in Equation 2.7 assumes energy balance closure. However, energy balance closure is rarely achieved in eddy covariance measurements due to systematic sensor errors, differences in the spatial footprints of individual sensors, advective fluxes, and a variety of other factors (Stoy et al., 2013; Mauder et al., 2020). The energy balance closure ratio (C) can be calculated as:

$$C = \frac{\lambda E + H}{Q_a} \tag{2.17}$$

We calculated C for the half-hourly flux measurements using Equation 2.17.

We quantified the sensitivity of the T_c predictions to C by forcing closure in the flux

measurements and then comparing the T_c predictions from the forced and unforced values. While forcing energy balance closure is often not recommended for eddy covariance analyses (e.g., Scott, 2010), comparing the different T_c predictions enabled us to quantify the model error that might be attributable to the lack of energy balance closure. Energy balance closure was forced by assuming that the λE and H were measured correctly and adjusting the value of Q_a. Energy balance closure can also be forced by assuming that Q_a was measured correctly and adjusting the values of λE and H (Twine et al., 2000; Knauer et al., 2018). However, the H term is not explicitly represented in Equation 2.7. Energy balance closure was forced by setting Q_a equal to the sum of the turbulent fluxes:

$$Q_{a,f} = \lambda E + H \tag{2.18}$$

where the subscript f denotes that the value was adjusted to force energy balance closure. Equation 2.7 was forced with $Q_{a,f}$ to generate a new set of T_c predictions. All other model forcings remained unchanged. We compared the two sets of T_c predictions to estimate the model error that might be attributable to the lack of energy balance closure.

T/ET partitioning

The model presented in Equation 2.7 also assumes that all λE is attributable to leaf transpiration (T). However, eddy covariance measurements are collected at a stand scale, and soil evaporation (E) may also contribute to the λE signal. The ratio of T/ET can be used to quantify the extent to which the λE signal is attributable to T. Several methods have been proposed to partition T and E in eddy covariance measurements (Stoy et al., 2019). We reanalyzed data from Scott et al. (2021) and Nelson et al. (2020a,b), who partitioned data for the riparian woodland and upland savanna, respectively, using the method proposed by Nelson et al. (2018). We used their daily estimates of T and ET

to calculate T/ET for the two sites. The T/ET analysis included all days where there was at least one half-hourly measurement in the filtered eddy covariance data set and an estimate of T/ET from the published data sets. The resulting data set covered years 2005-2006 for the riparian woodland and 2007-2013 for the upland savanna.

Analysis of flux tower measurements

We conducted several analyses to identify the mechanistic basis for the model behavior using the flux tower measurements. We compared the distributions of the $T_c - T_a$ and f_E measurements and calculated the seasonal and diurnal climatology of $T_c - T_a$ at each site. We also produced seasonal and diurnal climatologies for the individual drivers of T_c, including T_a, f_E, r_H, and Q_a. Spearman rank correlation was used to quantify the sensitivity of T_c and $T_c - T_a$ to the individual drivers. The data were grouped by month to assess seasonal changes in the variables that drive T_c and $T_c - T_a$. Spearman rank correlation was also used to quantify the sensitivity of f_E, r_H, and Q_a to environmental variables measured by the flux towers, which may have an indirect effect on T_c and $T_c - T_a$. The environmental variables include SW↓, VPD, u, and soil water content (SWC). VPD was calculated using the flux tower measurements of T_a and RH following Allen et al. (1998).

Leaf respiration model

We also analyzed the sensitivity of daytime leaf respiration (R_L) to changes in T_c caused by λE variability. Leaf respiration is a complex biochemical process that varies as a function of leaf mass per area, leaf nitrogen and phosphorus concentrations, photosynthetic carboxylation capacity, T_L, and other variables (Atkin et al., 2015). Leaf respiration is also inhibited by sunlight during the daytime (Kok, 1948; Heskel et al., 2013). In practice, R_L is often estimated as an empirical function of T_L (Mathias and

Trugman, 2022). We estimated leaf dark respiration ($R_{L,dark}$) following Heskel et al. (2016):

$$R_{L,dark}(T_L) = R_{L,dark}(T_{ref}) * e^{0.1012(T_L - T_{ref}) - 0.0005(T_L^2 - T_{ref}^2)} \tag{2.19}$$

where T_{ref} is the reference temperature and $R_{L,dark}$ is measured in units of CO_2 m^{-2}s^{-1}. The $R_{L,dark}(T_{ref})$ parameter was set to 1.7 µmol CO_2 m^{-2}s^{-1} based on a measurement of *Prosopis glandulosa* by Reich et al. (1998) at a T_{ref} of 25 °C. Leaf light respiration ($R_{L,light}$) was modeled as a function of $R_{L,dark}$ following Way et al. (2015) and Mathias and Trugman (2022):

$$R_{L,light}(T_L) = R_{L,dark}(T_L) * (0.0039 * T_L + 0.6219) \tag{2.20}$$

Equation 2.20 helps control for the light inhibition of R_L, which is not represented in the $R_{L,dark}$ estimates (Way et al., 2015).

We estimated $R_{L,light}$ using two temperature forcings: T_c and modeled canopy temperature with no evaporative cooling ($T_{c,ne}$). We modeled T_c by forcing Equation 2.7 with flux tower measurements. The r_H term was calculated using Equations 2.10-2.16. We used modeled rather than measured T_c values to control for any effect of changing sensor calibrations over the multi-annual time series. We modeled $T_{c,ne}$ by setting λE to 0 in Equation 2.7. We also calculated Q_a as a function of its component fluxes (Equations 2.3-2.4) to account for the effect of T_c on $LW\uparrow$. When all terms in Equation 2.7 are directly measured, the feedback between T_c and $LW\uparrow$ is implicitly encoded in the flux measurements. However, when combining measured and forced flux values (i.e., by setting λE to 0), the feedback must be explicitly specified in the analytical formulation. The $LW\downarrow$ term must also be multiplied by ε_L. The equation for $T_{c,ne}$ can be written as:

$$T_{c,ne} = T_a + \frac{(SW\downarrow - SW\uparrow + \varepsilon_L LW\downarrow - \varepsilon_L \sigma T_{c,ne}^4 - G)r_H}{\rho c_p} \tag{2.21}$$

Equation 2.21 estimates the temperature of a non-transpiring canopy. The terms of the equation were forced with flux tower measurements. To make Equation 2.21 analytically tractable, we rewrote the equation in the form of a quartic function and solved for $T_{c,ne}$ using a numerical solver (NumPy v1.23.3; Harris et al., 2020). Physically unreasonable values where modeled $T_{c,ne}$ was less than modeled T_c were likely due to the lack of energy balance closure and were removed from the analysis.

The difference between the estimates of $R_{L,light}$ using T_c and $T_{c,ne}$ revealed the marginal change in $R_{L,light}$ that is attributable to T_c variability caused by λE (i.e., $\partial R_{L,light}/\partial T_c(\lambda E)$). This framework enabled us to estimate the decrease in daytime R_L caused by evaporative cooling of the leaf surface (ΔR_L).

2.3 Results

2.3.1 Leaf temperature model

The mechanistic model of T_L presented in Equation 2.7 reveals that there are three drivers of T_L: (1) T_a, (2) a radiative heating term that is proportional to Q_a, and (3) an evaporative cooling term that is proportional to f_E. The model predicts that T_L converges to T_a when λE consumes all of the energy incident on the leaf surface, regardless of environmental conditions (Figure 2.1). When $f_E < 1$, $T_L - T_a$ also varies as a function of Q_a and r_H. Importantly, the model predicts that $T_L - T_a \geq 0$ °C under all conditions, although there are environmental conditions when $T_L - T_a$ approaches 0 °C even though $f_E < 1$. Specifically, the model predicts that $T_L - T_a = 0$ °C when $Q_a = 0$ Wm^{-2} or when $r_H = 0$ sm^{-1}, regardless of the value of f_E. The first condition often happens around
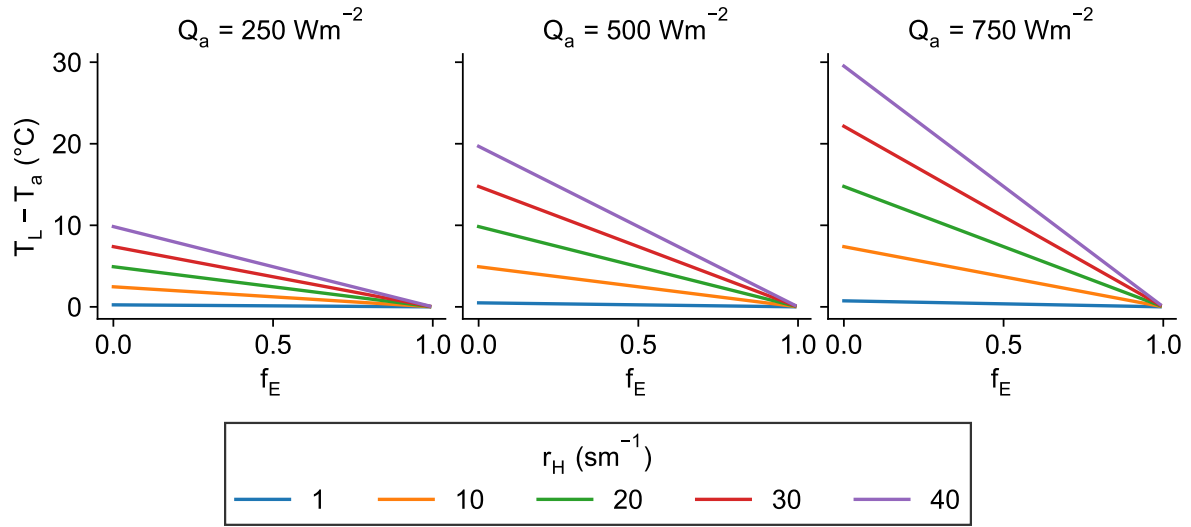
Figure 2.1: Predicted values of $T_L - T_a$ from Equation 2.6 calculated using different values of available energy (Q_a), evaporative fraction (f_E), and resistance to sensible heat flux (r_H). Air density (ρ) was held constant at 1.006 kg m^{-3}. The specific heat of air (c_p) was held constant at 1010 J K^{-1} kg^{-1}.

dawn and dusk, while the second condition is unrealistic in real-world settings (Young et al., 2021).

2.3.2 Model validation

The model of T_L presented in Equation 2.7 was validated by forcing Equation 2.7 with flux tower measurements and comparing the T_L predictions to concurrent T_c measurements from infrared radiometers mounted on the flux towers. The T_c measurements represented the average temperature of many leaves on the outside of a *P. velutina* canopy, and we generally assumed that $T_c \cong T_L$. The model yielded strong fits at both study sites (Figure 2.2). The predictions for the riparian woodland exhibited a stronger fit (MAE = 2.67 °C). The predictions for the upland savanna exhibited a slightly weaker fit (MAE = 3.42 °C), but the range of observed T_c values was also larger. The model tended to slightly overestimate T_c at both sites (mean bias = 2.53 °C and 1.55 °C, respectively).
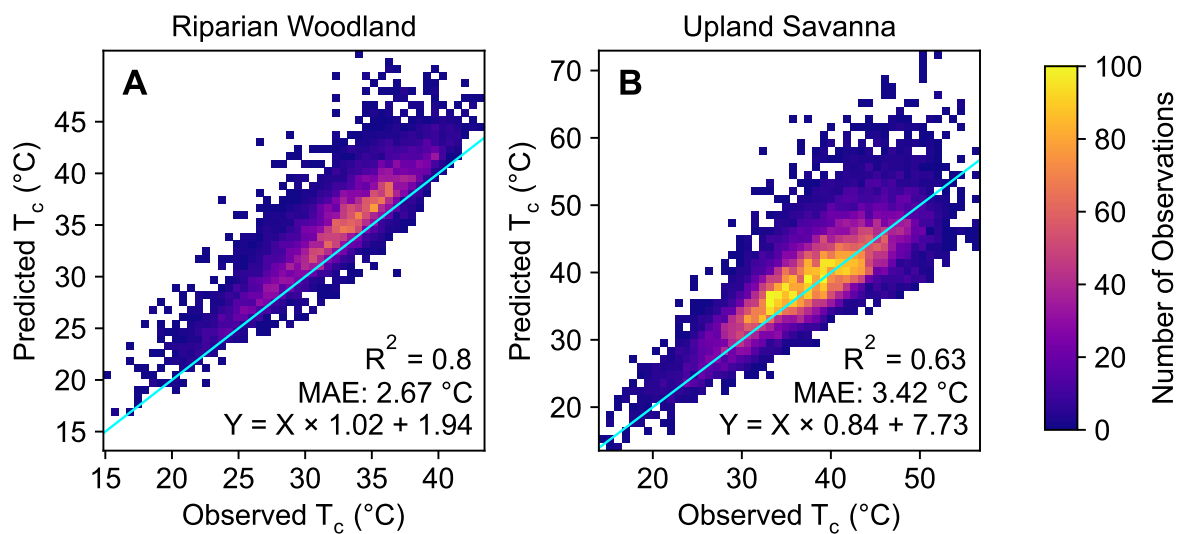
Figure 2.2: Model predicted T_c compared to T_c measurements from the infrared radiometers for the riparian woodland (a) and upland savanna (b). The predicted T_c values were calculated by forcing Equation 2.7 with flux tower measurements. The blue lines are the 1:1 line. The mean absolute error (MAE) is also indicated. White areas in the plots indicate that there were 0 observations in that portion of the feature space. The color scale saturates when there are more than 100 half-hourly observations in a given portion of the feature space.

2.3.3   Energy balance closure

We also assessed the impact of energy balance closure on the T_c predictions. The median energy balance closure ratio (C) in the riparian woodland was 0.86 with an interquartile range of [0.75, 0.98]. The median C in the upland savanna was 0.83 with an interquartile range of [0.75, 0.92] (Figure B.5). Forcing energy balance closure by adjusting the Q_a value reduced the T_c predictions by 1.06 °C in the riparian woodland and 1.64 °C in the upland savanna. The MAE between the two sets of T_c predictions was 1.38 °C in the riparian woodland and 1.8 °C in the upland savanna. The T_c predictions based on $Q_{a,f}$ were more parsimonious than the predictions based on the unforced values when compared to the infrared radiometer measurements at both sites. The R^2 values were 0.89 and 0.7 for the riparian woodland and upland savanna, respectively. The analysis suggests that the overestimation of T_c seen in Figure 2.2 is due, in part, to the lack of energy balance closure in the flux data. This is supported by comparing the model prediction error to the C values. In the riparian woodland, the average model prediction error was near 0 °C when $C \approx 1$. When C decreased below 1, the model prediction error increased monotonically. In the upland savanna, the model prediction error also increased as C decreased below 1, although the upland savanna exhibited a less clear trend (Figure B.5).

2.3.4   T/ET partitioning

The analysis of T/ET values indicated that the λE signal was dominated by T and not E at both sites (Figure 2.3). In the riparian woodland, the median daily T/ET value ranged from 0.87 to 0.92 for each month. In the upland savanna, the median daily T/ET value ranged from 0.72 to 0.8 for each month. The upland savanna exhibited more variability in T/ET values, suggesting that E may have contributed more error to the
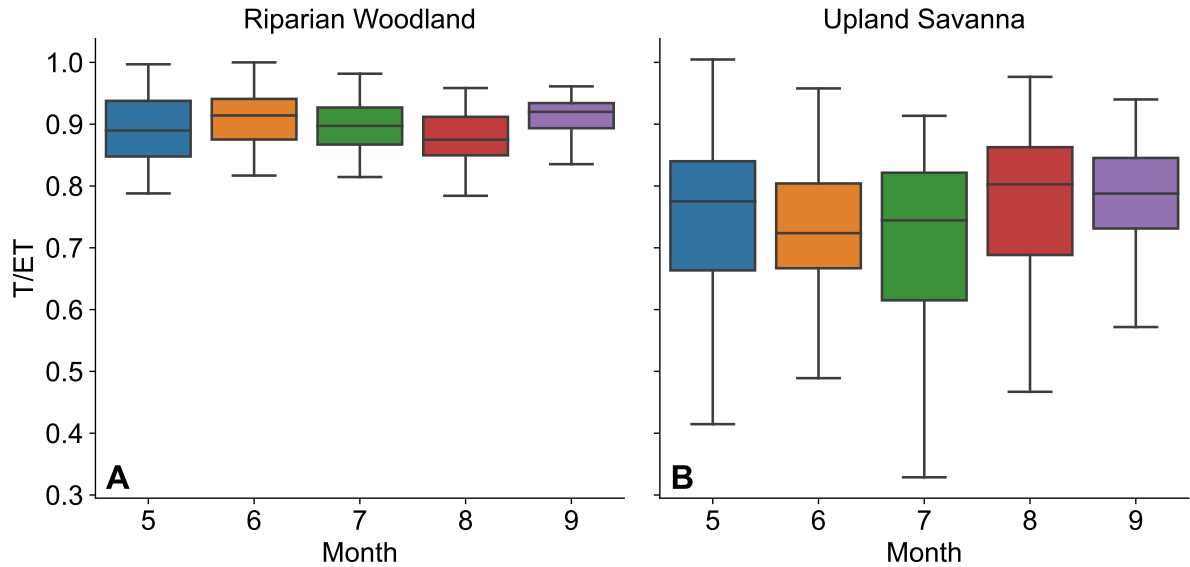
Figure 2.3: Boxplots of daily T/ET values in the riparian woodland (a) and upland savanna (b) for each month of the growing season. Data are reanalyzed from Scott et al. (2021) and Nelson et al. (2020a,b). Outliers are not shown.

model predictions at that site. The T/ET values were relatively consistent throughout the growing season and did not exhibit any apparent seasonal trend at either site.

2.3.5 Flux tower observations

We also analyzed the flux tower observations to characterize the mechanistic basis for the model behavior. In the riparian woodland, $T_c - T_a$ remained close to 0 °C for the entire time series, although $T_c - T_a$ varied both seasonally and diurnally. The mean $T_c - T_a$ value across the entire data set was 1.57 °C (Figure 2.4). $T_c - T_a$ values near 0 °C indicate that there was a substantial degree of evaporative cooling in the riparian woodland. Otherwise, T_c would substantially exceed T_a because of energy inputs from solar radiation. The largest $T_c - T_a$ values tended to occur in May when the trees were leafing out and plant hydraulic function was still increasing. The values decreased substantially starting in June (Figure 2.5). In May, the average peak value was 4.27 °C,

and by June the average peak value decreased to 2.44 °C, with lower peaks occurring in subsequent months. The daily maximum values tended to occur around 11:30 local time.

The upland savanna exhibited similar trends. The mean $T_c - T_a$ value across the entire data set was 6.46 °C (Figure 2.4). The largest values tended to occur in the dry months of May and June and decreased substantially starting in July when the summer rainy season began (Figure 2.5). In June, the average peak value was 10.59 °C. By August, the average peak value decreased to 5.72 °C. Unlike the riparian woodland, the daily maximum values tended to occur around 13:00 local time.

The sensitivity of $T_c - T_a$ to f_E from the flux tower measurements was consistent with the sensitivity predicted by Equation 2.6. At both sites, $T_c - T_a$ converged to 0 °C as f_E approached 1 (Figure 2.4), which is consistent with the model predictions shown in Figure 2.1. When $f_E < 1$, the range and distribution of measured $T_c - T_a$ values was also similar to the modeled values. The $T_c - T_a$ values ranged from -1.24 °C (1st percentile) to 7.61 °C (99th percentile) in the riparian woodland and -0.25 °C (1st percentile) to 16.44 °C (99th percentile) in the upland savanna. The maximum values at both sites occurred when f_E approached 0, consistent with the model predictions. The f_E values for the upland savanna (mean $f_E = 0.15$) were on average lower than the f_E values for the riparian woodland (mean $f_E = 0.46$), which provides a mechanistic explanation for why $T_c - T_a$ was generally greater at the upland savanna than the riparian woodland.

The flux tower measurements exhibited a non-linear relationship between f_E and $T_c - T_a$, especially at the riparian woodland. The model in Equation 2.6 predicts a linear relationship between f_E and $T_c - T_a$ when all other variables are held constant. The apparent non-linear relationship between f_E and $T_c - T_a$ is likely due to covariance between f_E, r_H, and Q_a on seasonal and diurnal time scales. The model validation accounted for the changing values of f_E, r_H, and Q_a, and it demonstrated strong model performance at both sites (Figure 2.2).
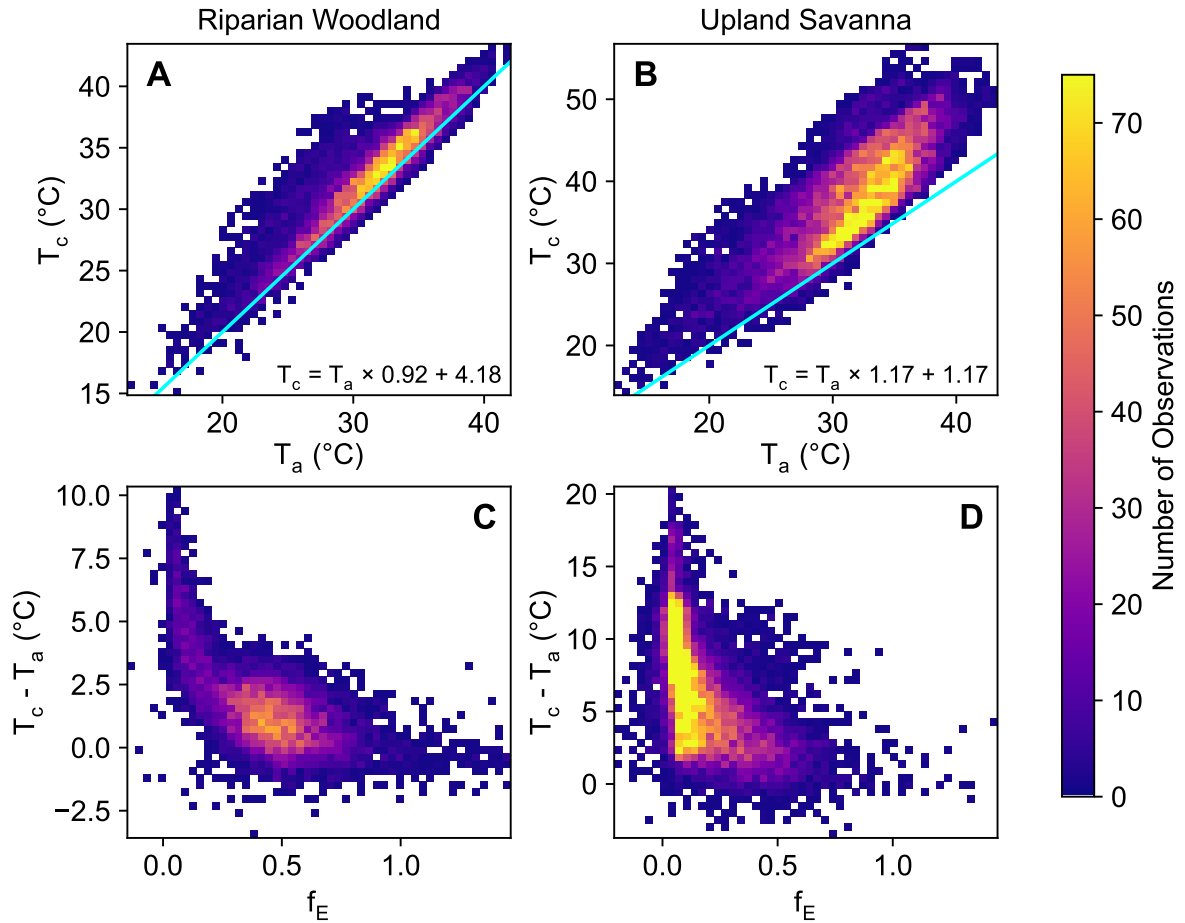
Figure 2.4: Energy flux measurements from the riparian woodland (a,c) and upland savanna (b,d) differ in that the riparian woodland has a higher evaporative fraction (f_E) compared to the upland savanna. However, in both systems leaf temperature (T_c) converges to air temperature (T_a) when f_E approaches 1. The plots in the top row (a,b) compare T_a and T_c measurements. The blue lines are the 1:1 line. The plots in the bottom row (b,d) show the relationship between $T_c - T_a$ and f_E. White areas in the plots indicate that there were 0 observations in that portion of the feature space. The color scale saturates when there are more than 75 half-hourly observations in a given portion of the feature space. Some outliers are outside of the plotted range.
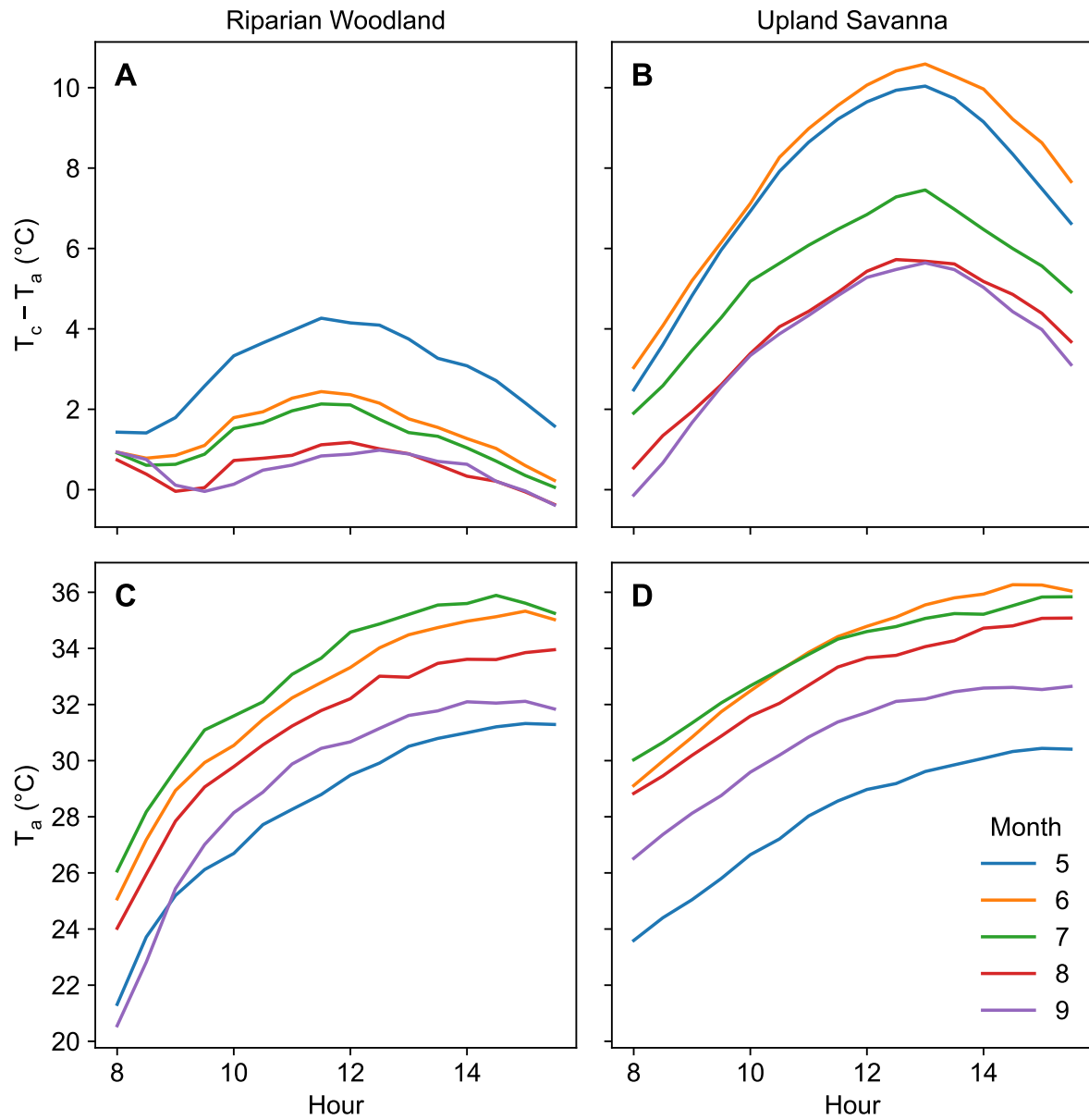
Figure 2.5: Diurnal and seasonal climatology of $T_c - T_a$ (a,b) and T_a (c,d) in the riparian woodland (a,c) and upland savanna (b,d). The colored lines represent the mean values for each time of day, grouped by month of the growing season. A comparable figure for f_E, r_H, and Q_a is located in Appendix B.
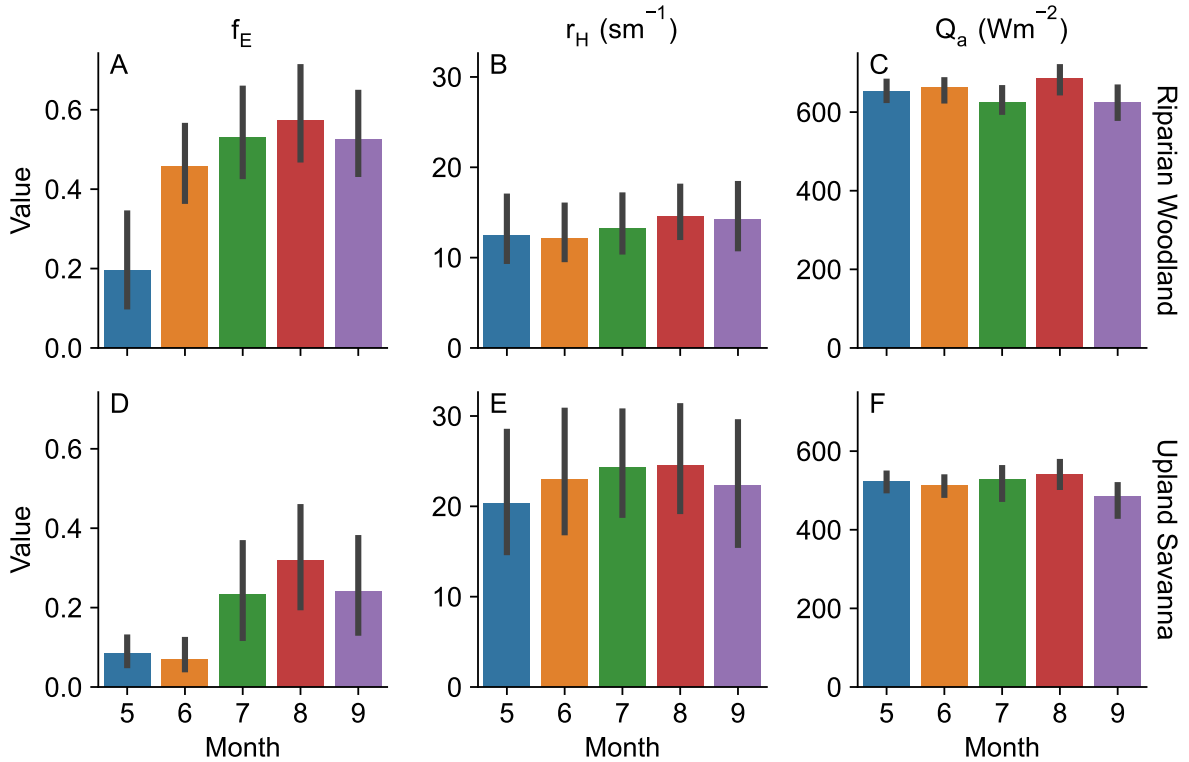
Figure 2.6: Seasonal climatology of evaporative fraction (f_E), resistance to sensible heat flux (r_H), and available energy (Q_a) in the riparian woodland (a-c) and upland savanna (d-f). The colored bars represent the median values for each month of the growing season. The black vertical bars represent the interquartile range. The Q_a values are limited to observations from 12:00 local time.

Drivers of leaf temperature

Seasonal climatologies of f_E, r_H, and Q_a revealed seasonal changes in the environmental variables that drive $T_c - T_a$. The f_E exhibited the most pronounced seasonal trends and generally tracked the onset of the monsoon. In the riparian woodland, median f_E increased from 0.2 in May to 0.57 in August. In the upland savanna, median f_E remained low in May and June (0.08 and 0.07, respectively) and increased to 0.32 in August. At both sites, r_H exhibited a much less pronounced seasonal trend. Monthly median r_H values ranged from 12.1 to 14.6 sm^{-1} in the riparian woodland and 20.4 to 24.6 sm^{-1} in the upland savanna. Likewise, median monthly Q_a (measured at 12:00 local

time) exhibited little seasonal trend and ranged from 604 to 652 Wm^{-2} in the riparian woodland and 501 to 528 Wm^{-2} in the upland savanna. The greater values of Q_a in the riparian woodland are likely due to the greater canopy cover with lower albedo as well as smaller G flux. The median albedos were 9.3% and 15.2% in the riparian woodland and upland savanna, respectively. The median G fluxes were 59 Wm^{-2} and 119 Wm^{-2}, respectively.

The r_H term can also be calculated directly from temperature measurements by inverting Equation B.6 (Verhoef et al., 1997). The inversion method yielded a different seasonal trend, indicating that r_H decreased throughout the growing season. However, the values of r_H were generally similar using both methods (Figure B.7).

Spearman rank correlation was used to quantify the sensitivity of observed T_c to the individual variables that drive T_c, including T_a, Q_a, r_H, and f_E. As expected, T_a was highly correlated with T_c in all months at both sites ($r_s \geq 0.75$; Figure B.8). We controlled for T_a by repeating the analysis with $T_c - T_a$ values. There were coherent seasonal trends in the correlations between $T_c - T_a$ and Q_a, r_H, and f_E at both sites (Figure 2.7). In the riparian woodland, $T_c - T_a$ was highly correlated with f_E early in the growing season ($r_s = -0.79$ in May), but the sensitivity to f_E decreased as monsoonal moisture accumulated in the ecosystem ($r_s = -0.14$ in September). The sensitivity to Q_a peaked in the middle of the summer ($r_s = 0.71$ in July) and was lower at the beginning and end of the growing season. The sensitivity to modeled r_H was negligible in all months ($r_s \leq 0.1$). In the upland savanna, $T_c - T_a$ was more sensitive to Q_a in May and June ($r_s = 0.56$ and 0.58, respectively) and more sensitive to f_E after the onset of the monsoon in July. The sensitivity to f_E peaked in July ($r_s = -0.68$) and decreased at the end of the growing season. The sensitivity to modeled r_H was weak in all months ($-0.15 \leq r_s \leq 0.09$).

Spearman rank correlation was also used to quantify the sensitivity of observed Q_a,

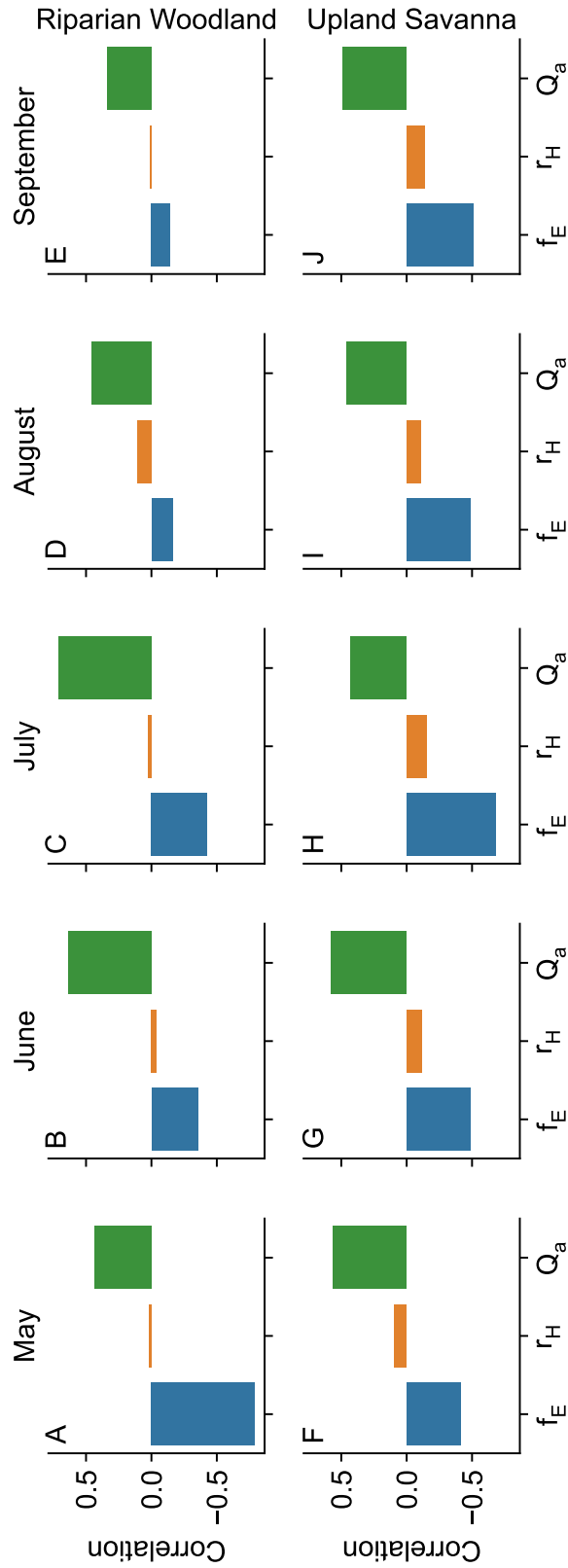Figure 2.7: Spearman rank correlations between $T_c - T_a$ and evaporative fraction (f_E), resistance to sensible heat flux (r_H), and available energy (Q_a) at the riparian woodland (a-e) and upland savanna (f-j). The colored bars represent the correlations for each month of the growing season.

Table 2.1: Spearman rank correlations between observed Q_a, r_H, and f_E and environmental variables measured by the flux towers, including shortwave insolation (SW↓), vapor pressure deficit (VPD), wind speed (u), and soil water content (SWC) for the riparian woodland and upland savanna.

	Riparian Woodland				Upland Savanna			
	SW↓	VPD	u	SWC	SW↓	VPD	u	SWC
f_E	-0.39	-0.15	-0.36	0.02	-0.36	-0.34	-0.40	0.76
r_H	-0.15	-0.21	-0.73	0.12	-0.08	-0.02	-0.66	0.04
Q_a	0.86	0.27	0.15	-0.02	0.91	0.20	0.27	0.07

r_H, and f_E to environmental variables measured by the flux towers, including SW↓, VPD, u, and SWC. The f_E term was negatively correlated with SW↓ and VPD at both sites (Table 2.1). The f_E term was also negatively correlated with u, potentially because u often peaks late in the afternoon when VPD is highest. The f_E term was negligibly correlated with SWC in the riparian woodland ($r_s = 0.02$) but strongly correlated with SWC in the upland savanna ($r_s = 0.76$), likely due to contrasting groundwater availability at the two sites (Mayes et al., 2020; Sabathier et al., 2021). The u term was the dominant driver of r_H at both sites ($r_s = -0.73$ and -0.66, respectively), which was expected given that u is encoded in the r_H calculations. SW↓ was the dominant driver of Q_a ($r_s = 0.86$ and 0.91, respectively). The analysis of the environmental variables also explains the negative correlations between $T_c - T_a$ and r_H at both sites (Figure 2.7), which were contrary to expectations. The negative correlations likely emerge from the fact that u has negative correlations with both f_E and r_H (Table 2.1), yet f_E and r_H have opposing effects on $T_c - T_a$. Thus, the effect of u on f_E and $T_c - T_a$ is likely large enough to confound the relationship between r_H and $T_c - T_a$.
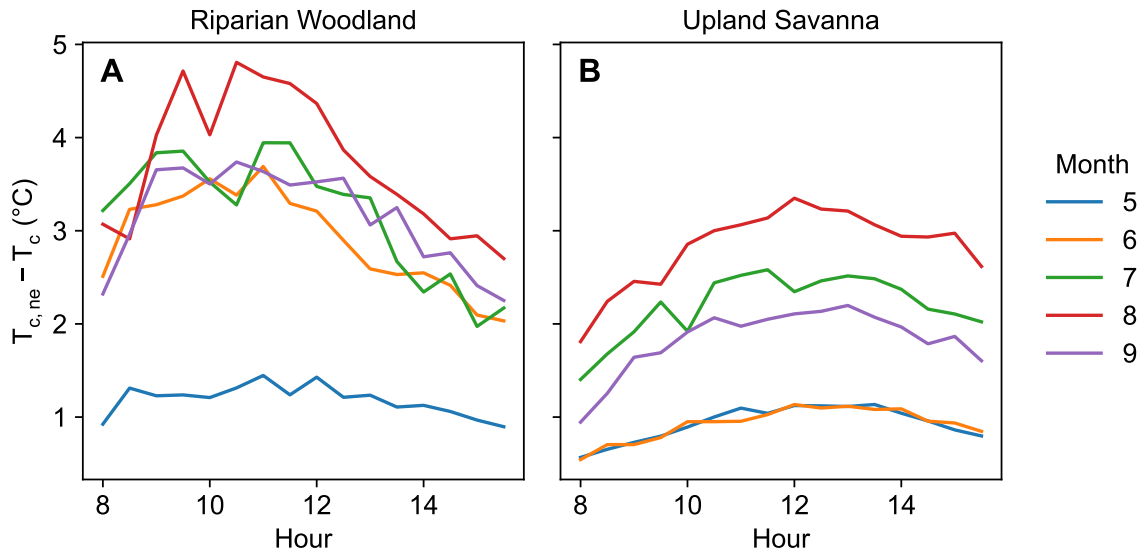
Figure 2.8: Diurnal and seasonal climatology of modeled $T_{c,ne} - T_c$, which indicates the change in T_c due to evaporative cooling of the leaf surface. The colored lines represent the mean values for each time of day, grouped by month of the growing season, for the riparian woodland (a) and upland savanna (b).

2.3.6   Evaporative cooling

The modeled values of T_c and $T_{c,ne}$ revealed the change in T_c that can be attributed to evaporative cooling of the canopy. The $T_{c,ne} - T_c$ values were generally greater in the riparian woodland than the upland savanna (Figure 2.8). At both sites, seasonal variability in $T_{c,ne} - T_c$ tracked the seasonal trends of f_E. The smallest values of $T_{c,ne} - T_c$ occurred in May at the riparian woodland and in May and June at the upland savanna. The largest values of $T_{c,ne} - T_c$ (i.e., the most evaporative cooling) occurred in August at both sites. In the riparian woodland, the maximum daily climatological $T_{c,ne} - T_c$ was 1.45 °C in May and 4.81 °C in August. In the upland savanna, the maximum daily climatological $T_{c,ne} - T_c$ was 1.14 °C in May and 3.35 °C in August. The dip in $T_{c,ne} - T_c$ values in the middle of the morning is likely a measurement or modeling artifact, potentially caused by shading of the flux tower sensors.

2.3.7 Impact of evaporative cooling on leaf respiration

Leaf light respiration ($R_{L,light}$) was predicted using modeled values of T_c and $T_{c,ne}$. The difference between the two predictions (ΔR_L) indicates the change in $R_{L,light}$ that is attributable to evaporative cooling of the canopy. In the riparian woodland, ΔR_L exhibited consistent seasonal patterns each year, with the lowest values occurring during the pre-monsoon period in May and the largest values occurring in August (Figure 2.9). In May, evaporative cooling decreased $R_{L,light}$ by 5-11%. In August, evaporative cooling decreased $R_{L,light}$ by 21-24%. In the upland savanna, ΔR_L varied much more sporadically, likely due to the dependence of the ecosystem on water inputs from precipitation. The smallest values of ΔR_L typically occurred in May and June of each year, and the largest values typically occurred in August. In May, evaporative cooling decreased $R_{L,light}$ by 4-11%. In August, evaporative cooling decreased $R_{L,light}$ by 7-28%. The largest value of ΔR_L occurred in July 2008, when evaporative cooling decreased $R_{L,light}$ by 31%. It is important to note the difference in sample size at the two study sites (3 years for the riparian woodland vs. 11 years for the upland savanna) due to the limited measurements of $SW\downarrow$, $SW\uparrow$, and $LW\downarrow$ in the riparian woodland, which may account for some of the contrasting variability.

2.4 Discussion

We have presented a novel model to predict leaf temperature (T_L) as a linearized function of the evaporative fraction (f_E). The model predictions and empirical observations presented here demonstrate that evapotranspiration reduces T_L by consuming energy that would otherwise be partitioned into sensible heat flux. The model predicts that $T_L - T_a$ varies as a linear function of f_E when all other variables are held constant. The model also predicts that $T_L = T_a$ when $f_E = 1$. When $f_E < 1$, T_L theoretically
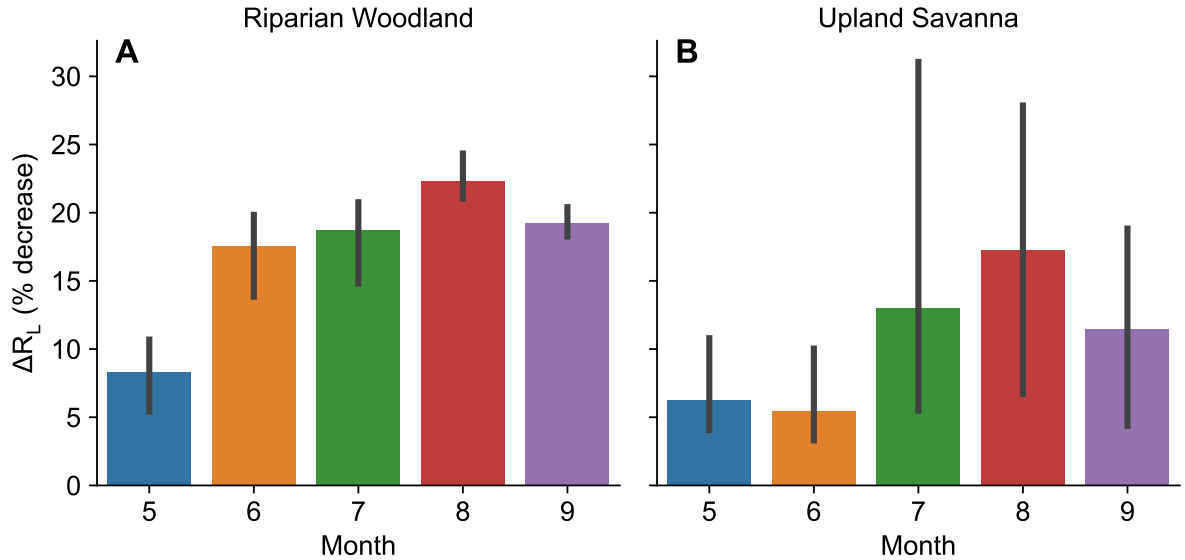
Figure 2.9: Monthly mean decrease in daytime leaf respiration (ΔR_L) that is attributable to evaporative cooling for the riparian woodland (a) and upland savanna (b). The black vertical bars indicate the range of monthly mean ΔR_L values for individual years. There are 3 years of data for the riparian woodland and 11 years of data for the upland savanna.

varies as a function of Q_a and r_H. The theoretical predictions from the energy balance model were tested using canopy-scale measurements of leaf temperature (T_c) from two flux towers with contrasting water availability. At both sites, T_c converged to T_a when f_E approached 1. The mechanistic model presented in Equation 2.7 exhibited strong model fit at both sites. Our findings are also consistent with a multi-site synthesis reported by Panwar et al. (2020), who demonstrated that the difference between surface temperature and air temperature was negatively correlated with f_E across a variety of ecosystems.

2.4.1 Environmental controls on T_c

The flux tower observations suggest that water availability plays an important role in regulating f_E and its impact on T_c. The riparian woodland has consistent access to shallow groundwater (depth to groundwater $\approx$ 10 m), which provides a persistent source

of water that is decoupled from the local precipitation regime on short time scales. The upland savanna does not have access to groundwater (depth to groundwater > 100 m) and is thus reliant on water inputs from monsoonal precipitation during the growing season. As a result, f_E was decoupled from near-surface SWC in the riparian woodland ($r_s = 0.02$) but strongly coupled to SWC in the upland savanna ($r_s = 0.76$). The enhanced water availability in the riparian woodland resulted in an earlier increase in f_E in the late spring and higher values of f_E throughout the growing season compared to the upland savanna (Figure 2.6).

The differences in f_E at the two sites resulted in different magnitudes of evaporative cooling throughout the growing season. In the riparian woodland, $T_c - T_a < 2$ °C for much of the growing season, while in the upland savanna T_c consistently exceeded T_a by as much as 10 °C (Figure 2.5). The seasonal patterns of $T_c - T_a$ matched the seasonal patterns in f_E at both sites. That being said, the strength of the correlation between $T_c - T_a$ and f_E in the riparian woodland decreased throughout the growing season, suggesting that Q_a, and not water availability, was the primary driver of riparian T_c by the end of the growing season (Figure 2.7). In the upland savanna, $T_c - T_a$ was most strongly correlated with f_E in the middle of the growing season during peak monsoonal precipitation and less strongly correlated with f_E during the drier periods at the beginning and end of the growing season.

At low values of f_E, $T_c - T_a$ is largely regulated by non-evaporative cooling processes (Muller et al., 2021, 2023). The efficiency of non-evaporative cooling is determined by the resistance to sensible heat flux (r_H). At a leaf scale, r_H is a function of leaf size, leaf structure, and the wind speed across the leaf surface (Balding and Cunningham, 1976; Jones, 2014; Leigh et al., 2017). At a canopy scale, r_H is also a function of vegetation cover and vegetation structure, which drive turbulent mixing (Yang and Friedl, 2003; Rigden et al., 2018). The upland savanna experienced a larger range of $T_c - T_a$ values at

low values of f_E because there was a larger range of r_H values under those conditions. In the riparian woodland, f_E and r_H covaried more strongly, resulting in a smaller range of $T_c - T_a$ values at low values of f_E. Interestingly, the upland savanna experienced higher wind speeds and likely had smaller leaves (Stromberg et al., 1993), which are typically associated with more efficient heat transfer, but the riparian woodland had lower modeled values of r_H. This suggests that turbulent mixing at a canopy scale played an important role in regulating r_H, which is consistent with previous analyses of r_H across different vegetation types (Rigden et al., 2018; Young et al., 2021).

2.4.2   Limited homeothermy

The mechanistic relationship between T_L and T_a has received considerable attention in literature (Cavaleri, 2020, and references therein), with various studies arguing that plants exhibit either limited homeothermy ($T_L < T_a$ at high values of T_a), poikilothermy ($T_L \cong T_a$), or megathermy ($T_L > T_a$ at high values of T_a). We found that the riparian woodland generally exhibited poikilothermy. The slope of the relationship between T_c and T_a was close to 1 ($\beta = 0.92$) and there were few observations where $T_c < T_a$, even at high values of T_a. The upland savanna exhibited megathermy; the slope of the relationship between T_c and T_a was greater than 1 ($\beta = 1.17$) and T_c consistently exceeded T_a. Neither site in this study exhibited a clear signal of limited homeothermy. Moreover, the mechanistic model of T_L always predicts that $T_L \geq T_a$ when $Q_a \geq 0$ W m^{-2} and $f_E \leq 1$. Even if stomatal conductance is not limiting, there is by definition not enough Q_a in the system to increase λE to levels that result in $T_L < T_a$ under normal conditions. It follows from Equation 2.6 that $T_L < T_a$ can only occur if $f_E > 1$. Previous studies have demonstrated that $f_E > 1$ only occurs briefly around sunrise and sunset when H is negative and λE is positive, a time of day when the magnitudes of

energy fluxes are small. The value of f_E is somewhat constant during daylight hours and typically substantially less than 1 (Crago, 1996; Gentine et al., 2007, 2011). Conditions where $f_E > 1$ can also occur as a result of the "oasis effect" whereby the advection of dry air over well-watered vegetation creates a land-atmosphere feedback that causes λE to exceed Q_a (Baldocchi et al., 2016). The oasis effect is most commonly associated with rice paddies and wetlands in semi-arid climates, but it is not clear how often the effect actually occurs (Baldocchi et al., 2016).

Despite the lack of theoretical or empirical support for limited homeothermy in the data examined here, observations where $T_L < T_a$ are commonly reported in literature. Some researchers have suggested that observations of limited homeothermy are due to systematic errors from certain types of *in situ* sensors (Still et al., 2019b). However, observations where $T_L < T_a$ have also been reported in studies that measure T_L using infrared radiometers (e.g., Idso et al., 1981; Jackson et al., 1981; Kar and Kumar, 2007; Ballester et al., 2013; Blonder et al., 2020). Thus, there is an apparent paradox whereby observations of $T_L < T_a$ seem highly unlikely given fundamental energy balance constraints (Equation 2.6), but are nonetheless common. Blonder and Michaletz (2018) demonstrated from energy balance theory that limited homeothermy can only occur when stomatal conductance is high and r_H is low. Other research has examined non-steady state T_L dynamics, which are not explored here (e.g., Leigh et al., 2017). The relationship between f_E and T_L established by this study represents another novel constraint on leaf thermoregulation via limited homeothermy. Further theoretical and empirical research is needed to constrain the conditions that result in observations where $T_L < T_A$, especially given the substantial disagreement over how frequently leaf thermoregulation actually occurs in nature (e.g., Blonder et al., 2020; Still et al., 2022).

2.4.3   Plant carbon balance

Constraining the mechanistic relationship between T_L and T_a is of critical importance for modeling ecosystem responses to anthropogenic climate change. Leaf energy balance and T_L serve as fundamental constraints on the selection and adaptation of plant traits (Michaletz et al., 2015, 2016), which are generally assumed to maximize net carbon uptake while controlling for the risk of plant hydraulic failure (Wolf et al., 2016; Sperry et al., 2017; Mencuccini et al., 2019). Previous trait-based research has focused on the role of stomatal conductance in maximizing photosynthetic assimilation via biochemical fixation of carbon (Cowan and Farquhar, 1977; Medlyn et al., 2011). Here we demonstrate that stomatal conductance also alters net carbon uptake via the impact of evaporative cooling on R_L. In both the riparian woodland and upland savanna, evaporative cooling of the leaf surface often reduced R_L by *ca.* 15% in the middle of the growing season. Reduced T_L from evaporative cooling would also be expected to keep T_L closer to the photosynthetic optimum in hot environments, maximizing photosynthetic assimilation (Roden and Pearcy, 1993; Medlyn et al., 2002). For example, Uni et al. (2022) demonstrated that a reduction in T_L from 40 °C to 35 °C would increase photosynthetic assimilation by 42%. Their study analyzed *Acacia tortilis*, a species that is structurally and functionally similar to *P. velutina*. The regulation of T_L by stomatal conductance represents an important linkage between plant water and carbon cycles that has received little attention in literature (but see Michaletz et al., 2015, 2016) and may alter predictions of optimal plant traits and behavior. All other factors held constant, the data examined here suggest that high levels of λE will enhance net carbon uptake by reducing R_L, which may marginally favor high risk-high reward hydraulic strategies in dryland vegetation (e.g., Hultine et al., 2020; Williams et al., 2022).

2.4.4 Thermal remote sensing

Equation 2.7 also provides a physical basis to interpret thermal remote sensing measurements (Mallick et al., 2022). Tower-mounted infrared radiometers are a reliable proxy for airborne and satellite thermal sensors, which can measure surface temperature over broad spatial scales. Thermal remote sensing is widely used to monitor agricultural productivity (Jones et al., 2009; Maes and Steppe, 2012) and manage water resources (Anderson et al., 2012). Our study joins other recent efforts to unify plant traits and thermal measurements, which will likely yield novel insights into ecosystem processes at leaf to global scales (Still et al., 2019a, 2021; Farella et al., 2022).

2.5 Conclusion

The mechanistic relationships between water, energy, and carbon fluxes at the leaf surface are of considerable importance for predicting the responses of terrestrial ecosystems to anthropogenic climate change. The model presented here constrains the mechanistic relationship between T_L and T_a and provides a framework to quantify evaporative cooling of the leaf surface. Importantly, the model reveals that $T_L - T_a$ varies as a linear function of f_E and that $T_L - T_a = 0$ °C when $f_E = 1$. The model predictions were validated using measurements of canopy-scale leaf temperature (T_c) from two flux towers. Seasonal variability in measured T_c was primarily driven by f_E, although Q_a also played an important role in regulating T_c in well-watered conditions. Neither the model predictions nor the empirical observations provided evidence for regimes where T_L is substantially less than T_a. Future work is needed to understand the conditions that result in empirical observations of $T_L < T_a$ in croplands. Our analysis also reveals that evaporative cooling of the leaf surface has important functional implications for plant carbon cycling. Evaporative cooling substantially reduced R_L at both study sites. The impact of evaporative cooling

on R_L may affect predictions of optimal plant traits and behavior under future climate scenarios.

Chapter 3

Vertical profiles of leaf temperature and photosynthesis within forest canopies

3.1   Introduction

Atmospheric conditions regulate the rates of mass and energy exchange between plant tissues and the surrounding environment. The amount of available energy, which is driven by solar radiation, and the turbulent transport of water vapor, which is driven by wind speed, regulate potential evapotranspiration, which plays an important role in determining plant water use and carbon uptake (Fisher et al., 2011). Mass and energy exchange at the leaf surface also influence leaf temperature (Kibler et al., 2023), which regulates the rates of leaf biochemical reactions, including photosynthesis and respiration (Medlyn et al., 2002; Heskel et al., 2016). Atmospheric conditions thus play a critical role in regulating plant physiological function and mediating the interactions between water, energy, and carbon fluxes in terrestrial ecosystems.

In forest ecosystems, there are strong vertical gradients of atmospheric conditions within tree canopies (De Frenne et al., 2021; Vinod et al., 2023). Leaves and branches attenuate solar radiation downward through the canopy (Fotis and Curtis, 2017; Béland and Baldocchi, 2021), while canopy structural complexity attenuates the wind speed (Moon et al., 2019). The resulting variability in atmospheric conditions creates distinct microclimates within tree canopies, such that individual leaves growing on the same plant may experience vastly different environmental forcings (Song et al., 2021). Given that leaf physiological function is regulated by atmospheric conditions at the leaf surface, there are likely strong vertical gradients of evapotranspiration, leaf temperature, and photosynthesis within forest canopies. The magnitudes of these gradients likely play an important role in regulating ecosystem water use and carbon uptake. Vertical attenuation of environmental forcings will also affect how forest ecosystems respond to anthropogenic climate change. Many ecosystems will experience increased radiative forcing (Stephens and L'Ecuyer, 2015), increased air temperatures, and decreased water availability under climate change (McDowell et al., 2020; Williams et al., 2020). Canopy microclimates will likely play a critical role in mitigating heat and water stress for trees (De Frenne et al., 2021), and they may also serve as refugia that protect the biodiversity of other plant and animal species (Wolf et al., 2021; Kim et al., 2022).

Despite the functional importance of within-canopy variability in radiation, air temperature, and wind speed, the vertical profiles of environmental variables remain poorly constrained in both models and measurements. Many analyses of plant physiological function rely on top-of-canopy values to predict the rates of mass and energy exchange in forest ecosystems. Likewise, measurements from remote sensing platforms and meteorological towers almost always measure the outsides of tree canopies, which may not be representative of the canopy as a whole (Stark et al., 2012; Miller et al., 2021). Relying on these models and measurements to constrain plant functional traits may lead to biased

predictions of how forest ecosystems will respond to anthropogenic climate change. Thus, there is a critical need to develop mechanistic models that represent vertical variation in canopy environmental conditions, which will improve predictions of plant physiological function and may alter estimates of optimal leaf traits (Wright et al., 2017) and carbon allocation strategies (Trugman et al., 2019) based on canopy position.

Variability in canopy environmental conditions can also affect leaf exposure to critical temperatures that inhibit plant carbon uptake. Photosynthetic assimilation decreases when leaf temperature exceeds *ca.* 30 °C (Medlyn et al., 2002), and leaf respiration increases exponentially with increasing temperature (Heskel et al., 2016). Likewise, when leaf temperature exceeds *ca.* 45 °C, leaves experience irreversible damage to photosystem II that permanently inhibits leaf photosynthetic function (Havaux, 1992). Leaf trait coordination (i.e., adapting or evolving combinations of traits that optimize physiological function) generally enables species to avoid thermal damage within their normal ranges of growing conditions (Michaletz et al., 2016; Leigh et al., 2017), but non-stationary climate change and the increasing frequency of extreme heat events may outpace plants' capacity to adapt to environmental change in the coming decades (Diffenbaugh and Ashfaq, 2010; Cook et al., 2020). Quantifying the sensitivity of leaf physiological function to different combinations of leaf traits will provide insights into which adaptations will enhance forest resilience under anthropogenic climate change, especially in the portions of forest canopies where leaves experience the most environmental stress.

In this analysis, we examine whether forest canopies create novel microclimates that enhance plant productivity and increase resilience to changing environmental conditions. We create a mechanistic model to predict within-canopy environmental conditions as a function of cumulative leaf area index. We then predict vertical gradients of leaf temperature and photosynthesis extending through the canopy. We also examine whether leaf trait coordination enables trees to avoid critical leaf temperatures that would cause

thermal damage to photosynthetic infrastructure. In doing so, we answer three research questions:

1. How do within-canopy microclimates predicted by known physical processes affect the vertical profile of leaf temperature within forest canopies? How does the vertical profile of leaf temperature vary diurnally?

2. How do the vertical profiles of leaf temperature and photosynthetically active radiation affect the vertical profile of net photosynthesis within forest canopies? How does the vertical profile of net photosynthesis vary diurnally?

3. Do trees optimize their structural and functional traits to avoid damaging leaf temperatures across forest biomes?

Answering these research questions will provide insights into the spatial distribution of physiological stress within forest canopies under anthropogenic climate change. Answering the first two research questions will reveal where in the canopy leaves will experience the most stress under warming and drying conditions. Answering the third research question will reveal the types of leaf physiological adaptations that will be needed to adapt to environmental change, especially in the most stressed parts of forest canopies.

3.2 Methods

3.2.1 Leaf temperature model

Following Kibler et al. (2023), leaf temperature (T_L) was modeled as a linear function of the evaporative fraction (f_E):

$$T_L = T_a + \frac{Q r_H}{\rho c_p}(1 - f_E) \tag{3.1}$$

where T_a is air temperature, Q is available energy, r_H is aerodynamic resistance to sensible heat flux, ρ is air density, c_p is the specific heat of air, and f_E is the evaporative fraction. The Q term is regulated by leaf-level net radiation:

$$Q = SW\downarrow - SW\uparrow + LW\downarrow - LW\uparrow \tag{3.2}$$

where $SW\downarrow$ is shortwave incoming radiation, $SW\uparrow$ is shortwave outgoing radiation, $LW\downarrow$ is longwave incoming radiation, and $LW\uparrow$ is longwave outgoing radiation. The f_E term represents the proportion of available energy that is consumed by latent heat flux (λE):

$$f_E = \frac{\lambda E}{Q} \tag{3.3}$$

The vertical profile of T_L within a canopy was estimated by attenuating the values of the Q, λE, and r_H downward through the canopy as a function of leaf area index (L). Available energy at height z was modeled using the Bouguer-Beer-Lambert Law:

$$Q_z = Q_h \exp(-k_Q L_{z \to h}) \tag{3.4}$$

where subscript z denotes the value at the measurement height and subscript h denotes the value at the top of the canopy. The k_Q term is the extinction coefficient for all-wave net radiation, and $L_{z \to h}$ is the cumulative leaf area index between height z and the top of the canopy. The value of k_Q was set to 0.592 based on measurements by Baldocchi et al. (1984). The f_E term was assumed to be constant at all heights, such that λE was downregulated proportionally to Q. As a result, the modeled value of λE was highest at the top of the canopy and lowest at the bottom of the canopy. The r_H term was estimated as a function of wind speed (u) and the leaf characteristic dimension (d):

70

$$r_H = \frac{1}{b \left(\frac{u_z}{d} \right)^{0.5}} \tag{3.5}$$

The coefficient b was set to a value of 0.00662 following Jones (2014). The d term represents the average path length of wind blowing over a leaf. The value of d was estimated as the width of the leaf along the shortest axis (Gurevitch and Schuepp, 1990; Leigh et al., 2017). It can also be estimated as a function of leaf area (A_L) following Wright et al. (2017):

$$d = \sqrt{\frac{A_L}{1.5}} \tag{3.6}$$

where d is measured in m and A_L is measured in m^2. The vertical profile of u within the canopy was estimated using the formula proposed by Cionco (1972, 1978):

$$u_z = u_h \exp \left[a \left(\frac{z}{h} - 1 \right) \right] \tag{3.7}$$

The a term is a coefficient that was estimated as a function of $L_{z \to h}$ following Yi (2008):

$$a = \frac{L_{z \to h}}{2} \tag{3.8}$$

Empirical analyses have demonstrated that T_a varies relatively little along vertical gradients within forest canopies (Vinod et al., 2023), so T_a was assumed to be constant at all heights, such that $T_{a,z} = T_{a,h}$. The values of ρ, c_p, and d were also assumed to be constant at all heights.

Equations 3.1-3.8 can be used to estimate T_L at the top of the canopy ($z/h = 1$). They can also be used to estimate T_L below a certain number of layers of leaves ($z/h = 0$), which are represented by the $L_{z \to h}$ term. The required input variables are top-of-canopy measurements of T_a, Q, u, λE, ρ, c_p, and d.

71

3.2.2   Photosynthesis model

Net leaf photosynthesis (A_n) was modeled as the minimum of the photosynthesis rates limited by Rubisco activity (A_c) and RuBP regeneration (A_j) minus leaf respiration (Farquhar et al., 1980; Medlyn et al., 2002):

$$A_n = \min(A_c, A_j) - R_{L,light} \tag{3.9}$$

where $R_{L,light}$ is the rate of leaf respiration under light-inhibited conditions. Equations 3.9-3.17 were calculated following Medlyn et al. (2002). The A_c term was modeled as:

$$A_c = \frac{V_{cmax}(C_i - \Gamma^*)}{\left[C_i + K_c \left(1 + \frac{O_i}{K_o} \right) \right]} \tag{3.10}$$

where V_{cmax} is the maximum rate of Rubisco activity, C_i is the intercellular concentration of CO_2, Γ^* is the CO_2 compensation point, K_c is the Michaelis–Menten coefficient of Rubisco activity for CO_2, O_i is the intercellular concentration of O_2, and K_o is the Michaelis–Menten coefficient of Rubisco activity for O_2. The C_i term was calculated as a fixed fraction of the ambient atmospheric CO_2 concentration (C_a):

$$C_i = 0.7 C_a \tag{3.11}$$

The Γ^*, K_c, and K_o parameters were estimated using Arrhenius-type functions of leaf temperature measured in K (T_k). We used functions that were calibrated by Bernacchi et al. (2001):

$$\Gamma^* = 42.75 \exp \left[\frac{37830(T_k - 298)}{298 R T_k} \right] \tag{3.12}$$

$$K_c = 404.9 \exp\left[\frac{79430(T_k - 298)}{298RT_k}\right] \tag{3.13}$$

$$K_o = 278.4 \exp\left[\frac{36380(T_k - 298)}{298RT_k}\right] \tag{3.14}$$

The A_j term was modeled as:

$$A_j = \left(\frac{J}{4}\right) \times \left(\frac{C_i - \Gamma^*}{C_i + 2\Gamma^*}\right) \tag{3.15}$$

where J is the rate of electron transport. The value of J was calculated as a quadratic function of the maximum rate of electron transport (J_{max}):

$$\theta J^2 - (\alpha P + J_{max})J + \alpha P J_{max} = 0 \tag{3.16}$$

where θ is the shape of the photosynthesis response curve to light, α is the quantum yield of electron transport, and P is the photosynthetic photon flux density. The values of V_{cmax} and J_{max} were estimated using a modified Arrhenius function of T_k (Medlyn et al., 2002):

$$f(T_k) = k_{opt}\frac{H_d \exp\frac{H_a(T_k - T_{opt})}{T_k RT_{opt}}}{H_d - H_a\left(1 - \exp\frac{H_d(T_k - T_{opt})}{T_k RT_{opt}}\right)} \tag{3.17}$$

where k_{opt} is the maximum value of the function, T_{opt} is the temperature where the maximum value occurs, H_d controls the rate of decrease when $T_k > T_{opt}$, and H_a controls the rate of increase when $T_k < T_{opt}$. The R term is the universal gas constant (8.314 J mol⁻¹ K⁻¹). We used values of k_{opt}, T_{opt}, H_d, and H_a that were derived from measurements of *Acer pseudoplatanus* by Medlyn et al. (2002).

Leaf dark respiration ($R_{L,dark}$) was estimated as a function of T_L following Heskel

et al. (2016):

$$R_{L,dark}(T_L) = R_{L,dark}(T_{ref}) * e^{0.1012(T_L - T_{ref}) - 0.0005(T_L^2 - T_{ref}^2)} \tag{3.18}$$

where $R_{L,dark}(T_{ref})$ is a reference respiration value at a reference temperature (T_{ref}). We set $R_{L,dark}(T_{ref})$ to 0.99 µmol m^{-2} s^{-1} based on measurements of 24 broadleaf tree species by Reich et al. (1998) at a T_{ref} of 25 °C. Leaf respiration is inhibited by light during the daytime, so $R_{L,dark}$ was downregulated using the formula proposed by Mathias and Trugman (2022) based on measurements by Way et al. (2015):

$$R_{L,light}(T_L) = R_{L,dark}(T_L) * (0.0039 * T_L + 0.6219) \tag{3.19}$$

Equations 3.9-3.19 enabled us to estimate A_n along a vertical profile within the canopy as a function of T_L and P. The values of T_L were calculated as described in Section 3.2.1. The value of P at height z was modeled as a function of $L_{z \to h}$ using the Bouguer-Beer-Lambert Law:

$$P_z = P_h \exp(-k_P L_{z \to h}) \tag{3.20}$$

where k_P is the extinction coefficient for P. The value of k_P was set to 0.732 based on measurements by Baldocchi et al. (1984).

3.2.3 Model limitations

The model presented here represents a simplified framework to predict vertical profiles of T_L and A_n based solely on top-of-canopy measurements. To achieve this, we hold the values of several parameters constant at all heights within the canopy. These simplifying assumptions improve the tractability of the model, especially given that the vertical

variation of many canopy traits is not well constrained in literature. For example, the value of d was held constant at all heights within the canopy. In reality, there are typically smaller leaves near the tops of tree canopies and larger leaves near the bottoms of tree canopies (e.g., Klich, 2000; Zwieniecki et al., 2004). Accounting for variability in leaf size might improve predictions of T_L and A_n at different heights within a canopy, although it is not clear how to parameterize such a model in a generalizable manner without extensive field measurements. The model also neglects vertical variability in leaf angle, which also affects leaf physiological function. In reality, leaves growing at the tops of tree canopies often have more vertical leaf angles, which reduces radiative forcing, while leaves growing near the bottoms of tree canopies often have more horizontal leaf angles, which maximizes photosynthetic light harvesting (Niinemets, 2010; Yang et al., 2023). Incorporating leaf angle variability into the model might improve predictions of T_L and A_n, although it would require a multi-layer representation of the canopy or another spatially explicit radiative transfer scheme. Photosynthetic parameters such as V_{cmax} and J_{max} also exhibit vertical variation within forest canopies. Both V_{cmax} and J_{max} are typically higher near the tops of tree canopies (e.g., Carswell et al., 2000; Lamour et al., 2023). Accounting for vertical variation in photosynthetic parameters may affect the predicted magnitude and spatial distribution of A_n within forest ecosystems (Bachofen et al., 2022).

3.2.4   Study sites

We analyzed eddy covariance data from five broadleaf forests spanning a large latitudinal gradient in North and South America. The five sites represent a wide range of climate zones and forest physiognomies. The specific sites were selected because they have long sensor data records for the input variables needed to implement the T_L and A_n

models. The site characteristics are summarized in Table 3.1.

Several filters were applied to the eddy covariance data set to remove low-quality measurements:

- selected peak growing season measurements between June and August

- selected daytime observations between 8:00 and 16:00 local time

- removed days with any measured precipitation and the day after any measured precipitation

- removed observations with low friction velocity (u_*) values

Low u_* values can cause errors in the eddy covariance measurements (e.g., Barr et al., 2013). For three of the sites, the minimum acceptable u_* value was set to the site-specific threshold reported by Barr et al. (2013). For the riparian woodland, the minimum acceptable u_* value was set to 0.2 following Kibler et al. (2023). For the tropical rainforest, the u_* value was set to 0.15 following Bonal et al. (2008).

The meteorological sensors at Willow Creek and the tropical rainforest were located far above the top of the canopy, so the u measurements for the two sites were interpolated downward to the top of the canopy by assuming a logarithmic wind profile:

$$u_h = u_z \frac{\log(h - h_d)/z_0)}{\log(z - h_d)/z_0)} \tag{3.21}$$

where h_d is the zero-plane displacement height and z_0 is the roughness length for momentum. The h_d and z_0 terms were calculated as a function of canopy height (h), such that $d = 0.64h$ and $z_0 = 0.13h$ (Jones, 2014). The sensor measurement heights (z) for the two sites were 38 m and 58 m, respectively. The canopy heights were 20.1 m and 35 m, respectively (Gaumont-Guay et al., 2009; Bonal et al., 2008). For the other three sites, the selected u measurement heights were approximately equal to the height of the canopy.

Table 3.1: Characteristics of the five study sites, including canopy height (h_c), mean annual temperature (MAT), and mean annual precipitation (MAP).

Site	FLUXNET ID	Latitude	Longitude	h_c (m)	MAT (°C)	MAP (mm)
Boreal aspen forest	CA–Oas	53.6289 °N	106.1978 °W	21.5	0.34	429
Willow Creek	US–WCR	45.8059 °N	90.0799 °W	24	4.02	787
Morgan Monroe S.F.	US–MMS	39.3232 °N	86.4131 °W	27	10.85	1032
Riparian woodland	US–CMW	31.6637 °N	110.1777 °W	7	17	288
Tropical rainforest	GF–Guy	5.2788 °N	52.9249 °W	35	25.7	3041

Table 3.2: Canopy traits used to parameterize the T_L and A_n models. The L_h value indicates the total leaf area index. The u_* value indicates the minimum u_* threshold for filtering the eddy covariance data.

Site	FLUXNET ID	d (cm)	L_h	$u*$ (ms^{-1})
Boreal aspen forest	CA-Oas	3.5[a]	4.4[b]	0.39[c]
Willow Creek	US-WCR	10.0[d]	5.3[e]	0.42[c]
Morgan Monroe State Forest	US-MMS	10.0[d]	4.5[f]	0.48[c]
Riparian woodland	US-CMW	0.8[g]	2.0[h]	0.2[i]
Tropical rainforest	GF-Guy	5.5[j]	6.0[k]	0.15[l]

Sources: a) Hogg and Hurdle (1997), b) Barr et al. (2004), c) Barr et al. (2013), d) Béland and Baldocchi (2020), e) Cook et al. (2004), f) Sulman et al. (2016), g) Stromberg et al. (1993), h) Scott et al. (2021), i) Kibler et al. (2023), j) De Azevedo Falcão et al. (2022), k) Ganivet and Gaspard (2013), l) Bonal et al. (2008)

3.2.5 Vertical profiles

The top-of-canopy flux tower measurements were used to predict the vertical profiles of Q (Equation 3.4), u (Equation 3.7), r_H (Equation 3.5), and P (Equation 3.20) within each forest canopy. The predictions revealed the vertical changes in canopy microclimate as a function of cumulative leaf area index ($L_{z \to h}$). The vertical profiles of T_L were then predicted using Equation 3.1, and the vertical profiles of A_n were predicted using Equations 3.9-3.19. The total leaf area index (L_h) and representative leaf width (d) for each site were parameterized using values reported by previous studies (Table 1). The T_a and f_E values were parameterized based on top-of-canopy flux tower measurements.

A sensitivity analysis was also conducted to quantify the extent to which leaf traits regulate the vertical profile of T_L. For the sensitivity analysis, the values of Q, T_a, ρ, and c_p were held constant at baseline conditions, and the values of u, f_E, and d were perturbed individually. The baseline conditions were set to the mean midday growing season conditions at Morgan Monroe State Forest, which is a temperate broadleaf decid-uous forest. The value of u was set to 0.5, 1.5, 2.5, and 3.5 ms^{-1}. The value of f_E was set to 0.2, 0.4, 0.6, and 0.8. The value of d was set to 2.5, 5, 10, and 20 cm. The value

of $L_{z \to h}$ varied between 0 and 4.5.

3.2.6 Leaf trait coordination

Leaves can experience thermal damage that disrupts photosynthetic function when T_L exceeds a critical temperature (T_{crit}) of *ca.* 45 °C (O'Sullivan et al., 2017). However, coordination between leaf structural (e.g., leaf width) and functional (e.g., stomatal conductance) traits can prevent leaves from experiencing critical temperatures in stressful environmental conditions. By adjusting their stomatal conductance, which regulates f_E, and leaf size, which is related to d, plants can reduce their susceptibility to leaf thermal damage. Coordination between these traits may be a critical adaptation that enables plants to maintain physiological function under changing climatic conditions.

We conducted another sensitivity analysis on Equation 3.1 to identify the combinations of environmental conditions and plant traits that result in $T_L > T_{crit}$. The value of Q was set to 250, 500, and 750 Wm^{-2}. The value of T_a was set to 20, 30, and 40 °C. The value of r_H varied between 0 and 100 sm^{-1}, and the value of f_E varied between 0 and 1. The ρ term was held constant at a representative value of 1.006 kg m^{-3}, and the c_p term was held constant at a representative value of 1010 J kg^{-1} K^{-1}.

A second analysis examined the flux tower measurements to quantify the extent to which leaf trait coordination enabled the plants at each site to avoid conditions where $T_L > T_{crit}$. We calculated the critical value of f_E that resulted in $T_L = T_{crit}$ for a given set of environmental conditions:

$$f_{E,crit} = 1 - \frac{(T_L - T_a)\rho c_p}{(SW \downarrow - SW \uparrow + LW \downarrow - \varepsilon \sigma T_k^4) r_H} \tag{3.22}$$

where ε is emissivity and σ is the Stefan-Boltzmann constant. The expanded radiation budget helps account for the feedback of T_L on Q, which occurs because T_L regulates

79

the rate of longwave emittance from a surface. For each site, the measurements were filtered to select stressful conditions where $T_a > 30$ °C. The mean values of T_a, $SW\downarrow$, $SW\uparrow$, $LW\downarrow$, ρ, and c_p were calculated from the selected measurements. Equation 3.22 was then forced with different values of r_H to identify the combinations of r_H and f_E that result in $T_L = T_{crit}$ given the prevailing environmental conditions at each site. The observed distributions of r_H and f_E across the entire data set were then compared to the $f_{E,crit}$ curves.

We also repeated the analysis with a different data set to determine whether the observed leaf trait coordination between r_H and f_E held true at a global scale. We analyzed a database compiled by Wright et al. (2017), which contains 6,499 measurements of tree leaves spanning global forest biomes. The database contains a measurement of leaf area (A_L) and geographic coordinates for each leaf. The leaf measurements generally represent sunlit leaves, which were presumably measured on the outsides of the tree canopies (see Wright et al., 2017). We calculated the values of r_H and f_E for each leaf measurement, and we compared the r_H and f_E values to the T_{crit} curves for different forest biomes produced in Section 3.2.6.

The value of r_H was calculated for each leaf measurement using Equation 3.5 (i.e., $r_H = f(u, d)$). We assumed a representative u value of 1.75 ms^{-1}, which represents the average measured midday top-of-canopy wind speed across the five flux tower study sites. The value of d was calculated as a function of the A_L value reported in the database using Equation 3.6.

We used Google Earth Engine to calculate the mean midday peak growing season value of f_E for each leaf in the database. To achieve this, we used the geographic coordinates associated with each leaf to extract values of λE and Q from ERA5-Land gridded reanalysis data (Muñoz-Sabater et al., 2021). The gridded reanalysis data has a 9 km spatial resolution and an hourly temporal resolution. For measurements north of the

equator, we selected peak growing season values from June to August. For measurements south of the equator, we selected peak growing season values from January to March. The analysis was limited to data from 2015 to 2019 for computational efficiency. The value of f_E was calculated using Equation 3.3 (i.e., $f_E = \lambda E/Q$). For each day, we selected the single value of f_E when λE reached its daily maximum, which typically occurred in the middle of the day. The mean midday peak growing season value of f_E was then calculated for each leaf. The distributions of r_H and f_E values for the 6,499 global leaf measurements were then compared to the T_{crit} curves for different forest biomes produced in Section 3.2.6.

3.3 Results

3.3.1 Canopy microclimate

Within-canopy microclimate conditions were predicted for each site by attenuating the drivers of T_L and A_n based on known physical principles. The within-canopy values for each variable were predicted as a function of cumulative leaf area index ($L_{z \to h}$) based on top-of-canopy measurements. The $L_{z \to h}$ term equals zero at the top of the canopy and equals the total leaf area index (L_h) at the bottom of the canopy. The modeled values of Q, u, and P decreased exponentially as $L_{z \to h}$ increased downward through the canopy (Figure 3.1). The modeled value of r_H, which is a function of u and d, increased exponentially as $L_{z \to h}$ increased. The mean top-of-canopy (measured) and bottom-of-canopy (modeled) conditions at 12:00 local time were compared for each site. The values are summarized in Table 3.3.

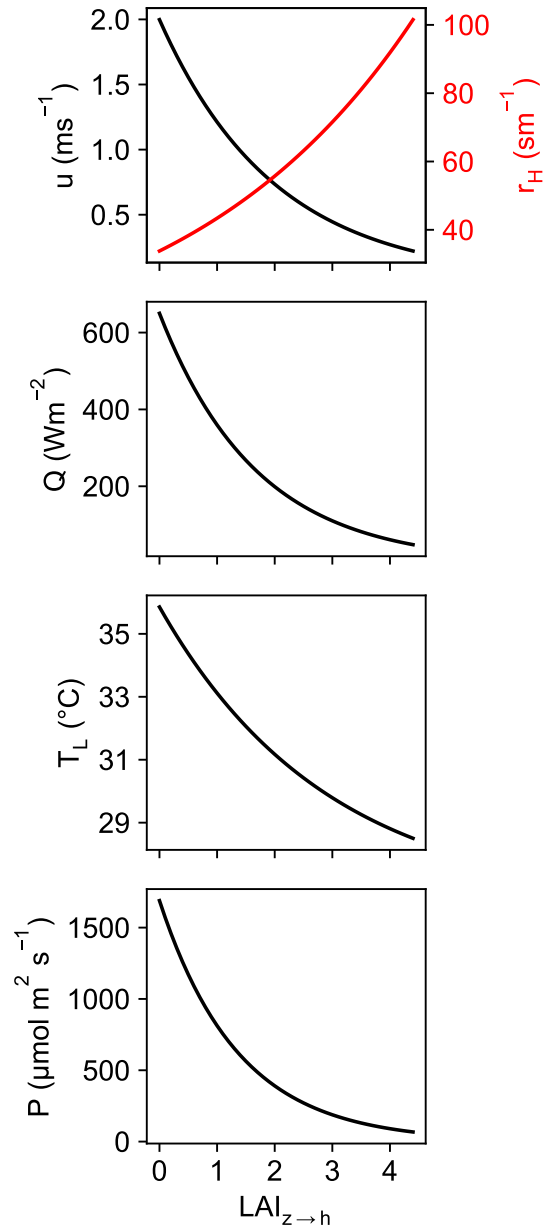Figure 3.1: Modeled vertical profiles of wind speed (u), aerodynamic resistance (r_H), available energy (Q), leaf temperature (T_L), and photosynthetic photon flux density (P) as a function of cumulative leaf area index ($LAI_{z \to h}$). An $LAI_{z \to h}$ value of 0 indicates the top of the canopy. The plotted values represent mean midday growing season conditions at Morgan Monroe State Forest.

Table 3.3: Top of canopy (measured) and bottom of canopy (modeled) values of available energy (Q), wind speed (u), resistance (r_H), and photosynthetic photon flux density (P) at the five study sites.

Site	FLUXNET ID	Q (Wm^{-2})		u (ms^{-1})		r_H (sm^{-1})		P (µmol m^{2}s^{-1})	
		Top	Bottom	Top	Bottom	Top	Bottom	Top	Bottom
Boreal aspen forest	CA-OAS	486	36	1.56	0.17	24	71	1321	147
Willow Creek	US-WCr	545	24	1.44	0.1	50	186	1509	31
Morgan Monroe S.F.	US-MMS	649	45	2.01	0.21	36	111	1689	63
Riparian woodland	US-CMW	744	228	2.04	0.75	11	18	1918	444
Tropical rainforest	GF-Guy	677	19	1.66	0.08	29	129	1603	20

3.3.2 Leaf temperature

The modeled T_L at each site decreased exponentially as $L_{z \to h}$ increased downward through the canopy (Figure 3.2a-e). The largest vertical gradients in T_L typically occurred around the middle of the day. In the boreal aspen forest (CA-Oas), the mean midday T_L value decreased from 24.48 °C at the top of the canopy to 20.19 °C at the bottom of the canopy. In Willow Creek (US-WCr), the T_L value decreased from 29.04 °C to 22.04 °C. In Morgan Monroe State Forest (US-MMS), the T_L value decreased from 36.25 °C to 28.52 °C. In the riparian woodland (US-CMW), the T_L value decreased from 36.1 °C to 33.38 °C. In the tropical rainforest (GF-Guy), the T_L value decreased from 35.39 °C to 29.9 °C. The smallest vertical gradients in T_L typically occurred at the end of the day, when large values of u substantially reduced T_L at all levels of the canopy. The differences between top-of-canopy and bottom-of-canopy T_L at 16:00 local time were 2.45, 1.49, 4.12, 0.82, and 2.22 °C for the five sites, respectively.

The values of d, u, and f_E were perturbed individually to analyze the sensitivity of the T_L model to each driver. The mean midday conditions from Morgan Monroe State Forest were used as the baseline conditions for the sensitivity analysis. The vertical gradient of T_L was positively correlated with d and negatively correlated with u and f_E (Figure 3.3). For all three variables, the differences in T_L were most pronounced at the top of the canopy ($L_{z \to h} = 0$) and approached an equilibrium value near the bottom of the canopy. Increasing the value of d from 2.5 cm to 20 cm increased the modeled top-of-canopy T_L value from 31.13 °C to 39.77 °C. Increasing the value of u from 0.5 sm^{-1} to 3.5 sm^{-1} decreased the modeled top-of-canopy T_L value from 45.92 °C to 33.54 °C. Increasing the value of f_E from 0.2 to 0.8 decreased the modeled top-of-canopy T_L value from 41.62 °C to 30.21 °C.

We also compared the T_L model predictions to T_L measurements from a wet tropical
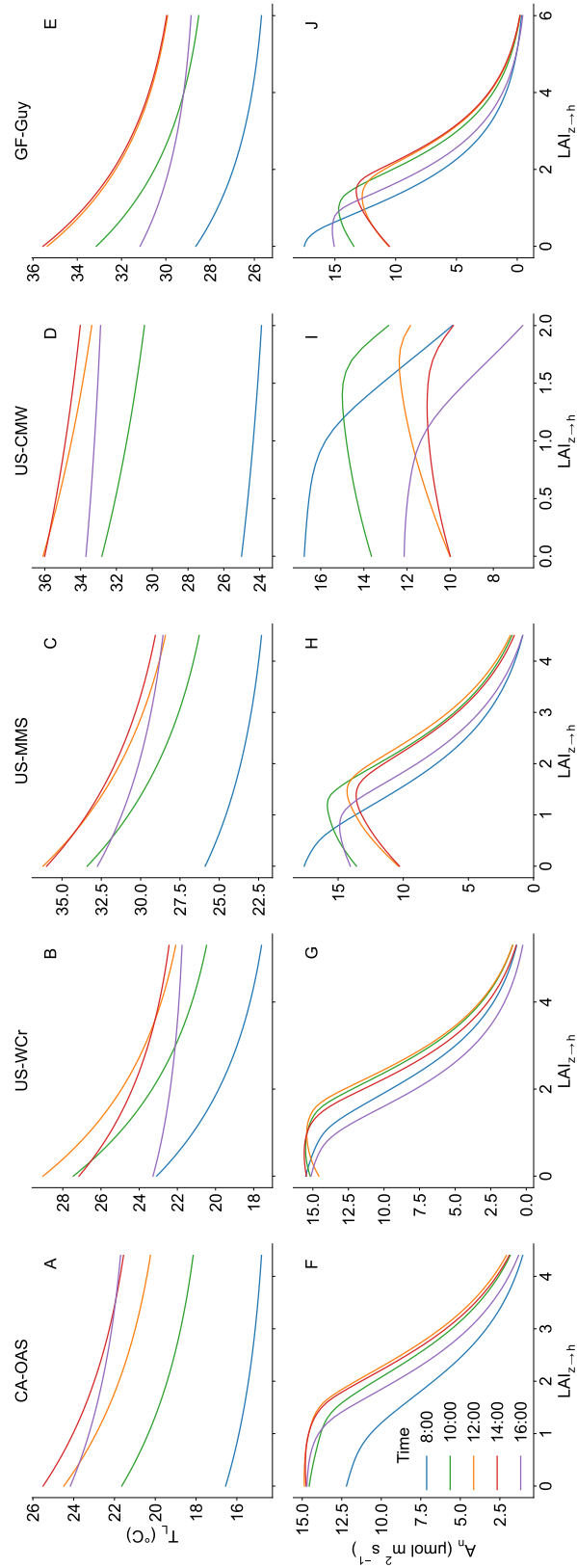
Figure 3.2: Modeled vertical profiles of leaf temperature (T_L) and net photosynthetic assimilation (A_n) as a function of cumulative leaf area index ($LAI_{z \rightarrow h}$) for the boreal aspen forest (CA-Oas), Willow Creek (US-WCr), Morgan Monroe State Forest (US-MMS), riparian woodland (US-CMW), and tropical rainforest (GF-Guy). An $LAI_{z \rightarrow h}$ value of 0 indicates the top of the canopy.
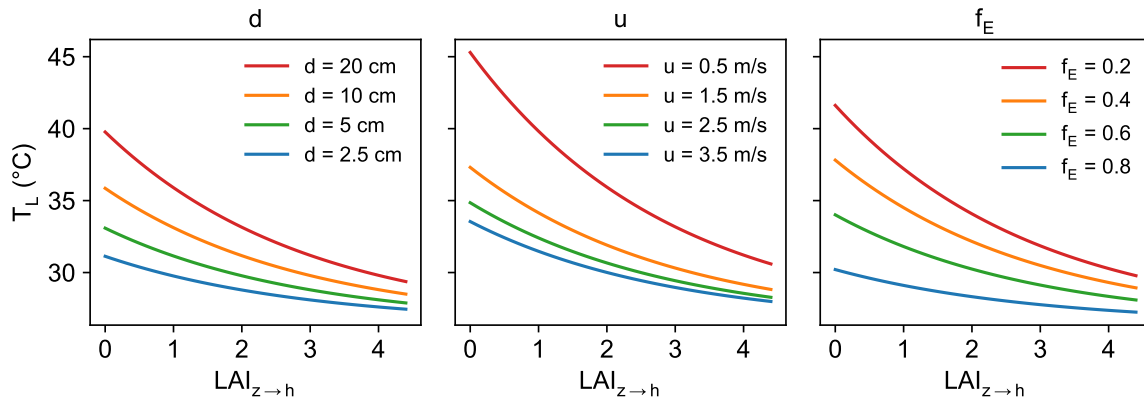
Figure 3.3: Sensitivity of the modeled vertical profiles of leaf temperature to perturbations in leaf dimension (d), top-of-canopy wind speed (u), and evaporative fraction (f_E). The data are presented as a function of cumulative leaf area index ($LAI_{z \to h}$). An $LAI_{z \to h}$ value of 0 indicates the top of the canopy. The baseline conditions for the sensitivity analysis are the mean midday growing season conditions at Morgan Monroe State Forest.

forest by Miller et al. (2021). The empirical measurements were on the same order of magnitude and exhibited many of the same trends as the T_L predictions for our study sites (Figure 3.4). Like the model predictions, the empirical measurements typically exhibited an exponential decrease in T_L downward through the canopy. The lowest values of measured T_L occurred early in the morning. The highest values and the largest vertical gradient in T_L occurred around 12:30 local time, when the difference between top-of-canopy and bottom-of-canopy T_L was 3.66 °C. The vertical gradient in T_L decreased substantially by 16:00 local time, when the difference between top-of-canopy and bottom-of-canopy T_L was only 0.76 °C. These T_L trends mirror the trends seen at the five study sites, which suggests that the model is correctly representing the physical processes that regulate T_L.
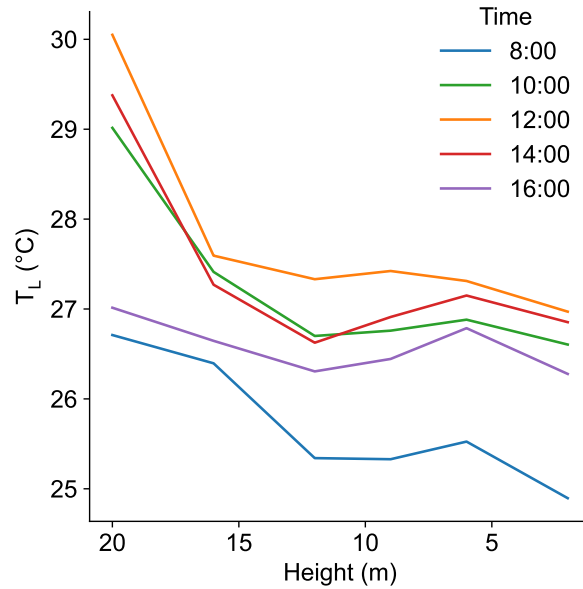
Figure 3.4: Leaf temperature measured along a vertical profile in a wet tropical forest by Miller et al. (2021). The colored lines indicate time of day. Note that the x axis is reversed to align with other plots. Data replotted from Miller et al. (2021).

3.3.3 Photosynthesis

The modeled vertical profiles of net photosynthetic assimilation (A_n) exhibited contrasting trends at the five sites (Figure 3.2f-j). The boreal aspen forest (CA-Oas) and Willow Creek (US-WCr) exhibited consistent levels of A_n when $L_{z \to h}$ was less than *ca.* 1.5, but A_n decreased rapidly when $L_{z \to h}$ was greater than 1.5. This indicates that the highest levels of photosynthesis occurred at the top of the canopy. In Morgan Monroe State Forest (US-MMS) and the tropical rainforest (GF-Guy), midday A_n initially increased until $L_{z \to h}$ was equal to *ca.* 1.5, and then it decreased rapidly. These findings suggest that the highest levels of midday photosynthesis occurred in the middle of the canopy, which was contrary to expectations. Early and late in the day the highest levels of photosynthesis occurred near the top of the canopy. In the riparian woodland (US-CMW), midday A_n increased until $L_{z \to h}$ was equal to *ca.* 2. The total leaf area index (L_h) in the riparian woodland typically does not exceed 2, so the findings suggest that

the highest levels of midday photosynthesis occurred near the bottom of the canopy, which was again contrary to expectations. The highest levels of photosynthesis at 8:00 and 16:00 occurred at the top of the canopy.

3.3.4   Leaf trait coordination

A sensitivity analysis was conducted on Equation 3.1 to identify the combinations of environmental conditions that result in damaging leaf temperatures (i.e., $T_L > T_{crit}$). The sensitivity analysis provided clear evidence of a functional trade-off between leaf resistance to heat flux (r_H) and evaporative fraction (f_E), regardless of the values of Q and T_a (Figure 3.5). The value of r_H is regulated by u and d. At low levels of r_H, T_L was always less than T_{crit}, such that there was no minimum value of f_E needed to ensure that $T_L < T_{crit}$. As r_H increased, the minimum value of f_E needed to prevent leaf thermal damage also increased. At high levels of r_H, leaves must maintain high levels of f_E to ensure that $T_L < T_{crit}$. Greater values of Q and T_a also increased the minimum values of f_E when r_H was held constant. For example, when $T_a = 30$ °C, $Q = 750$ Wm^{-2}, and $r_H = 25$ sm^{-1}, the minimum value of f_E was 0.19. When T_a increased to 40 °C, the minimum value of f_E increased to 0.73. At larger values of Q and r_H, the minimum value of f_E was even higher.

The observed distributions of top-of-canopy r_H and f_E values from the five study sites were then compared to the critical values that cause damaging leaf temperatures. The critical f_E curves were calculated based on average measurements from stressful conditions when $T_a > 30$ °C. At all five sites, the 95% percentile intervals of observed values (i.e., the observed values without outliers) occurred in portions of the feature space that result in $T_L < T_{crit}$, suggesting that trait coordination between stomatal conductance and leaf size helps prevent leaf thermal damage across forest biomes (Figure 3.6a). At

88
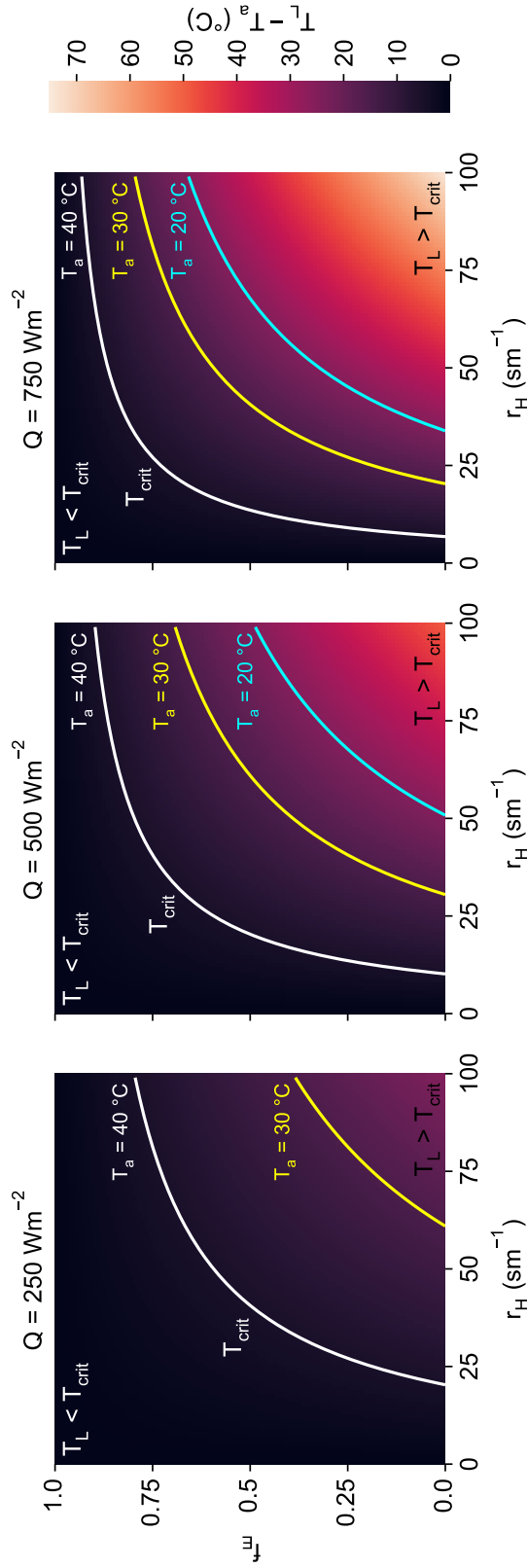
Figure 3.5: Sensitivity curves identifying the environmental conditions that result in $T_L = T_{crit}$. The panels represent different combinations of available energy (Q), air temperature (T_a), aerodynamic resistance (r_H), and evaporative fraction (f_E). The colored lines represent the conditions where $T_L = T_{crit}$, and the color gradient represents the difference between T_L and T_a. Values to the left of the curves indicate that $T_L < T_{crit}$ and values to the right of the curves indicate that $T_L > T_{crit}$. The sensitivity curves were calculated using Equation 3.1. The value of T_{crit} was set to 45 °C.

four of the five sites, the median observations tended to converge around r_H values of 25 sm^{-1} and f_E values of 0.5. The riparian woodland had lower values of r_H and generally exhibited lower values of f_E, suggesting that vegetation at the site has adapted to have smaller leaves (and thus lower values of r_H) in order to prevent leaf thermal damage when there are low values of f_E under arid conditions. Further evidence for this conclusion is provided by comparing the critical f_E curve for the riparian woodland to the observed distributions of r_H and f_E values for the other sites. For Willow Creek and Morgan Monroe State Forest, the observed values of r_H and f_E are below the critical f_E curve for the riparian woodland, suggesting that the plant traits observed at those two sites are not viable in the environmental conditions of the riparian woodland because they would result in situations where $T_L > T_{crit}$ (Figure 3.6a). Thus, the leaf traits observed at each site appear to be adapted to local environmental conditions and are not necessarily viable in other forest biomes.

To further test this conclusion, we compared the critical f_E curves from the five sites to modeled r_H and f_E values for 6,499 measurements of tree leaves compiled by Wright et al. (2017). Both the f_E curves and the leaf measurements were assumed to be representative of global forest biomes. The r_H and f_E values associated with the leaf measurements exhibited clear evidence of trait coordination between leaf size and stomatal conductance; the edges of the observed r_H and f_E distributions closely mirrored the modeled f_E curves (Figure 3.6b). At low values of r_H, the leaf measurements exhibited a wide range of f_E values. At greater values of r_H, the range of observed f_E values became progressively smaller, and the values of f_E were greater. The largest values of r_H correspond with the largest values of f_E, consistent with model predictions. These data provide high confidence in the conclusion that the observed trait coordination between leaf size and stomatal conductance holds true across global forest biomes.
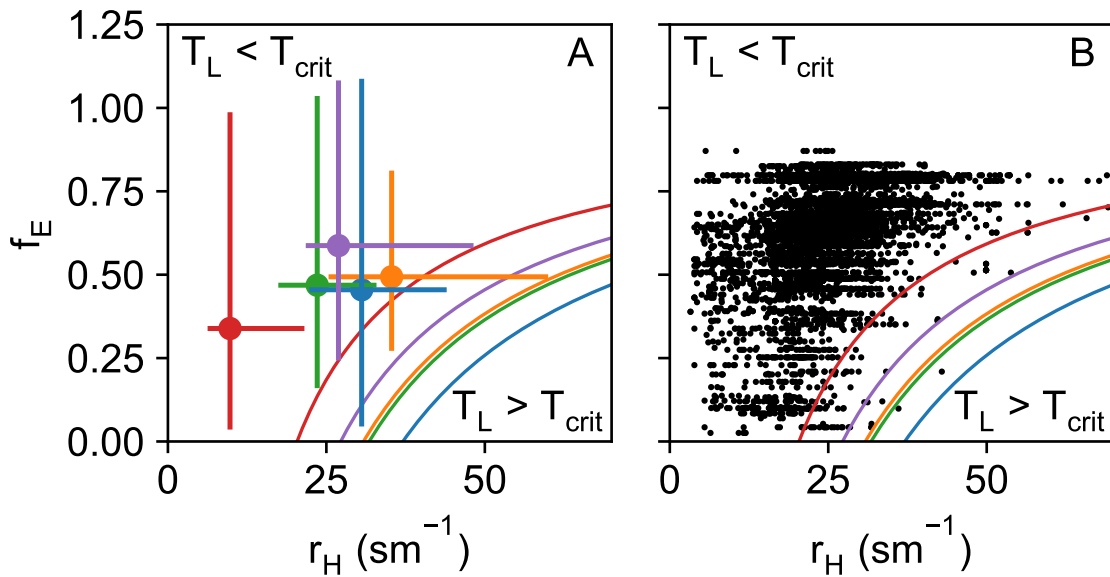
Figure 3.6: In panel (a), the horizontal and vertical bars show the range of observed values (95% percentile interval) for aerodynamic resistance (r_H) and evaporative fraction (f_E) in the boreal aspen forest (green), Willow Creek (blue), Morgan Monroe State Forest (orange), riparian woodland (red), and tropical rainforest (purple). The circles indicate the median observed values. The colored T_{crit} curves show the combinations of r_H and f_E values that result in $T_L = T_{crit}$ at each site. Values to the left of the curves indicate that $T_L < T_{crit}$ and values to the right of the curves indicate that $T_L > T_{crit}$. The curves were calculated using the mean values from stressful conditions where $T_a \geq 30$ °C. Panel (b) shows r_H and f_E values for 6,499 measurements of tree leaves that were compiled by Wright et al. (2017). Observations where $f_E < 0$ and $f_E > 1$ are not plotted. The T_{crit} curves from panel (a) are reproduced in panel (b) for comparison.

3.4   Discussion

We have presented a novel framework to model within-canopy environmental conditions based on known physical principles. The framework was used to predict the vertical profiles of leaf temperature and photosynthesis within forest canopies. We also examined whether leaf traits are coordinated to prevent damaging leaf temperatures that would inhibit photosynthetic function. The sensitivity analysis presented in Figure 3.3 reveals that trait coordination is most important at the top of the canopy, where leaves experience the most stressful temperatures. Within the canopy, there are likely more feasible trait combinations that avoid leaf thermal damage.

The environmental variables were modeled as a function of cumulative leaf area index (i.e., the number of layers of leaves above the measurement height), which provides a generalizable method of modeling within-canopy environmental conditions across different forest types. Different tree species have different vertical distributions of leaf area, and the method presented here is somewhat agnostic to the unique canopy shapes that emerge across different forest biomes (e.g., Béland and Kobayashi, 2021). Given that leaves and their supporting branches are what attenuate energy and wind fluxes downward through the canopy, cumulative leaf area index is a first-order control on canopy environmental variability. The modeled presented here could theoretically be used to retrieve environmental conditions at specific heights within the canopy if the vertical distribution of leaf area is known. It could also be used in combination with light detection and ranging (LiDAR) sensors to create three-dimensional maps of canopy microclimates over large areas.

3.4.1 Canopy microclimate

The modeled vertical profiles of Q, u, and r_H at the five study sites suggest that the environmental conditions in forest understories are often highly decoupled from environmental conditions at the top of the canopy. At four of the five sites, the bottom-of-canopy Q value was 3-7% of the top-of-canopy value, and the bottom-of-canopy u value was 5-11% of the top-of-canopy value. Somewhat surprisingly, vertical profiles of T_a are relatively constant through forest canopies (De Frenne et al., 2021; Vinod et al., 2023). They vary far less than canopy temperature (e.g., Kibler et al., 2023), suggesting that irradiance, and not T_a, is the primary driver of spatial variability in surface temperature within forest canopies.

Surface temperature is affected by irradiance across the full spectrum of electromagnetic radiation, but the distribution of radiation within forest canopies is not uniform across wavelengths. Photosynthetically-active radiation (*ca.* 400-700 nm) is absorbed by chlorophyll within leaves to drive photosynthesis, so it is attenuated downward through the canopy as a function of leaf area (e.g., Bolstad and Gower, 1990). Near-infrared radiation (*ca.* 770-930 nm) is forward-scattered by leaves downward through the canopy, so there are often secondary maxima of near-infrared irradiance in the middles of tree canopies (Roberts et al., 2004). Longwave thermal irradiance (*ca.* 8-14 µm) is emitted by the atmosphere and by leaves and branches themselves, so thermal irradiance can also have maxima within forest canopies (Baldocchi et al., 1984). These trends are demonstrated in data collected by Roberts et al. (unpublished data), who measured the proportion of diffuse to direct radiation at different heights and wavelengths in a plantation of *Populus trichocarpa* × *deltoides* hybrids (Figure 3.7). The visible wavelengths exhibited clear evidence of downward attenuation through the canopy, such that lower heights within the canopy had a smaller diffuse fraction. The near-infrared wavelengths
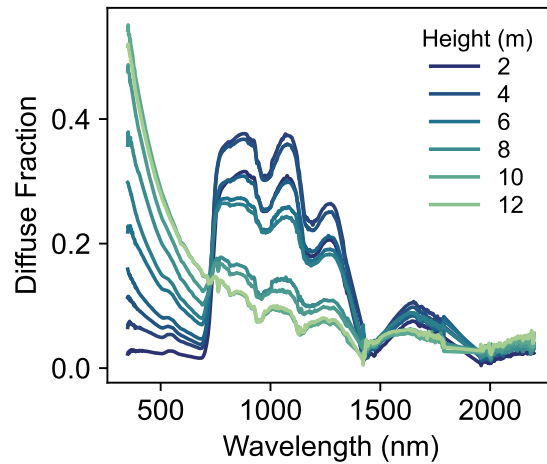
Figure 3.7: Spectral measurements collected at different heights within a plantation of *Populus trichocarpa × deltoides* hybrids by Roberts et al. (unpublished data). The values indicate the fraction of diffuse radiation (i.e., diffuse/(diffuse + direct). The colored lines indicate different measurement heights above the ground.

exhibited evidence of forward scattering, such that the largest fraction of diffuse near-infrared radiation occurred near the bottom of the canopy. Thermal wavelengths were not measured.

Despite the wavelength dependence of radiation attenuation within canopies, shorter wavelengths contain far more energy than longer wavelengths, so photosynthetically-active radiation represents the largest forcing on leaf energy balance. We modeled the attenuation of Q using an extinction coefficient for all-wave net radiation that was derived from measurements of a temperate broadleaf deciduous forest (Baldocchi et al., 1984). To date, there is a paucity of all-wave net radiation extinction measurements, and further research is needed to constrain the extinction dynamics of radiation across the entire electromagnetic spectrum.

The modeled values of u also demonstrated substantial attenuation within forest canopies, which resulted in an exponential increase in r_H towards the bottoms of canopies. At four of the five study sites, the modeled value of r_H more than tripled between the

top and the bottom of the canopy. The r_H value represents the ability of a surface or an organism to shed heat through convection, so it plays a critical role in maintaining surface energy balance within tolerable limits. High values of r_H prevent surfaces from shedding heat, which results in higher modeled surface temperatures. Thus, our model suggests that Q and r_H represent counteracting drivers on T_L within forest canopies. As Q decreases downward through the canopy (a negative forcing on T_L), the value of r_H increases (a positive forcing on T_L). At all five study sites, the modeled T_L at the bottom of the canopy was cooler than the modeled T_L at the top of the canopy, which suggests that Q ultimately represents a more important forcing on T_L within the ranges of observed values.

3.4.2 Leaf temperature

The vertical profiles of T_L exhibited several consistent trends across the study sites: the value of T_L decreased exponentially downward through the canopy at all times of day, the largest vertical gradients of T_L typically occurred in the middle of the day (12:00-14:00), the smallest values of T_L typically occurred early in the day (8:00), and the smallest vertical gradients in T_L typically occurred at the end of the day (16:00). Empirical measurements of T_L in a wet tropical forest by Miller et al. (2021) exhibited those same four features, which provides additional confidence in the model predictions presented here (Figure 3.4). Further research is needed to collect vertically-resolved energy flux measurements and T_L measurements at the same site, which would enable a rigorous validation of the T_L predictions. While T_a, u, and P are often measured along vertical profiles within canopies, few studies have measured vertical profiles of Q (Baldocchi et al., 1984; Chen et al., 1997). As discussed above, Q is likely one of the most important drivers of vertical variability in T_L. Further theoretical and empirical

95

research is also needed to constrain vertical profiles of λE, which is typically measured at a stand scale using eddy covariance sensors. We made the simplifying assumption that f_E was constant throughout the canopy, such that λE was attenuated proportionally to Q. Based on this parameterization, the modeled value of λE was highest at the top of the canopy and lowest at the bottom of the canopy.

The vertical profiles of T_L can also be used to improve the interpretation of temperature measurements from remote sensing platforms and *in situ* radiometers. Thermal sensors almost always measure the outsides of tree canopies, so their measurements may not be representative of the canopy as a whole. Our findings indicate that top-of-canopy measurements may be as much as 7 °C hotter than some leaves inside of the canopy, which could lead to biased predictions of plant physiological function. The model presented here can be used to assign confidence intervals to remote sensing canopy temperature measurements and improve models of plant physiological function that rely on top-of-canopy values.

3.4.3 Photosynthesis

Vertically-resolved estimates of T_L enabled us to model the spatial and temporal distribution of net photosynthesis (A_n) within forest canopies. Unexpectedly, at three of the five sites, the highest levels of midday A_n did not occur at the top of the canopy and actually occurred in the middle or at the bottom of the canopy. The unexpected increase in A_n at lower levels of the canopy can be explained by the temperature and light limitations on photosynthesis. The A_n term was modeled as the minimum of photosynthesis limited by Rubisco activity (A_c) and RuBP regeneration (A_j). Rubisco-limited photosynthesis is regulated by T_L (Figure 3.8b), while RuBP-limited photosynthesis is regulated by both T_L and P (Figure 3.8a). Near the top of the canopy, P does not

limit photosynthesis, so A_n varies solely as a function of T_L. The sensitivity of A_n to T_L resembles a bell curve as peaks at an optimum temperature (T_{opt}). When T_L at the top of the canopy is hotter than T_{opt}, the reduction in T_L within the canopy actually enhances photosynthesis because within-canopy T_L is closer to T_{opt} (Figure 3.8b). When T_L at the top of the canopy is cooler than T_{opt}, the reduction in T_L within the canopy decreases photosynthesis because within-canopy T_L is farther from T_{opt}. At large enough values of $L_{z \to h}$, the P term becomes the limiting factor on photosynthesis (i.e., there is a transition to RuBP-limited photosynthesis) and A_n decreases monotonically as $L_{z \to h}$ increases, regardless of the value of T_L (Figure 3.8c). Thus, the model reveals that when top-of-canopy T_L is greater than T_{opt}, A_n increases downward through the canopy until the point when P becomes limiting. Under these conditions, the maximum A_n occurs at the trade-off point between Rubisco-limited and RuBP-limited photosynthesis. When top-of-canopy T_L is less than T_{opt}, A_n decreases gradually until P becomes limiting, at which point A_n decreases more rapidly.

The A_n term was modeled per unit leaf area, so whole-plant net productivity further depends on the vertical distribution of leaf area within the canopy. Some canopy shapes necessarily have more sunlit leaves than shaded leaves (e.g., Tian et al., 2021), so some forests may experience more total productivity at the top of the canopy, even though the highest density of productivity (i.e., A_n per unit leaf area) occurs in the middle of the canopy. Whole-plant A_n also depends on stem and root respiration, which is not accounted for here. Stems and roots incur respiratory carbon costs but generally do not photosynthesize, so accounting for stem and root respiration would reduce predictions of whole-plant net carbon uptake and may alter estimates of optimal leaf and canopy traits. Interestingly, at four of the five sites, leaf A_n approached zero at the bottom of the canopy, which suggests that the leaf area index of a canopy may be determined by the point at which an additional layer of leaves would incur a net carbon cost (i.e., $A_n < 0$).
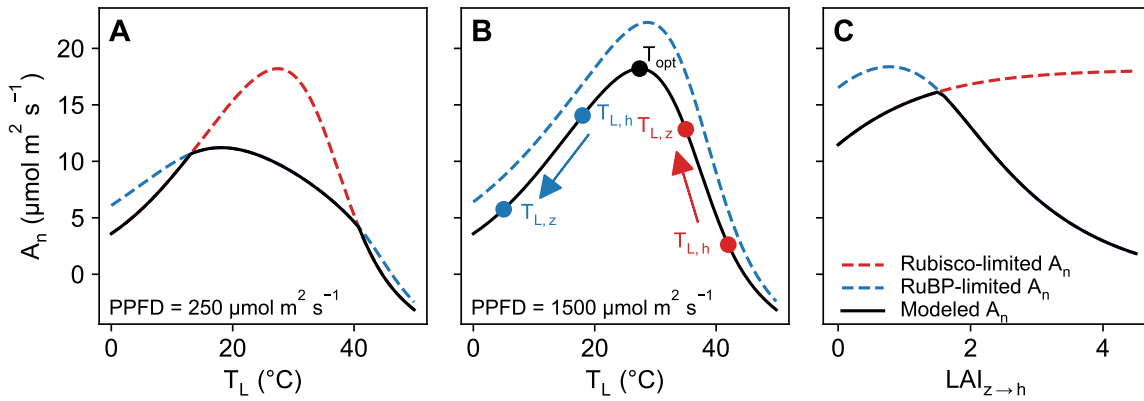
Figure 3.8: Panels (a) and (b) show Rubisco-limited A_n (dashed red line) and RuBP-limited A_n (dashed blue line) under low-light (a) and high-light (b) conditions. The modeled A_n (solid black line) is the minimum value of the two curves. When top-of-canopy leaf temperature ($T_{L,h}$) exceeds the optimum temperature for net photosynthesis (T_{opt}), the within canopy-leaf temperature ($T_{L,z}$) is closer to T_{opt} than $T_{L,h}$ (red dots). When $T_{L,h} < T_{opt}$, $T_{L,h}$ is closer to T_{opt} than $T_{L,z}$ (blue dots). Panel (c) shows the modeled A_n for mean midday conditions at Morgan Monroe State Forest as a function of cumulative leaf area index ($LAI_{z\rightarrow h}$). The modeled A_n initially increases as a function of $LAI_{z\rightarrow h}$ because $T_{L,h} > T_{opt}$.

3.4.4 Leaf trait coordination

The model perturbation analysis revealed that leaf traits play an important role in regulating the vertical profile of T_L. The magnitude of the vertical gradient in T_L was negatively correlated with f_E and positively correlated with d (Figure 3.3). For all three variables, the largest variability in T_L occurred at the top of the canopy, which suggests that top-of-canopy leaves are most vulnerable to thermal stress and damage under changing environmental conditions.

Plants can regulate both f_E and d to avoid leaf thermal damage. Plants actively regulate stomatal conductance, which drives f_E, on time scales of minutes to hours (Drake et al., 2013). Leaf size, which is related to d, also exhibits pronounced intra- and inter-specific variability organized across climate gradients, which likely emerges on inter-annual to evolutionary time scales (e.g., Ackerly et al., 2002; Zwieniecki et al., 2004;

Ramirez-Valiente et al., 2010). The sensitivity analysis presented in Figure 3.5 revealed that trait coordination between f_E and r_H is often necessary to keep leaves below damaging temperatures, and two different data sets provided evidence of trait coordination between f_E and r_H across global forest biomes. (Recall that $r_H = f(d, u)$.) The findings presented here provide a mechanistic framework to examine adaptive plasticity that facilitates leaf thermoregulation and enables plants to respond to heat and water stress under changing environmental conditions. Our findings suggest that arid sites with low values of f_E will likely adapt smaller leaves, and that larger leaves are only feasible in mesic environments that consistently have high values of f_E. Likewise, understory environments will support larger leaves because there is less radiative forcing, which reduces the critical value of f_E at a given value of r_H. Indeed, both trends have been observed in empirical measurements of leaf traits (e.g., Klich, 2000; Zwieniecki et al., 2004; Wright et al., 2017).

3.4.5 Forest responses to climate change

The model predictions and sensitivity analyses also provide insights into how forests will respond to anthropogenic climate change. Many forest ecosystems will experience increased radiative forcing, increased air temperatures, and decreased water availability under anthropogenic climate change (Stephens and L'Ecuyer, 2015; Williams et al., 2020). Our findings suggest that all three shifts in environmental forcings will increase leaf temperature under anthropogenic climate change, especially at the tops of canopies where leaves experience the most stress (Figure 3.3). Changes in leaf temperature will in turn decrease the net photosynthesis of forest canopies because photosynthesis in generally regulated by leaf temperature at the top of the canopy (Figure 3.8). Any reductions in leaf area index that occur under climate change would also diminish canopy microclimates

and subject a larger portion of the canopy to environmental stress. Plants can potentially mitigate the increased stress by adapting leaf traits that help maintain favorable leaf temperatures (Figure 3.5). However, the rate of environmental change may exceed plants' adaptive capacity in some regions. It is also worth noting that changes in plant water use as a result of CO_2 fertilization will also affect how plant productivity responds to anthropogenic climate change.

3.5 Conclusion

In this study, we developed a novel modeling framework to predict the vertical variation of environmental conditions within forest canopies based on known physical principles. The model was forced with top-of-canopy measurements from five flux towers spanning global forest biomes. The model predictions revealed that environmental conditions in forest understories are substantially decoupled from the environmental conditions at the top of the canopy. The modeled vertical profiles of the environmental variables were then used to predict the vertical profiles of leaf temperature and net photosynthetic assimilation. All five sites exhibited exponential decreases in leaf temperature downward through the forest canopy, with the largest vertical gradients occurring in the middle of the day and the smallest vertical gradients occurring in the late afternoon. Unexpectedly, the highest levels of net photosynthesis occurred in the middle or the bottom of the canopy at three of the five sites. An examination of the mechanistic drivers of photosynthesis revealed that this occurred because the top-of-canopy leaf temperature exceeded the optimum temperature for photosynthesis, so the reduced irradiance within the canopy resulted in cooler leaves and more productivity. We also examined whether leaf trait coordination enabled leaves to avoid critical temperatures that cause permanent damage to photosynthetic infrastructure. The findings demonstrated clear evidence

of trait coordination between leaf size and stomatal conductance in both the flux tower data set and a separate data set of leaf measurements spanning global forest biomes. Collectively, our findings suggest that vertical variation in environmental conditions within forest canopies has a substantial impact on plant physiological function, and that canopy microclimates likely play and important role in enhancing forest productivity and resilience under anthropogenic climate change. Our findings also provide insights into how forest productivity will respond to anthropogenic climate change, and the types of adaptations that will help plants maintain high levels of physiological function under shifting environmental conditions.

Conclusion

The goal of this research was to identify how changes in root zone water availability affect the evapotranspiration and photosynthesis of dryland vegetation, and to quantify how water subsidies from shallow groundwater aquifers alter plant physiological function. Dryland ecosystems represent the largest source of inter-annual variability in the global land carbon cycle (Poulter et al., 2014), and the productivity of dryland ecosystems is primarily limited by water availability, so constraining the sensitivity of dryland plant function to changes in root zone soil moisture is of critical importance for improving global land surface models. Groundwater-dependent ecosystems serve as an ideal natural experiment in dryland plant function because they benefit from a consistent source of water in otherwise water-limited environments. By analyzing temporal trends of groundwater availability, and by comparing vegetation stands with and without access to groundwater, I was able to quantify the impact of subsurface water subsidies on vegetation cover, evapotranspiration, and photosynthesis. I primarily analyzed plant physiological function through the lens of leaf temperature, which is sensitive to air temperature, radiation, and plant water use. Leaf temperature directly regulates the rates of photosynthesis and respiration, so it is a useful proxy for other aspects of plant physiological function that are more difficult to measure and model.

In Chapter 1, I synthesized remote sensing data with measurements from groundwater monitoring wells to quantify the sensitivity of riparian woodland vegetation cover

to changes in groundwater depth during an extreme drought. Both healthy vegetation cover and dead/woody vegetation cover exhibited a strong sensitivity to groundwater depth. The fraction of healthy vegetation cover was negatively correlated with groundwater depth, and the fraction of dead/woody vegetation cover was positively correlated with groundwater depth. The land cover fractions exhibited pronounced changes when the depth to groundwater exceeded *ca.* 5 m, which is approximately equal to the rooting depths of riparian tree species. The findings suggest that changes in riparian woodland vegetation cover were driven by riparian trees losing access to root zone water subsidies from shallow groundwater. We also observed a coherent spatial and temporal trend of riparian woodland mortality over six years, which mirrored similar trends in groundwater depth. The "brown wave" of tree mortality was likely an emergent property of individual trees responding to local changes in groundwater depth across the entire subbasin. Collectively, the findings suggest that riparian tree species depend on water subsidies from shallow groundwater to maintain high levels of physiological function, and that losing access to shallow groundwater will cause substantial stress or mortality. Our findings also represent one of the most robust estimates to date of the minimum groundwater depth needed to maintain the health and function of dryland riparian woodlands.

In Chapter 2, I developed a novel theoretical model to predict leaf temperature as a function of surface energy fluxes and environmental conditions. I demonstrated that the difference between leaf temperature and air temperature varies as a linear function of the evaporative fraction, which is a novel linearization that reduces the number of surface parameters needed to estimate leaf temperature. The model was validated using data from two flux towers that measure stands of *Prosopis velutina*, one of which has access to groundwater and one of which does not. The model exhibited strong predictive power at both sites ($R^2 = 0.8$ and $R^2 = 0.63$, respectively) when the predictions were compared to measurements of leaf temperature from infrared radiometers mounted on

the flux towers. The model predictions and empirical observations also revealed that leaf temperature converges to air temperature when the evaporative fraction equals one. When the evaporative fraction is less than one, leaf temperature is higher than air temperature. The evaporative fraction data also provided insights into plant water sources at the two sites. In the riparian woodland with groundwater access, the evaporative fraction was not strongly correlated with shallow soil moisture. In the upland savanna without groundwater access, the evaporative fraction was strongly correlated with shallow soil moisture. The findings suggest that the riparian woodland primarily consumed deeper water from groundwater aquifers, while the upland savanna primarily consumed shallow soil moisture derived from local precipitation. The leaf temperature model was also used to perform counterfactual simulations to predict the leaf temperature if the evaporative fraction was reduced to zero. We also predicted changes in leaf respiration, which is a critical component of the carbon cycle and can be empirically modeled as a function of leaf temperature. The simulations revealed that evaporative cooling reduced leaf temperature by *ca.* 1-5 °C and leaf respiration by *ca.* 15% in the middle of the growing season. The findings demonstrated a novel connection between plant water and carbon cycles via leaf energy balance that has received little attention in literature.

In Chapter 3, I developed a novel modeling framework to predict within-canopy environmental conditions based on top-of-canopy measurements. The model was then used to predict the vertical profiles of leaf temperature and photosynthesis within forest canopies at five flux tower sites spanning global forest biomes. The model predictions, which were based on known physical principles, indicated that leaf temperature decreased exponentially downward through the forest canopies. The tops of the forest canopies exhibited the most variability in leaf temperature. The highest leaf temperatures and the largest vertical gradients in leaf temperature occurred in the middle of the day. The lowest leaf temperatures occurred early in the morning, and the smallest vertical gradients in

leaf temperature occurred late in the afternoon. The leaf temperature predictions were compared to empirical measurements of leaf temperature by Miller et al. (2021) in a wet tropical forest. The empirical measurements exhibited the same key trends as the model predictions, which provides additional confidence that the model has predictive value. We also performed a sensitivity analysis on the leaf temperature model to identify the combinations of environmental conditions that result in damaging leaf temperatures (*ca.* 45 °C). The sensitivity analysis revealed that there is a functional trade-off between aerodynamic resistance, which is related to leaf size, and the evaporative fraction, which is related to stomatal conductance, such that larger leaves typically need to maintain higher evaporative fractions to prevent leaf thermal damage. We compared the critical leaf temperature curves to the flux tower measurements and to a separate global database of leaf measurements, both of which demonstrated clear evidence of trait coordination between leaf size and stomatal conductance to avoid leaf thermal damage across global forest biomes.

Mechanistic models of ecosystem function substantially improve our ability to interpret measurements from remote sensing platforms and flux tower sensors. They also make it possible to reliably interpolate observations where sensor measurements are not available, and they provide a framework to predict how ecosystems will respond to future climate forcings. Many mechanistic models can also be differentiated, which makes it possible to quantify the sensitivity of ecosystem processes to traits that are difficult to measure. Much of the work presented here leverages a novel data-model fusion approach to quantify critical thresholds for plant physiological function that rarely occur in reality. For example, we were able to estimate the changes in leaf temperature and respiration that would occur if stomatal conductance was reduced to zero. We also identified the combinations of leaf size and stomatal conductance that result in damaging leaf temperatures. Applied in this way, the data-model fusion approach will likely be

useful for predicting critical tipping points in ecosystem function under anthropogenic climate change. We also use the data-model fusion approach to estimate environmental conditions along vertical profiles within tree canopies. Canopy microclimates will likely play a critical role in enhancing forest resilience under anthropogenic climate change, but remote sensing platforms and meteorological sensors typically measure the outsides of tree canopies, and there have been relatively few systematic analyses of within-canopy environmental variability (De Frenne et al., 2021; Vinod et al., 2023). By combining top-of-canopy measurements with a model based on known physical principles, we were able to develop spatially explicit estimates of leaf temperature and photosynthesis within forest canopies, and we were able to predict how canopy microclimates will respond to changing environmental conditions. These findings can serve as the basis for future research that examines how canopy microclimates alter plant physiological function and how canopy microclimates serve as refugia for plant and animal biodiversity.

The research presented here also provides new insights into the functional ecology of dryland riparian woodlands, which are productivity and biodiversity hotspots on dryland landscapes, but are also extremely sensitive to hydroclimatic change. Many riparian woodlands in the southwestern United States grow near rivers whose hydrologic regimes are subject to substantial anthropogenic regulation (Downs et al., 2013; Rohde et al., 2021). Water management decisions often come into conflict with legal obligations to protect endangered species that rely on riparian woodlands (e.g., Kus, 1998), and these situations do not always have clear solutions. Some legal frameworks, such as California's Sustainable Groundwater Management Act, require water managers to protect the basic function of groundwater-dependent ecosystems when making water management decisions (Rohde et al., 2017). However, there is a paucity of scientific research that can be used to inform such evidence-based water management decisions that protect ecosystem function. I have identified the critical minimum groundwater depth that is needed to

sustain the function of dryland riparian woodlands. This research is already being used to inform groundwater management decisions in the Fillmore Basin in Ventura County, California. Likewise, the remote sensing products developed in Chapter 1 are being used in a related research project to monitor changes in habitat quality and population density for several sensitive riparian bird species. By leveraging new techniques in remote sensing, ecological modeling, and field measurements, I have produced novel insights into dryland riparian ecohydrology that are helping protect biodiversity and ecosystem function under anthropogenic climate change.

3.5.1 Future Research

The findings presented here create several new opportunities for future research. The first chapter demonstrated that groundwater declines during extreme drought conditions can cause widespread tree mortality in riparian woodlands. Groundwater declines resulting from extreme droughts are likely ubiquitous across semi-arid and arid regions, although there is relatively little research examining how vegetation health responds to changing groundwater depth across space and time. Future research could examine other study systems that experienced substantial declines in groundwater during drought conditions to determine whether there were coherent spatial and temporal trends of vegetation change, similar to the brown wave of riparian woodland mortality reported here. More advanced remote sensing data could also improve the ability of future studies to resolve changes in ecosystem structure and function. For example, hyperspectral remote sensing imagery could be used to develop maps of individual species within riparian woodlands, and groundwater data could be used to constrain the sensitivity of each species to changes in root zone water availability. Light detection and ranging (LiDAR) data could also be used to characterize the height and structure of individual trees, and groundwater data

107

could be used to determine whether trees with certain structural traits are more vulnerable to groundwater declines. Future research could also examine whether the duration of groundwater declines affects the recovery of vegetation, and whether prolonged groundwater declines are more likely to cause drought-induced vegetation type conversion.

The research in the second chapter could be extended to quantify the magnitude of leaf evaporative cooling that occurs across global forest biomes. It is likely that some regions, such as wet tropical forests, experience more evaporative cooling than the dryland ecosystems examined here. Future research could also examine the impact of evaporative cooling on both photosynthetic assimilation and respiration, which interact to regulate net carbon uptake. The temperature sensitivity of photosynthetic assimilation resembles a bell curve and peaks at an optimal temperature, while the temperature sensitivity of respiration is an increasing exponential function. The work presented here only examined the impact of evaporative cooling on leaf respiration. Modeling both components of the plant carbon cycle simultaneously may lead to novel insights about the connection between plant water and carbon cycles via evaporative cooling. Future research could also extend the modeling framework used in the second chapter to quantify the impacts of radiative cooling on leaf temperature. Radiative cooling is an important mechanism of leaf thermoregulation that has received little attention in literature.

The modeling framework proposed in the third chapter would benefit from more extensive validation at a study site where ecosystem energy fluxes and vertical profiles of leaf temperature are measured simultaneously. To date, there is a paucity of such measurements in the literature. Future work could also constrain the extinction coefficients for all-wave net radiation across different plant functional types. All-wave net radiation is an important driver of leaf temperature, but few studies have examined how it varies along vertical gradients within forest canopies. The modeling framework could also be used to predict how optimal leaf traits vary along vertical gradients within forest canopies.

Empirical analyses have demonstrated that leaf size and shape often differ between the tops and bottoms of canopies (e.g., Zwieniecki et al., 2004). The work presented here could be used to identify the mechanistic basis for such behavior across different forest biomes. The modeling framework could also be parameterized using LiDAR data in order to produce three-dimensional spatially-explicit maps of canopy microclimates. Three-dimensional maps of canopy microclimates would not only be useful for improving predictions of plant physiological function, but they could also lead to novel insights into wildlife ecology and physical climate processes. Such research could result in a more synthetic understanding of the interactions between hydrological processes, plant traits, and ecosystem function across global forest biomes.

Appendix A

Supplementary Information for Chapter 1

A.1   Depth to groundwater

We used two different protocols to calculate DTG at the study sites, depending on the data availability for each site. The first protocol was used for four sites that had a nearby shallow well (< 30 m deep) with a complete time series of measurements from 2011 to 2018. Well depths for the shallow wells ranged from 9.8 m to 28 m. The distance between the riparian woodlands and their representative wells is the primary control on the accuracy of the groundwater data. The distance from the four study sites to their representative wells ranged from 13 m to 1,326 m with a median distance of 332 m (Figures A.1-A.2; Table A.1). We assumed that the shallow well measurements represented groundwater trends in the uppermost aquifer, where groundwater can be accessed by phreatophytes, so we used groundwater elevation data directly from the well measurements. We subtracted the groundwater elevation data from surface elevation data extracted from a U.S. Geological Survey digital elevation model. This enabled us

to calculate the mean DTG for each study site and each year. The second protocol was used for two sites (Fillmore Ciénega and East Grove) that did not have a complete time series of shallow groundwater data. For those sites, we compiled data from nearby shallow wells that had limited measurements during and after the drought (Figures A.3-A.4; Table A.2). We used the data to develop a composite time series of shallow DTG measurements at each site. When multiple shallow wells were measured on the same date, we calculated the mean DTG of all of the shallow well measurements for that date. We then acquired data from nearby wells that had deep or unknown depths but had a complete time series of measurements from 2011 to 2018. For Fillmore Ciénega, we used data from two deep wells located immediately adjacent to each other, so we composited their measurements using the method described above (i.e., the mean reading for each date). For each shallow DTG measurement, we identified the deep DTG measurement that was closest in time to the shallow DTG measurement date. We then developed linear regression models to predict the shallow DTG measurements using the corresponding deep DTG measurements at Fillmore Ciénega ($R^2 = 0.96$, $p < 0.001$, MAE = 0.28 m) and East Grove ($R^2 = 0.69$, $p < 0.001$, MAE = 0.18 m). We then applied the models to the complete time series of DTG measurements from the deeper wells. This produced a temporally interpolated product of shallow DTG for each study site. The strong model fits and the small absolute errors indicate that the resulting data are accurate and precise estimates of the DTG at each study site.
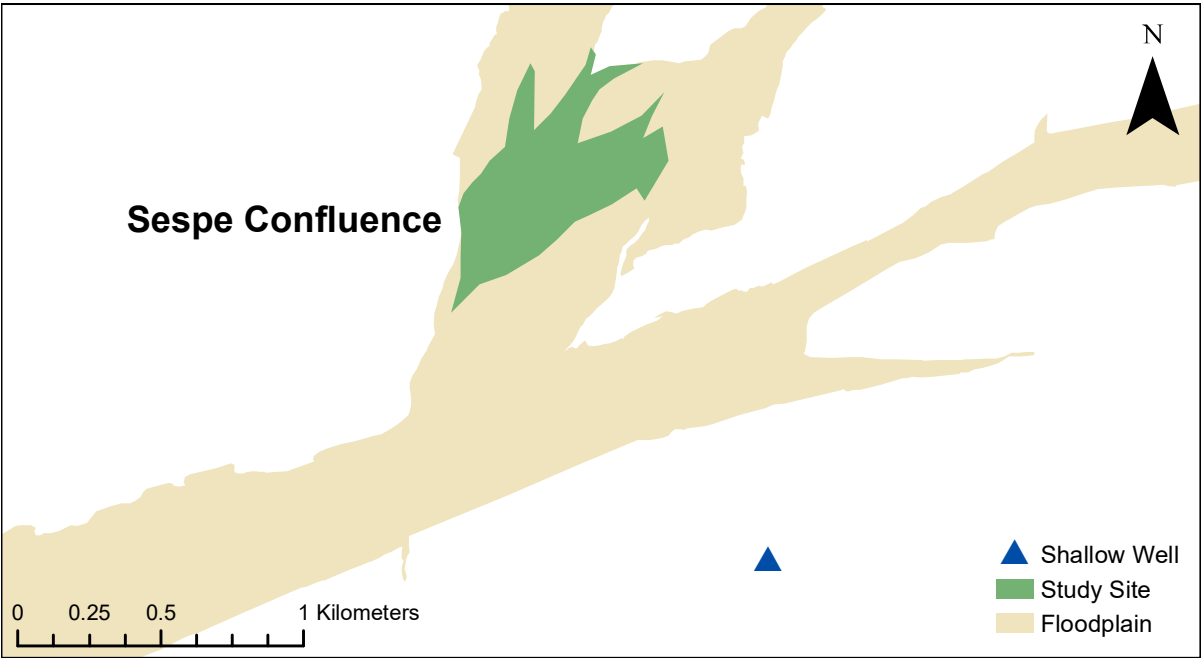
Figure A.1: Location of well used to measure DTG at the Sespe Confluence site.
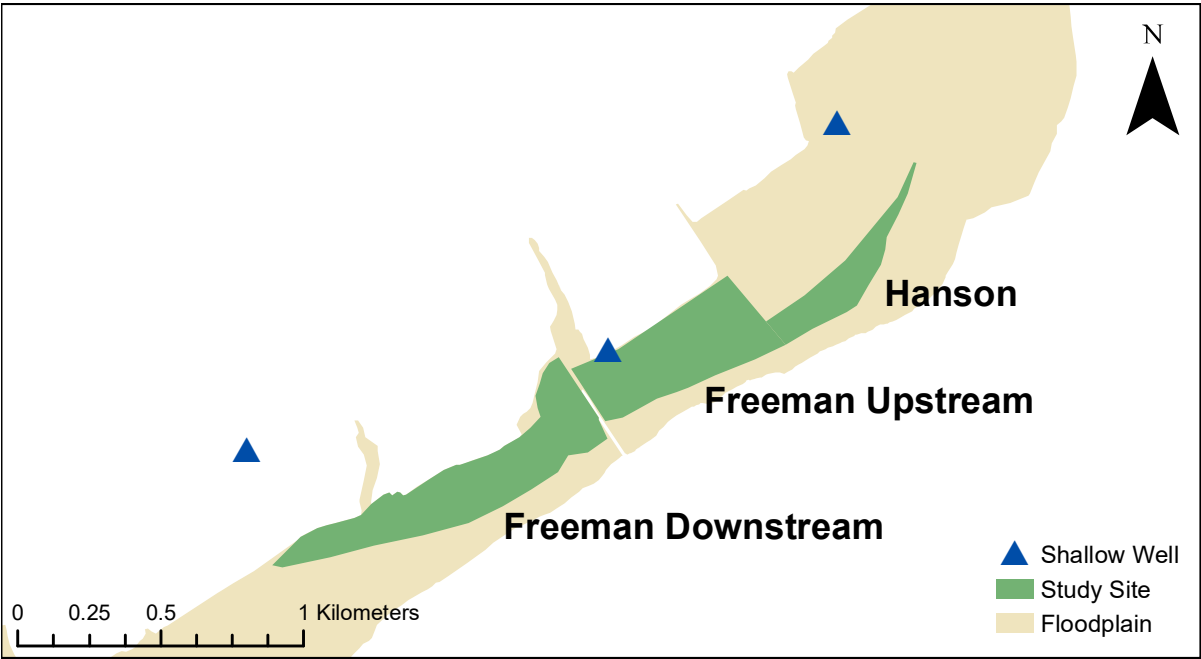

Figure A.2: Location of wells used to measure DTG at the Hanson, Freeman Upstream, and Freeman Downstream sites.
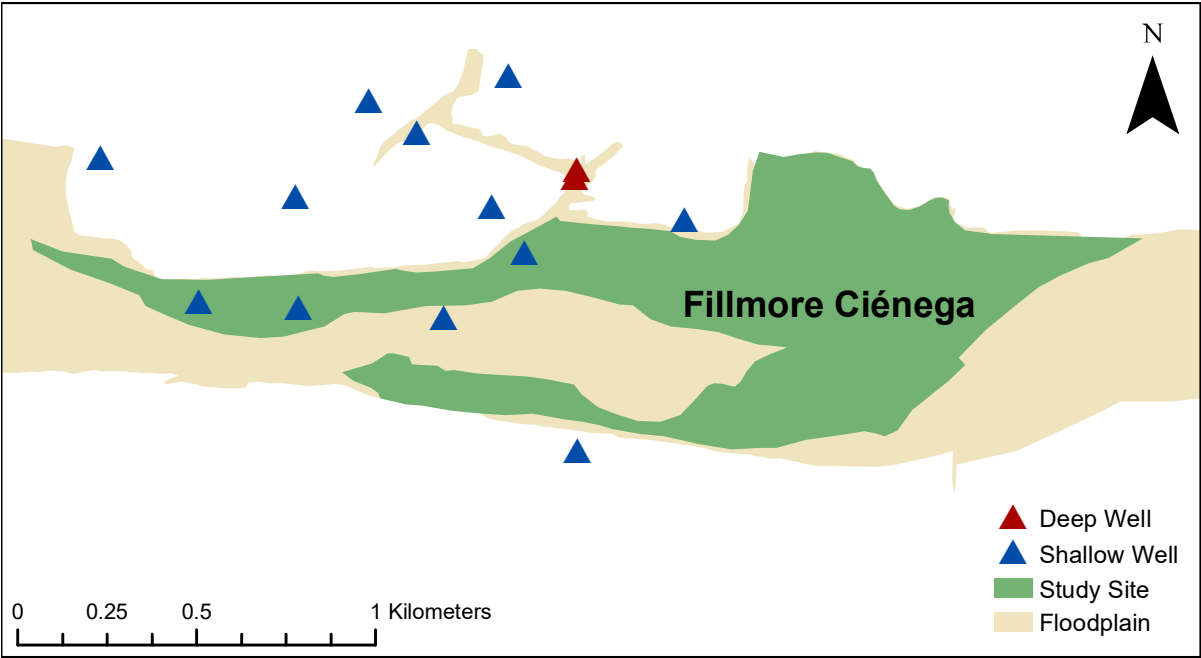
Figure A.3: Location of wells used to measure DTG at the Fillmore Ciénega site.
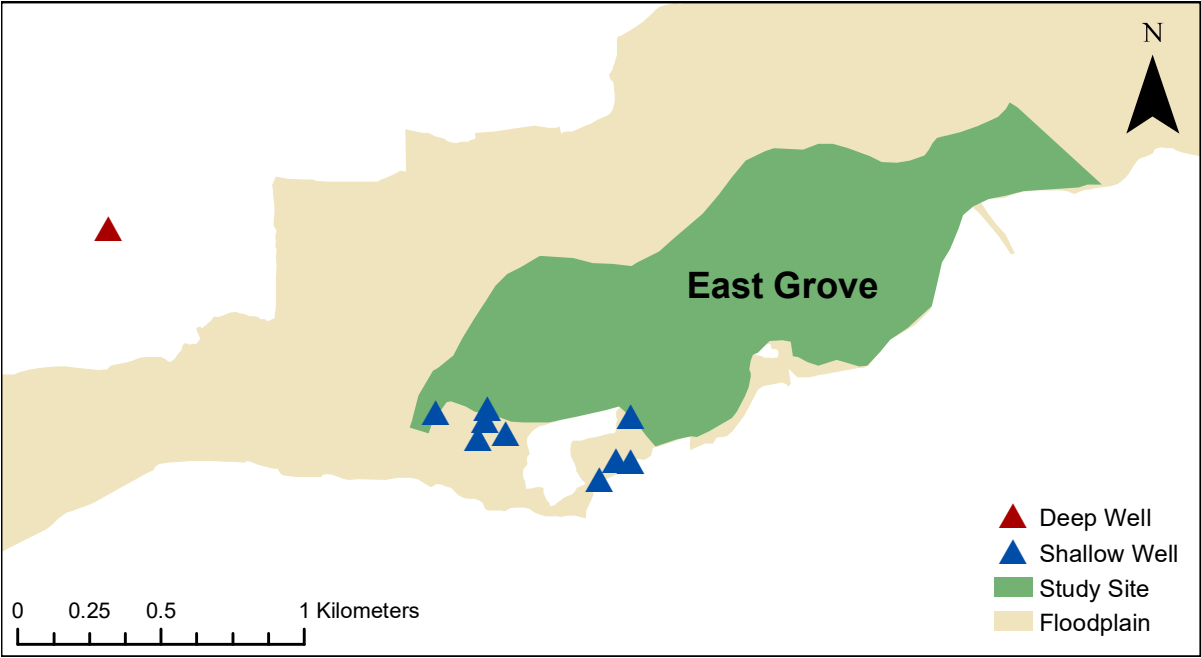
Figure A.4: Location of wells used to measure DTG at the East Grove site.

Table A.1: Wells used to model DTG at sites that required the first modeling protocol.

Site Name	State Well Number	Well Longitude	Well Latitude	Distance to Site (m)	Well Depth (m)	Well Top Perf. (m)	Well Bottom Perf. (m)
Sespe Confluence	03N20W02A001S	-118.941881	34.37595	1325.8	28	unknown	unknown
Hanson	03N21W29K002S	-119.100601	34.309735	303.7	21.3	9.1	18.3
Freeman Upstream	03N21W32C001S	-119.10914	34.302402	13	9.8	3.7	9.8
Freeman Downstream	03N21W31F004S	-119.122791	34.29901	359.5	11.3	5.2	11.3

Table A.2: Wells used to model DTG at sites that required the second modeling protocol.

Site Name	Well Number	Well Longitude	Well Latitude	Distance to Site (m)	Well Depth (m)	Well Type
Fillmore Ciénega	04N19W33D003S	-118.882346	34.391718	144.2	157.9	Deep
Fillmore Ciénega	04N19W33D004S	-118.882407	34.391525	122.3	151.2	Deep
Fillmore Ciénega	04N19W33M05S	-118.882178	34.3846292	81.7	32.6	Shallow
Fillmore Ciénega	UCSB-1	-118.887229	34.392557	385.4	3.07	Shallow
Fillmore Ciénega	UCSB-2	-118.888702	34.393366	478.4	3.10	Shallow
Fillmore Ciénega	UCSB-3	-118.89088	34.390884	215.2	4.80	Shallow
Fillmore Ciénega	UCSB-4	-118.88491	34.390747	111.3	2.78	Shallow
Fillmore Ciénega	UCSB-5	-118.890733	34.388109	0	2.87	Shallow
Fillmore Ciénega	UCSB-6	-118.896821	34.391792	275.6	3.25	Shallow
Fillmore Ciénega	UCSB-7	-118.893772	34.388208	0	<2.39	Shallow
Fillmore Ciénega	UCSB-8	-118.883888	34.389599	0	3.00	Shallow
Fillmore Ciénega	UCSB-9	-118.884486	34.394051	417.1	<3.92	Shallow
Fillmore Ciénega	UCSB-10	-118.879051	34.390502	48.6	3.58	Shallow
Fillmore Ciénega	UCSB-11	-118.886312	34.387917	33.4	<3.92	Shallow
East Grove	03N21W12B002S	-119.029231	34.361255	1227.3	unknown	Deep (?)
East Grove	HRP-1	-119.01403	34.35505	47.0	2.72	Shallow
East Grove	HRP-2	-119.01474	34.35583	0	3.18	Shallow
East Grove	HRP-3	-119.01479	34.35547	20.0	2.90	Shallow
East Grove	HRP-4	-119.01505	34.35488	89.0	3.23	Shallow
East Grove	HRP-5	-119.01668	34.35566	0	2.79	Shallow
East Grove	HRP-6	-119.01041	34.35365	222.9	2.57	Shallow
East Grove	HRP-7	-119.00925	34.35424	99.7	2.62	Shallow
East Grove	HRP-8	-119.0098	34.35427	135.2	2.64	Shallow
East Grove	HRP-9	-119.00929	34.35567	0	2.79	Shallow

A.2 Spectral mixture analysis model calibration

Spectral mixture analysis (SMA) decomposes measured spectra using reference spectra of pure materials known as endmembers. SMA analyzes each measured spectrum as a weighted linear combination of two or more endmembers. SMA determines the combination of endmembers and weights that produces the smallest residual between the modeled and measured spectra (Smith et al., 1990; Roberts et al., 1998). The weight assigned to an endmember in the most parsimonious model is assumed to indicate the fractional cover of that material in a pixel (Roberts et al., 1993).

Endmember spectra can be acquired at the leaf, branch, or canopy scale. Leaf and branch spectra are measured *in situ* using a field spectrometer. Canopy spectra are measured using airborne or satellite sensors (Roberts et al., 2004). Typically, dozens of potential endmember spectra are acquired and the final set of endmembers is determined using an endmember selection algorithm (Dennison and Roberts, 2003). Endmember selection plays a crucial role in ensuring the accuracy of the modeled land cover fractions (Roth et al., 2012). We used a multi-stage endmember selection process to ensure that the endmembers were both pure and representative of the study sites.

GV and NPV endmembers were selected from WestUSA, a reference spectral library that was created *in situ* using a field spectrometer (Roberts et al., 2004). Using *in situ* spectra ensures that the endmembers are not contaminated by other land cover types. Endmembers were selected using constrained reference endmember selection (CRES), which determines the set of endmembers that minimize the residual between modeled and reference land cover fractions (Roberts et al., 1993). Reference land cover fractions were created for forty-nine 18 m by 18 m plots. The locations of the reference plots were selected from hyperspectral imagery acquired over the study area by the Airborne Visible/Infrared Imaging Spectrometer (AVIRIS)(Green et al., 1998). The goal of the

analysis was to select in situ spectra to serve as pure reference data for our study area, so we identified 49 AVIRIS pixels (18 m spatial resolution) that appeared to exhibit pure spectral responses and were representative of the GV (35 pixels) and NPV (14 pixels) classes. The locations of the AVIRIS pixels were then ported to Google Earth, and the reference fractions for each 18 m plot were manually estimated using high-resolution aerial imagery. CRES was performed individually for each reference plot, and the selected WestUSA endmembers were recorded. The two GV endmembers and the two NPV endmembers that were selected most frequently were included in the final spectral library. One additional NPV endmember was extracted directly from the Landsat imagery to model a small stand of NPV that was not successfully modeled by the other endmembers.

The study area contains large areas of barren ground, so soil spectra were extracted from imagery acquired by AVIRIS. AVIRIS was flown over the study area in April 2013, May 2013, September 2013, June 2014, May 2015, and June 2016 as part of the HyspIRI Airborne Campaign (Lee et al., 2015). Using soil spectra acquired over the study area ensures that the endmembers are representative of local soil types. A total of 439 soil spectra, 346 GV spectra, and 340 NPV spectra were extracted from the AVIRIS images, stratified evenly across the image dates. Iterative endmember selection (IES) was used to select soil endmembers from the AVIRIS spectra. IES is an automated endmember selection algorithm that iteratively adds and removes endmembers from the spectral library until the kappa statistic is maximized (Roth et al., 2012; Schaaf et al., 2011). Kappa is an omnibus statistic that considers all classes simultaneously, which is why we also extracted GV and NPV spectra from the AVIRIS imagery. IES selected nine soil endmembers, seven GV endmembers, and seven NPV endmembers. The soil endmembers were included in the final spectral library. The GV and NPV endmembers from AVIRIS were discarded because the WestUSA endmembers produced more stable model outputs across different image dates.

The final spectral library was convolved to the spectral resolutions of the Landsat sensors, and it was used to unmix Landsat images acquired in June between 2011 and 2018. Data from June 2012 was excluded because of the scan line corrector failure on Landsat 7 (Markham et al., 2004). The Landsat images were unmixed using multiple endmember SMA (MESMA), a variant of SMA that imposes several constraints to ensure that the modeled fractions are physically reasonable and accurate (Roberts et al., 1998). Endmember fractions were constrained between 0 and 1 (i.e., 0-100% cover), and the maximum allowable root mean square error between modeled and measured spectra was 0.025. MESMA also adds a photometric shade endmember with zero reflectance to the library before unmixing. The shade endmember helps normalize for illumination variability across the image. The shade fractions were constrained between 0 and 0.8, but the modeled shade fractions were proportionally reallocated to the other land cover classes before further analysis. This is a standard process known as shade normalization (Smith et al., 1990). Land cover fractions derived from MESMA have been validated extensively in a variety of natural and urban ecosystems and were found to be highly accurate. The validations for GV and NPV fractions typically produce R^2 values exceeding 0.8, a slope near 1, and intercepts less than 5% (Smith et al., 1990; Powell et al., 2007; Roberts et al., 2012; Wetherley et al., 2017). Almost all the pixels in the study area were successfully modeled using MESMA, and cloud cover over the study area was minimal. Unmodeled and clouded pixels were removed from the analyses. The final data set indicated GV, NPV, and soil fractions for each pixel in each image. These data were used to monitor changes in land cover throughout the time series.

A.3 Statistical analysis

Mixed-effect logistic-binomial regression was used to model the relationship between DTG and GV fractions and between DTG and NPV fractions. A logistic-binomial model (Gelman and Hill, 2007) was necessary because it is physically impossible to have land cover fractions outside of the 0-1 range. Thus, a robust statistical model of land cover fractions will never predict values outside of the 0-1 range and will naturally saturate at 0 and 1. Site was included as a random effect in the model to account for the effects of climate and other localized drivers of vegetation cover that were not explicitly specified in the model. In order to be compatible with the modeling software, the land cover fractions were recoded as count data that recorded the proportion of the land cover type in each pixel. The count data was scaled from 0 to 1,000. For example, a pixel with a GV fraction of 0.6 was coded as 600 "successes" and 400 "failures". The regression models were then developed using the glmer function in the lme4 package in R (Bates et al., 2015; R Core Team, 2020). The resulting statistical models were highly significant ($p <$ 0.001) and exhibited strong model fit. Pseudo-R^2 values between 0.2 and 0.4 indicate "excellent fit" (McFadden, 1977).

A.4 Results

Table A.3: Change in maximum DTG in meters compared to the maximum DTG from the previous calendar year. A negative value indicates a water table decline.

Site Name	2012	2013	2014	2015	2016	2017	2018	2019	2012-2016 Mean	2012-2016 Min.
Fillmore Ciénega	-0.25	-2.41	-2.38	-3.05	-3.86	3.05	6.02	0.18	-2.39	-3.86
Sespe Confluence	-0.83	-2.61	-3.35	-2.47	-3.45	1.51	2.83	0.34	-2.54	-3.45
East Grove	-0.08	-0.15	-0.27	-0.19	-0.23	0.41	0.04	0.04	-0.18	-0.27
Hanson	-0.67	-0.57	-0.94	-0.34	-1.0	1.09	-0.23	0.12	-0.7	-1.0
Freeman Upstream	-0.71	-0.41	-0.69	-0.62	-0.61	1.73	-0.79	-0.06	-0.61	-0.71
Freeman Downstream	-0.87	-0.99	-1.24	-1.41	-0.5	0.36	-0.52	1.93	-1.0	-1.41

Table A.4: Median green vegetation fractions for each study site and each year.

Site Name	2011	2013	2014	2015	2016	2017	2018
Fillmore Ciénega	0.585	0.609	0.271	0.1	0.096	0.141	0.125
Sespe Confluence	0.574	0.552	0.357	0.142	0.152	0.223	0.238
East Grove	0.691	0.705	0.669	0.65	0.618	0.615	0.629
Hanson	0.727	0.671	0.708	0.647	0.602	0.623	0.646
Freeman Upstream	0.613	0.514	0.458	0.351	0.397	0.486	0.374
Freeman Downstream	0.512	0.513	0.511	0.442	0.472	0.48	0.474

Table A.5: Median non-photosynthetic vegetation fractions for each study site and each year.

Site Name	2011	2013	2014	2015	2016	2017	2018
Fillmore Ciénega	0	0.301	0.57	0.68	0.66	0.504	0.542
Sespe Confluence	0	0.378	0.53	0.643	0.645	0.526	0.476
East Grove	0.255	0.287	0.324	0.345	0.379	0.372	0.359
Hanson	0	0.329	0.284	0.353	0.356	0.364	0.342
Freeman Upstream	0	0.418	0.472	0.606	0.551	0.443	0.56
Freeman Downstream	0	0.356	0.306	0.406	0.4	0.32	0.35

Table A.6: Compact letter display indicating significant differences in median land cover fractions by year for each study site. Like letters indicate that values do not differ significantly by Kruskal-Wallis using a post-hoc Dunn's test with a Holm adjustment ($\alpha = 0.05$). Each row was analyzed separately, and letters should not be compared across rows.

Site	Type	2011	2013	2014	2015	2016	2017	2018
Fillmore Ciénega	GV	a	a	b	c	c	d	d
Fillmore Ciénega	NPV	a	b	c	d	d	e	f
Sespe Confluence	GV	a	a	b	c	c	d	d
Sespe Confluence	NPV	a	b	c	d	d	c	c
East Grove	GV	a	b	c	d	e	e	e
East Grove	NPV	a	b	c	d	e	e	f
Hanson	GV	a	bc	ab	cd	d	d	cd
Hanson	NPV	a	bc	b	c	c	c	bc
Freeman Upstream	GV	a	b	b	c	c	b	c
Freeman Upstream	NPV	a	b	b	c	c	b	c
Freeman Downstream	GV	a	a	a	b	ab	ab	ab
Freeman Downstream	NPV	a	bc	b	c	c	b	b

Figure A.5: Dead riparian vegetation at the Fillmore Ciénega site. Photograph taken in March 2017. Photo credit: Michael Singer.

Figure A.6: Dead and surviving trees at the location where the brown wave ended. The brown wave caused widespread mortality of native phreatophytes (foreground) but stopped just upstream of the East Grove site (background). Photograph taken in April 2017 near the northeast edge of the East Grove site, looking south. Photo credit: Adam Lambert.
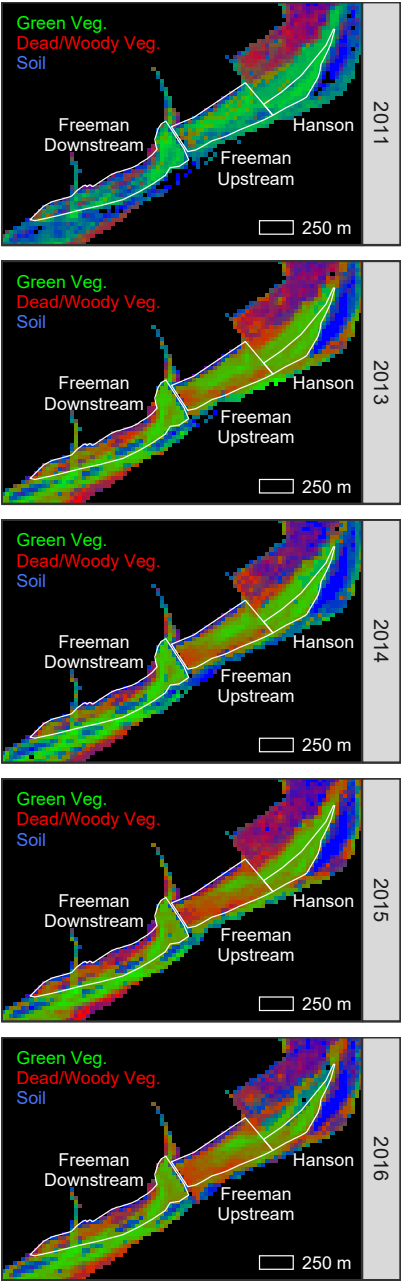
Figure A.7: Remote sensing model outputs of floodplain land cover in the Santa Paula subbasin from 2011 to 2016. The study sites are outlined in white. The river flows from right to left.

Figure A.8: Riparian vegetation at the Sespe Confluence site. The invasive reed *Arundo donax* (foreground) spread across the site after the widespread mortality of native phreatophytes. Photograph taken in April 2021.

Figure A.9: Dense and tall canopy of surviving riparian trees at the Freeman Downstream site. Photograph taken in April 2021.

Appendix B

Supplementary Information for Chapter 2

B.1   Equation 2.6 derivation

$$Q_a - H - \lambda E = 0 \tag{B.1}$$

$$H = k\frac{\rho c_p(T_L - T_a)}{r_H} \tag{B.2}$$

$$Q_a - \lambda E = k\frac{\rho c_p(T_L - T_a)}{r_H} \tag{B.3}$$

$$(Q_a - \lambda E)\frac{r_H}{k\rho c_p} = T_L - T_a \tag{B.4}$$

$$Q_a\left(1 - \frac{\lambda E}{Q_a}\right)\frac{r_H}{k\rho c_p} = T_L - T_a \tag{B.5}$$

$$\left(1 - \frac{\lambda E}{Q_a}\right) \frac{Q_a r_H}{k\rho c_p} = T_L - T_a \tag{B.6}$$

$$\frac{Q_a r_H}{k\rho c_p} - \frac{Q_a r_H}{k\rho c_p} \left(\frac{\lambda E}{Q_a}\right) = T_L - T_a \tag{B.7}$$

$$f_E = \frac{\lambda E}{Q_a} \tag{B.8}$$

$$\frac{Q_a r_H}{k\rho c_p} - \frac{Q_a r_H}{k\rho c_p} f_E = T_L - T_a \tag{B.9}$$

B.2 Comparison of kB^{-1} formulas

The r_H term is the sum of the resistance to momentum transfer (r_{am}) and the excess resistance (r_{bh}).

$$r_H = r_{am} + r_{bh} \tag{B.10}$$

The r_{am} term can be estimated as a function of the wind speed (u) and friction velocity (u_*).

$$r_{am} = \frac{u}{u_*^2} \tag{B.11}$$

The r_{bh} can be estimated as a function of the empirical parameter kB^{-1}.

$$r_{bh} = \frac{1}{\kappa u_*} kB^{-1} \tag{B.12}$$

Various empirical formulas for kB^{-1} have been proposed. We tested 12 formulas summarized by Verhoef et al. (1997) and Hong et al. (2012).

B.2.1 Reynold's number

Many of the empirical formulas for kB^{-1} require an estimate of the Reynold's number (Re^*), which is a function of u_*, the roughness length for momentum (z_{0m}), and the kinematic viscosity of air (v).

$$Re^* = \frac{u_* z_{0m}}{v} \tag{B.13}$$

The z_{0m} term is a function of the zero-plane displacement height (d), u_*, and u at height z.

$$z_{0m} = \frac{z - d}{exp\left(\frac{\kappa u(z)}{u_*}\right)} \tag{B.14}$$

The d term was estimated using wind profile data from the flux towers. We optimized Equation B.15 to find the single value of d that minimized the residual between the left and right sides of the equation (Young et al., 2021).

$$\frac{\kappa(u_1 - u_2)}{u_*} = log\left(\frac{z_1 - d}{z_2 - d}\right) \tag{B.15}$$

The optimization for d was calculated independently for each site and month in the data set to account for temporal variability in vegetation structure that may affect r_H.

B.2.2 Model selection

The 12 formulas for kB^{-1} were forced with the flux tower measurements from the riparian woodland and upland savanna. The kB^{-1} values were used to produce empirical estimates of r_H. The estimates of r_H were compared to the "true" values of r_H, which were calculated directly from T_c and T_a measurements by inverting Equation B.6 (Verhoef

et al., 1997; Figure B.7).

$$r_H = \frac{\rho c_p (T_L - T_a)}{H} \tag{B.16}$$

The median absolute error was used to compare the modeled and observed values of r_H and select the formula for kB^{-1} that produced the most accurate estimates of r_H (Table B.1). The formula proposed by Thom (1972) was selected. It yielded strong model fit for both the riparian woodland and upland savanna.

Table B.1: Comparison of prediction errors for estimates of r_H calculated using different empirical formulas for kB^{-1}.

kB^{-1} Formula	Reference	Median Absolute Error (sm^{-1})		
		Riparian Woodland	Upland Savanna	Average
$1.35\kappa(100u_*)^{1/3}$	Thom (1972)	7.25	9.10	8.18
$ln(1)$	Hong et al. (2012)	4.42	12.43	8.43
$ln(10)$	Hong et al. (2012)	8.60	10.07	9.34
$ln(100)$	Hong et al. (2012)	19.71	16.73	18.22
$0.1k\sqrt{Re*}$	Zilitinkevich (1995)	49.57	16.97	33.27
$ln(\kappa u_* z_{0m}/\kappa_\theta)$	Sheppard (1958)	46.18	37.19	41.68
$ln(Pr(Re*))$	Sheppard (1958)	50.62	42.40	46.51
$3\kappa Pr^{2/3}+ln(Re*Pr^{1/3}/3)$	Kondo (1975)	51.13	43.08	47.10
$0.13(Re*)^{0.45}$	Zeng and Dickinson (1998)	92.96	42.65	67.80
$1.29(Re*)^{0.25}-ln(7.4)$	Kanda et al. (2007)	90.20	57.40	73.80
$2.46(Re*)^{0.25}-2$	Brutsaert (1982)	184.87	131.22	158.05
$0.52\kappa(8Re*)^{0.45}Pr^{0.8}$	Owen and Thomson (1963)	302.57	157.22	229.90

B.3   Derivation of coefficients for Equation 2.21

$$T_{c,ne} = T_a + \frac{(SW\downarrow - SW\uparrow + \varepsilon_L LW\downarrow - \varepsilon_L \sigma T_{c,ne}^4 - G)r_H}{\rho c_p} \tag{B.17}$$

$$0 = T_a + \frac{(SW\downarrow - SW\uparrow + \varepsilon_L LW\downarrow - \varepsilon_L \sigma T_{c,ne}^4 - G)r_H}{\rho c_p} - T_{c,ne} \tag{B.18}$$

$$0 = T_a \rho c_p + (SW\downarrow - SW\uparrow + \varepsilon_L LW\downarrow - \varepsilon_L \sigma T_{c,ne}^4 - G)r_H - T_{c,ne}\rho c_p \tag{B.19}$$

$$0 = T_a \rho c_p + (SW\downarrow - SW\uparrow + \varepsilon_L LW\downarrow - G)r_H - \varepsilon_L \sigma T_{c,ne}^4 r_H - T_{c,ne}\rho c_p \tag{B.20}$$

$$0 = T_{c,ne}^4(-\varepsilon_L \sigma r_H) + T_{c,ne}(-\rho c_p) + T_a \rho c_p +$$
$$(SW\downarrow - SW\uparrow + \varepsilon_L LW\downarrow - G)r_H \tag{B.21}$$

$$0 = T_{c,ne}^4 \frac{-\varepsilon_L \sigma r_H}{\rho c_p} - T_{c,ne} + T_a + \frac{(SW\downarrow - SW\uparrow + \varepsilon_L LW\downarrow - G)r_H}{\rho c_p} \tag{B.22}$$
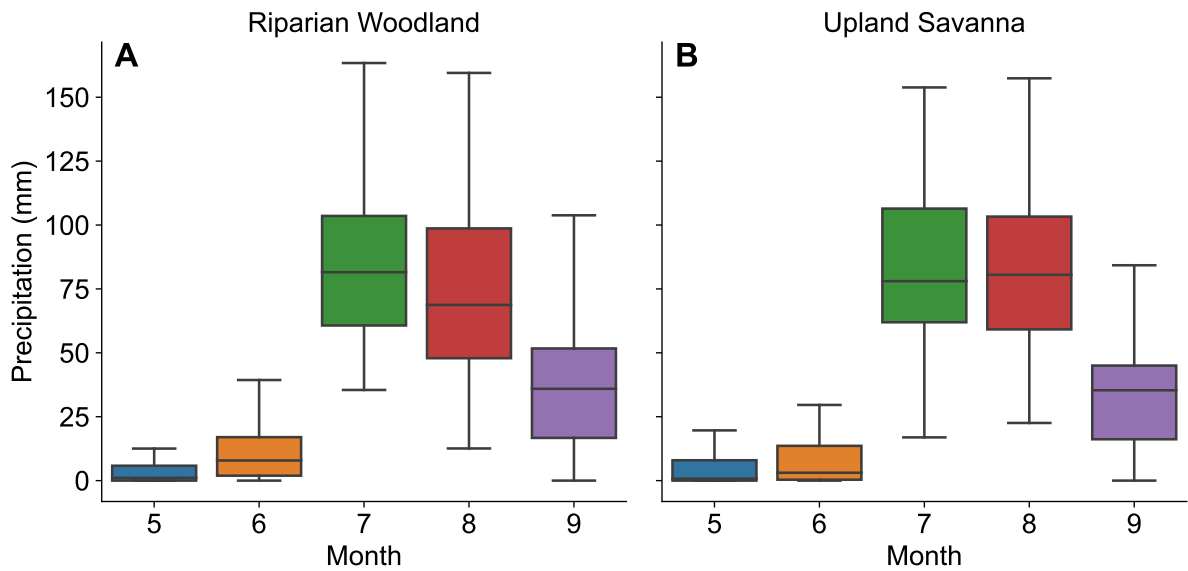
B.4 Figures

Figure B.1: Boxplots of monthly total precipitation (mm) in the riparian woodland (a) and upland savanna (b). Outliers are not shown.
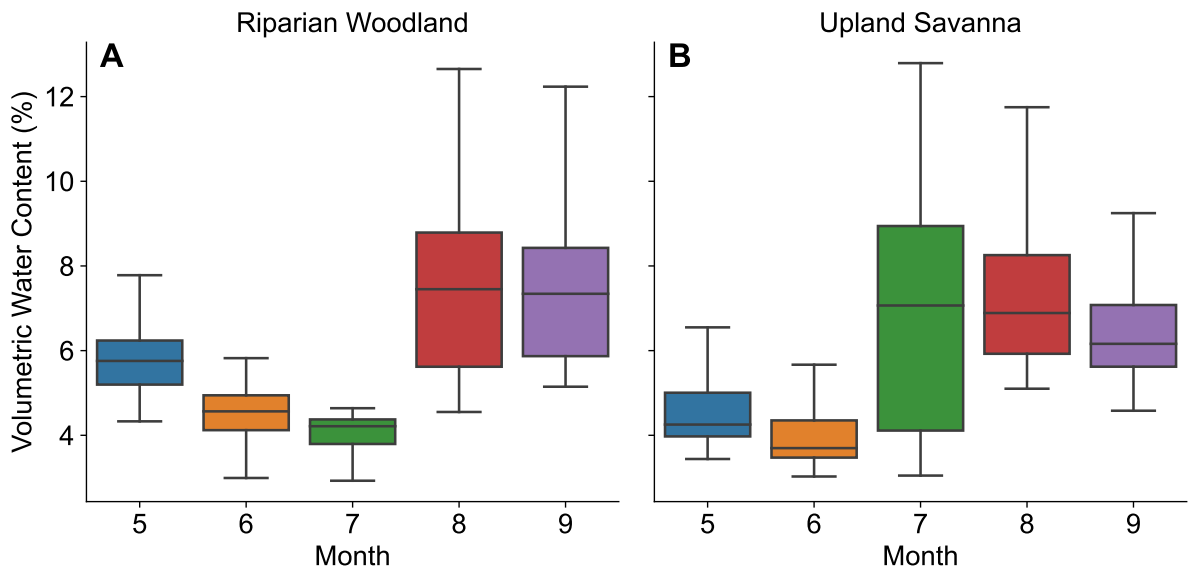

Figure B.2: Boxplots of soil volumetric water content (%) in the riparian woodland (a) and upland savanna (b). Data are measured at depths of 22.5 cm and 20 cm, respectively. Outliers are not shown.
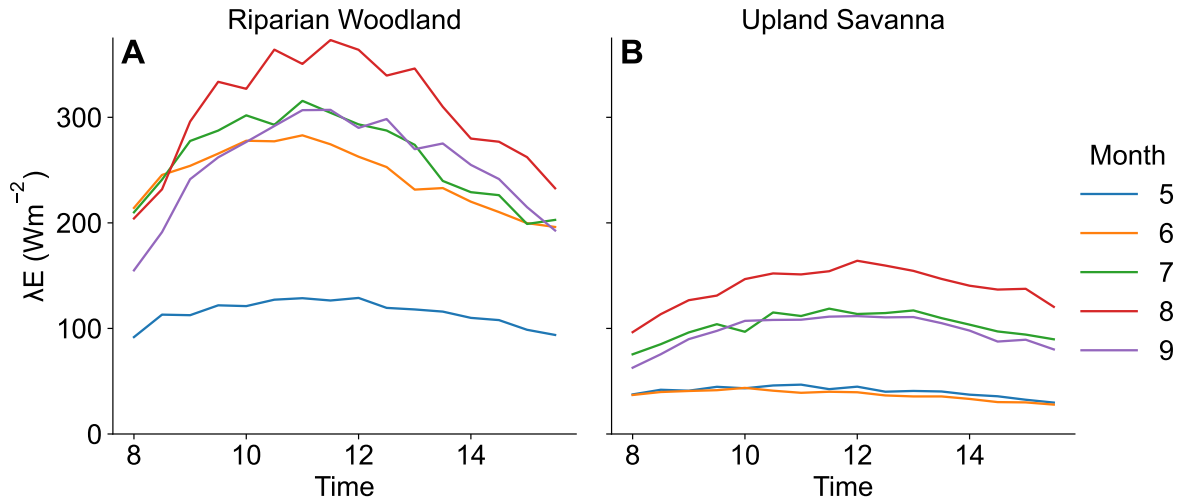
Figure B.3: Diurnal and seasonal climatology of latent heat flux (λE) in the riparian woodland (a) and upland savanna (b). The colored lines represent the mean values for each time of day, grouped by month of the growing season.
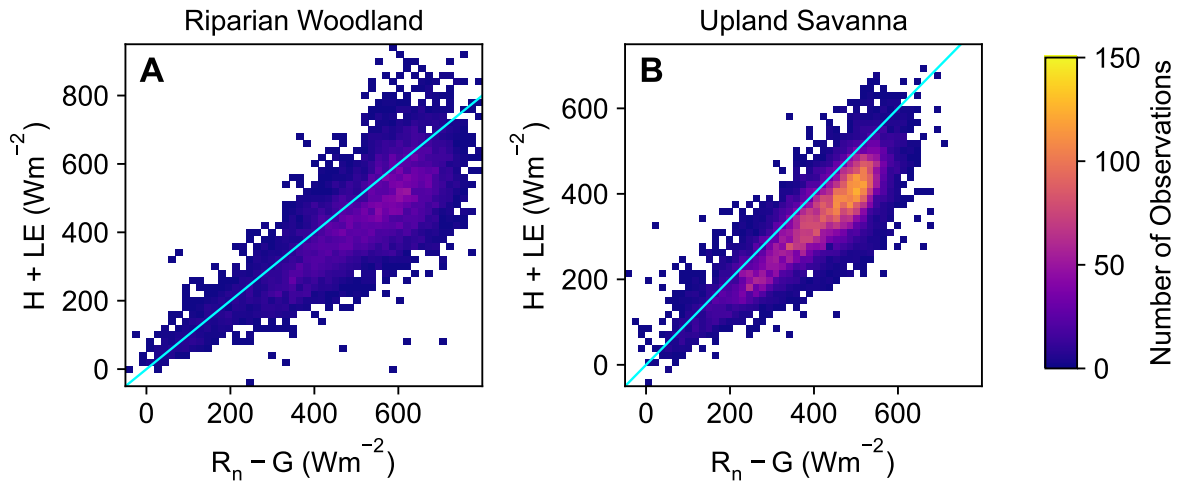

Figure B.4: Comparison of measured $H + \lambda E$ and $R_n - G$ in the riparian woodland (a) and the upland savanna (b). Some outliers are outside of the plotted range. The color scale saturates when there are more than 150 observations in a given portion of the feature space.

Figure B.5: Comparison of the energy balance closure ratio (C) and the prediction error for T_c in the riparian woodland (a) and the upland savanna (b). Some outliers are outside of the plotted range. The color scale saturates when there are more then 50 observations in a given portion of the feature space.
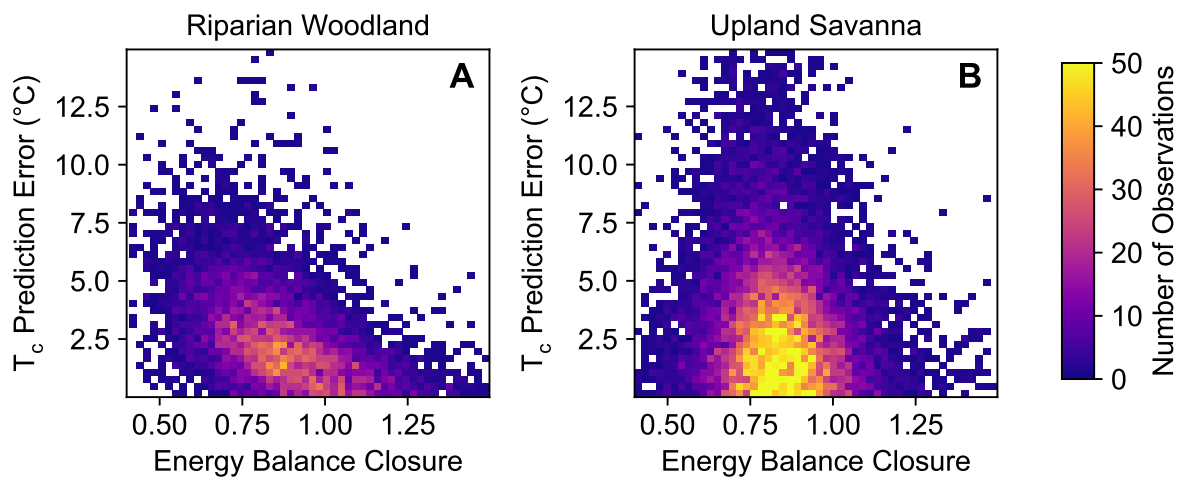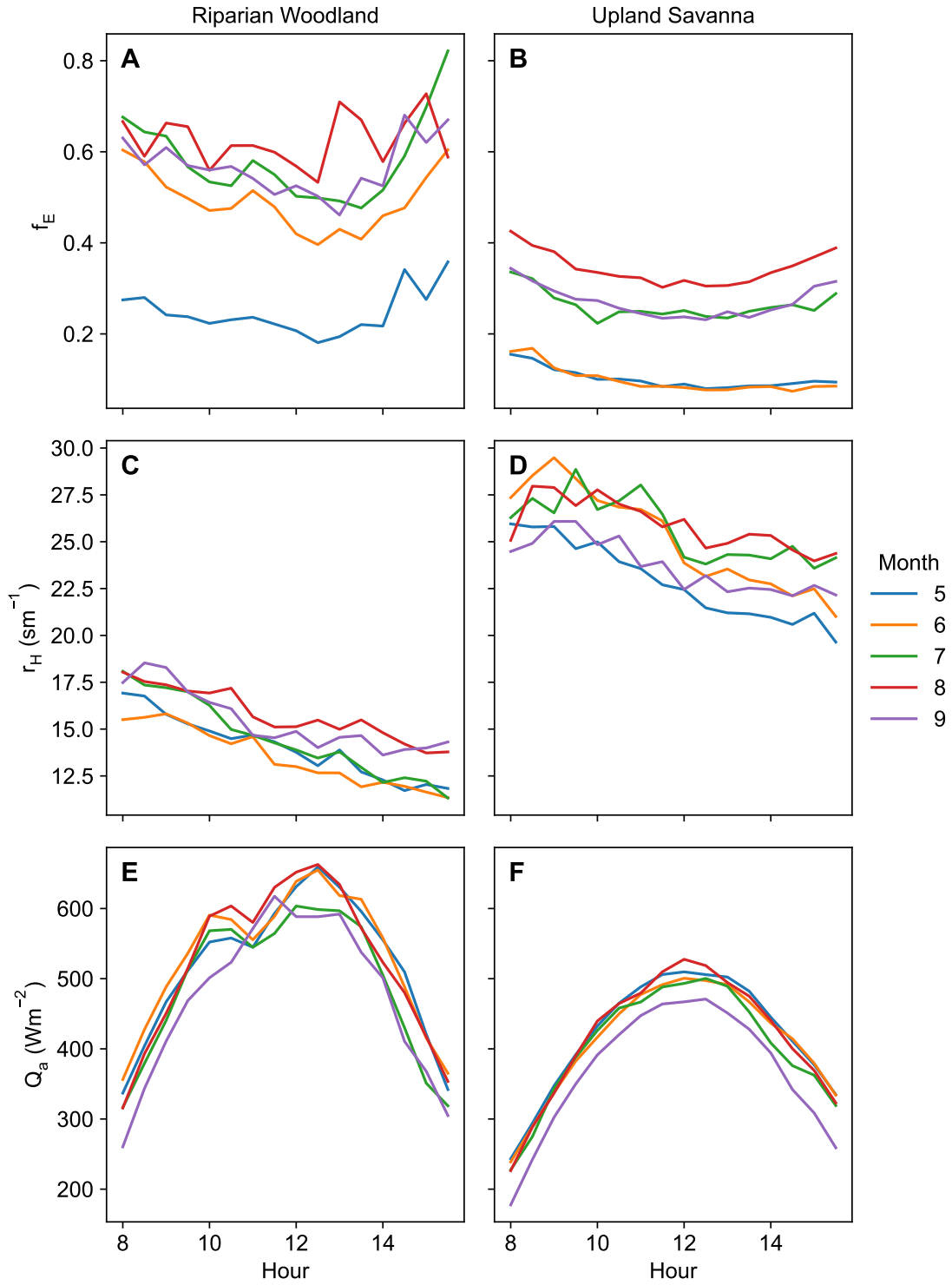
Figure B.6: Diurnal and seasonal climatology of f_E (a,b), r_H (c,d), and Q_a (e,f) in the riparian woodland (a,c,e) and upland savanna (b,d,f). The colored lines represent the mean values for each time of day, grouped by month of the growing season.

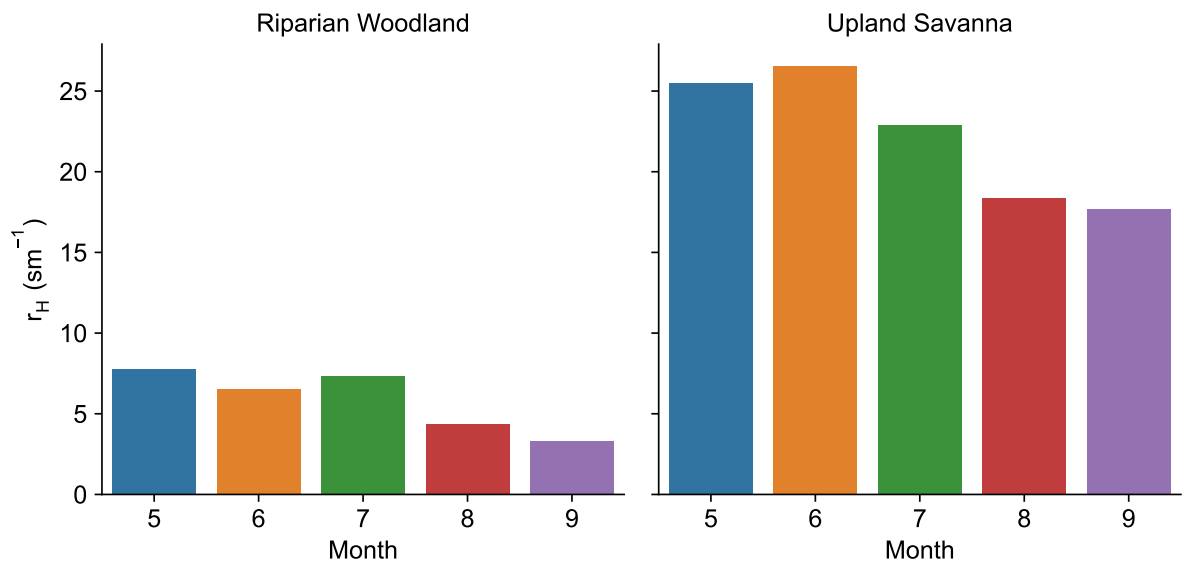Figure B.7: Values of r_H that were calculated directly from T_c and T_a measurements using Equation B.16.
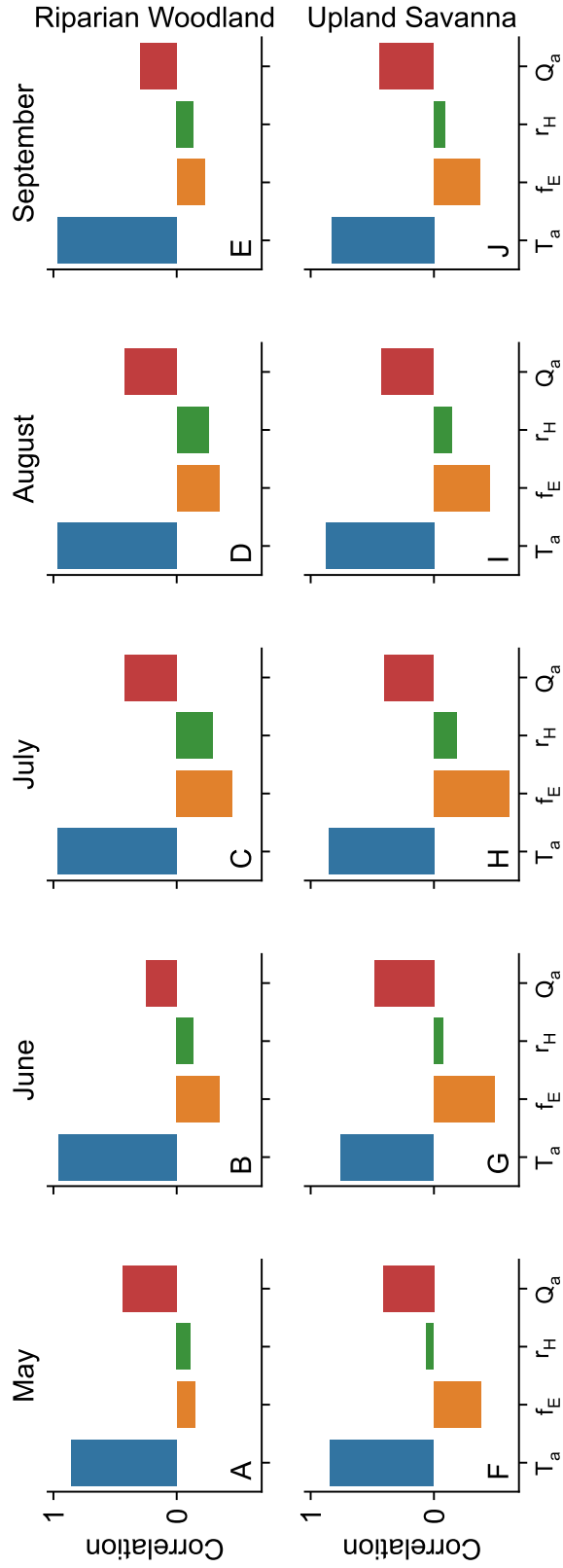
Figure B.8: Spearman rank correlations between T_c and air temperature (T_a), evaporative fraction (f_E), resistance to sensible heat flux (r_H), and available energy (Q_a) in the riparian woodland (a-e) and upland savanna (f-j). The colored bars represent the correlations for each month of the growing season.

Bibliography

J. T. Abatzoglou. Development of gridded surface meteorological data for ecological applications and modelling. *International Journal of Climatology*, 33(1):121–131, Jan. 2013. ISSN 08998418. doi: 10.1002/joc.3413. URL `http://doi.wiley.com/10.1002/joc.3413`.

D. Ackerly, C. Knight, S. Weiss, K. Barton, and K. Starmer. Leaf size, specific leaf area and microhabitat distribution of chaparral woody plants: contrasting patterns in species level and community level analyses. *Oecologia*, 130(3):449–457, Feb. 2002. ISSN 0029-8549, 1432-1939. doi: 10.1007/s004420100805. URL `http://link.springer.com/10.1007/s004420100805`.

J. B. Adams, D. E. Sabol, V. Kapos, R. A. Filho, D. A. Roberts, M. O. Smith, and A. R. Gillespie. Classification of multispectral images based on fractions of endmembers: Application to land-cover change in the Brazilian Amazon. *Remote Sensing of Environment*, 52(2):137–154, May 1995. ISSN 00344257. doi: 10.1016/0034-4257(94)00098-8. URL `http://linkinghub.elsevier.com/retrieve/pii/0034425794000988`.

C. D. Allen, A. K. Macalady, H. Chenchouni, D. Bachelet, N. McDowell, M. Vennetier, T. Kitzberger, A. Rigling, D. D. Breshears, E. T. Hogg, P. Gonzalez, R. Fensham, Z. Zhang, J. Castro, N. Demidova, J.-H. Lim, G. Allard, S. W. Running, A. Semerci, and N. Cobb. A global overview of drought and heat-induced tree mortality reveals emerging climate change risks for forests. *Forest Ecology and Management*, 259(4): 660–684, Feb. 2010. ISSN 03781127. doi: 10.1016/j.foreco.2009.09.001. URL `https://linkinghub.elsevier.com/retrieve/pii/S037811270900615X`.

C. D. Allen, D. D. Breshears, and N. G. McDowell. On underestimation of global vulnerability to tree mortality and forest die-off from hotter drought in the Anthropocene. *Ecosphere*, 6(8):art129, Aug. 2015. ISSN 2150-8925. doi: 10.1890/ES15-00203.1. URL `http://doi.wiley.com/10.1890/ES15-00203.1`.

R. G. Allen, L. S. Pereira, D. Raes, and M. Smith. Crop evapotranspiration: guidelines for computing crop water requirements. Irrigation and Drainage Paper 56, Food and Agriculture Organization of the United Nations, Rome, Italy, 1998.

N. M. Amlin and S. B. Rood. Drought stress and recovery of riparian cottonwoods due to water table alteration along Willow Creek, Alberta. *Trees*, 17(4):351–358, July 2003. ISSN 0931-1890, 1432-2285. doi: 10.1007/s00468-003-0245-3. URL `http://link.springer.com/10.1007/s00468-003-0245-3`.

J. S. Amthor. Scaling CO2-photosynthesis relationships from the leaf to the canopy. *Photosynthesis Research*, 39(3):321–350, Mar. 1994. ISSN 0166-8595, 1573-5079. doi: 10.1007/BF00014590. URL `http://link.springer.com/10.1007/BF00014590`.

W. R. L. Anderegg, J. M. Kane, and L. D. L. Anderegg. Consequences of widespread tree mortality triggered by drought and temperature stress. *Nature Climate Change*, 3(1):30–36, Jan. 2013. ISSN 1758-678X, 1758-6798. doi: 10.1038/nclimate1635. URL `http://www.nature.com/articles/nclimate1635`.

T. Andersen, J. Carstensen, E. Hernández-García, and C. M. Duarte. Ecological thresholds and regime shifts: approaches to identification. *Trends in Ecology & Evolution*, 24(1):49–57, Jan. 2009. ISSN 01695347. doi: 10.1016/j.tree.2008.07.014. URL `https://linkinghub.elsevier.com/retrieve/pii/S0169534708003054`.

M. C. Anderson, R. G. Allen, A. Morse, and W. P. Kustas. Use of Landsat thermal imagery in monitoring evapotranspiration and managing water resources. *Remote Sensing of Environment*, 122:50–65, July 2012. ISSN 00344257. doi: 10.1016/j.rse.2011.08.025. URL `https://linkinghub.elsevier.com/retrieve/pii/S0034425712000326`.

A. H. Arizpe, D. A. Falk, C. A. Woodhouse, and T. W. Swetnam. Widespread fire years in the US–Mexico Sky Islands are contingent on both winter and monsoon precipitation. *International Journal of Wildland Fire*, 29(12):1072, 2020. ISSN 1049-8001. doi: 10.1071/WF19181. URL `http://www.publish.csiro.au/?paper=WF19181`.

G. P. Asner, P. G. Brodrick, C. B. Anderson, N. Vaughn, D. E. Knapp, and R. E. Martin. Progressive forest canopy water loss during the 2012–2015 California drought. *Proceedings of the National Academy of Sciences*, 113(2):E249–E255, Jan. 2016. ISSN 0027-8424, 1091-6490. doi: 10.1073/pnas.1523397113. URL `http://www.pnas.org/lookup/doi/10.1073/pnas.1523397113`.

O. K. Atkin, K. J. Bloomfield, P. B. Reich, M. G. Tjoelker, G. P. Asner, D. Bonal, G. Bönisch, M. G. Bradford, L. A. Cernusak, E. G. Cosio, D. Creek, K. Y. Crous, T. F. Domingues, J. S. Dukes, J. J. G. Egerton, J. R. Evans, G. D. Farquhar, N. M. Fyllas, P. P. G. Gauthier, E. Gloor, T. E. Gimeno, K. L. Griffin, R. Guerrieri, M. A. Heskel, C. Huntingford, F. Y. Ishida, J. Kattge, H. Lambers, M. J. Liddell, J. Lloyd, C. H. Lusk, R. E. Martin, A. P. Maksimov, T. C. Maximov, Y. Malhi, B. E. Medlyn, P. Meir, L. M. Mercado, N. Mirotchnick, D. Ng, U. Niinemets, O. S. O'Sullivan, O. L. Phillips, L. Poorter, P. Poot, I. C. Prentice, N. Salinas, L. M. Rowland, M. G. Ryan, S. Sitch, M. Slot, N. G. Smith, M. H. Turnbull, M. C. VanderWel, F. Valladares, E. J. Veneklaas, L. K. Weerasinghe, C. Wirth, I. J. Wright, K. R. Wythers, J. Xiang,

S. Xiang, and J. Zaragoza-Castells. Global variability in leaf respiration in relation to climate, plant functional types and leaf traits. *New Phytologist*, 206(2):614–636, Apr. 2015. ISSN 0028-646X, 1469-8137. doi: 10.1111/nph.13253. URL `https://onlinelibrary.wiley.com/doi/10.1111/nph.13253`.

D. M. Aubrecht, B. R. Helliker, M. L. Goulden, D. A. Roberts, C. J. Still, and A. D. Richardson. Continuous, long-term, high-frequency thermal imaging of vegetation: Uncertainties and recommended best practices. *Agricultural and Forest Meteorology*, 228-229:315–326, Nov. 2016. ISSN 01681923. doi: 10.1016/j.agrformet.2016.07.017. URL `https://linkinghub.elsevier.com/retrieve/pii/S0168192316303434`.

C. Bachofen, L. Hülsmann, A. Revill, N. Buchmann, and P. D'Odorico. Accounting for foliar gradients in Vcmax and Jmax improves estimates of net CO2 exchange of forests. *Agricultural and Forest Meteorology*, 314:108771, Mar. 2022. ISSN 01681923. doi: 10.1016/j.agrformet.2021.108771. URL `https://linkinghub.elsevier.com/retrieve/pii/S0168192321004573`.

F. R. Balding and G. L. Cunningham. A Comparison of Heat Transfer Characteristics of Simple and Pinnate Leaf Models. *Botanical Gazette*, 137(1):65–74, Mar. 1976. ISSN 0006-8071. doi: 10.1086/336843. URL `https://www.journals.uchicago.edu/doi/10.1086/336843`.

D. Baldocchi, D. Matt, B. Hutchison, and R. Mcmillen. Solar radiation within an oak—hickory forest: an evaluation of the extinction coefficients for several radiation components during fully-leafed and leafless periods. *Agricultural and Forest Meteorology*, 32(3-4):307–322, Sept. 1984. ISSN 01681923. doi: 10.1016/0168-1923(84)90056-X. URL `https://linkinghub.elsevier.com/retrieve/pii/016819238490056X`.

D. Baldocchi, S. Knox, I. Dronova, J. Verfaillie, P. Oikawa, C. Sturtevant, J. H. Matthes, and M. Detto. The impact of expanding flooded land area on the annual evaporation of rice. *Agricultural and Forest Meteorology*, 223:181–193, June 2016. ISSN 01681923. doi: 10.1016/j.agrformet.2016.04.001. URL `https://linkinghub.elsevier.com/retrieve/pii/S0168192316302155`.

C. Ballester, M. Jiménez-Bello, J. Castel, and D. Intrigliolo. Usefulness of thermography for plant water stress detection in citrus and persimmon trees. *Agricultural and Forest Meteorology*, 168:120–129, Jan. 2013. ISSN 01681923. doi: 10.1016/j.agrformet.2012.08.005. URL `https://linkinghub.elsevier.com/retrieve/pii/S0168192312002572`.

A. Barr, A. Richardson, D. Hollinger, D. Papale, M. Arain, T. Black, G. Bohrer, D. Dragoni, M. Fischer, L. Gu, B. Law, H. Margolis, J. McCaughey, J. Munger, W. Oechel, and K. Schaeffer. Use of change-point detection for friction–velocity threshold evaluation in eddy-covariance studies. *Agricultural and Forest Meteorology*, 171-

172:31–45, Apr. 2013. ISSN 01681923. doi: 10.1016/j.agrformet.2012.11.023. URL `https://linkinghub.elsevier.com/retrieve/pii/S0168192312003607`.

A. G. Barr, T. Black, E. Hogg, N. Kljun, K. Morgenstern, and Z. Nesic. Inter-annual variability in the leaf area index of a boreal aspen-hazelnut forest in relation to net ecosystem production. *Agricultural and Forest Meteorology*, 126(3-4): 237–255, Nov. 2004. ISSN 01681923. doi: 10.1016/j.agrformet.2004.06.011. URL `https://linkinghub.elsevier.com/retrieve/pii/S0168192304001686`.

O. V. Barron, I. Emelyanova, T. G. Van Niel, D. Pollock, and G. Hodgson. Mapping groundwater-dependent ecosystems using remote sensing measures of vegetation and moisture dynamics. *Hydrological Processes*, 28(2):372–385, Jan. 2014. ISSN 08856087. doi: 10.1002/hyp.9609. URL `http://doi.wiley.com/10.1002/hyp.9609`.

H. L. Bateman and D. M. Merritt. Complex riparian habitats predict reptile and amphibian diversity. *Global Ecology and Conservation*, 22:e00957, June 2020. ISSN 23519894. doi: 10.1016/j.gecco.2020.e00957. URL `https://linkinghub.elsevier.com/retrieve/pii/S2351989419306699`.

D. Bates, M. Mächler, B. Bolker, and S. Walker. Fitting Linear Mixed-Effects Models Using **lme4**. *Journal of Statistical Software*, 67(1), 2015. ISSN 1548-7660. doi: 10.18637/jss.v067.i01. URL `http://www.jstatsoft.org/v67/i01/`.

B. Beisner, D. Haydon, and K. Cuddington. Alternative stable states in ecology. *Frontiers in Ecology and the Environment*, 1(7):376–382, Sept. 2003. ISSN 1540-9295. doi: 10.1890/1540-9295(2003)001[0376:ASSIE]2.0.CO;2. URL `http://doi.wiley.com/10.1890/1540-9295(2003)001[0376:ASSIE]2.0.CO;2`.

E. E. Beller, P. W. Downs, R. M. Grossinger, B. K. Orr, and M. N. Salomon. From past patterns to future potential: using historical ecology to inform river restoration on an intermittent California river. *Landscape Ecology*, 31(3):581–600, Mar. 2016. ISSN 0921-2973, 1572-9761. doi: 10.1007/s10980-015-0264-7. URL `http://link.springer.com/10.1007/s10980-015-0264-7`.

N. Berg and A. Hall. Increased Interannual Precipitation Extremes over California under Climate Change. *Journal of Climate*, 28(16):6324–6334, Aug. 2015. ISSN 0894-8755, 1520-0442. doi: 10.1175/JCLI-D-14-00624.1. URL `http://journals.ametsoc.org/doi/10.1175/JCLI-D-14-00624.1`.

C. J. Bernacchi, E. L. Singsaas, C. Pimentel, A. R. Portis Jr, and S. P. Long. Improved temperature response functions for models of Rubisco-limited photosynthesis: *In vivo* Rubisco enzyme kinetics. *Plant, Cell & Environment*, 24(2):253–259, Feb. 2001. ISSN 01407791. doi: 10.1111/j.1365-3040.2001.00668.x. URL `https://onlinelibrary.wiley.com/doi/10.1111/j.1365-3040.2001.00668.x`.

B. Blonder and S. T. Michaletz. A model for leaf temperature decoupling from air temperature. *Agricultural and Forest Meteorology*, 262:354–360, Nov. 2018. ISSN 01681923. doi: 10.1016/j.agrformet.2018.07.012. URL https://linkinghub.elsevier.com/retrieve/pii/S0168192318302338.

B. Blonder, S. Escobar, R. E. Kapás, and S. T. Michaletz. Low predictability of energy balance traits and leaf temperature metrics in desert, montane and alpine plant communities. *Functional Ecology*, 34(9):1882–1897, Sept. 2020. ISSN 0269-8463, 1365-2435. doi: 10.1111/1365-2435.13643. URL https://onlinelibrary.wiley.com/doi/10.1111/1365-2435.13643.

P. V. Bolstad and S. T. Gower. Estimation of leaf area index in fourteen southern Wisconsin forest stands using a portable radiometer. *Tree Physiology*, 7(1-2-3-4): 115–124, Dec. 1990. ISSN 0829-318X, 1758-4469. doi: 10.1093/treephys/7.1-2-3-4.115. URL https://academic.oup.com/treephys/article-lookup/doi/10.1093/treephys/7.1-2-3-4.115.

D. Bonal, A. Bosc, S. Ponton, J.-Y. Goret, B. Burban, P. Gross, J.-M. Bonnefond, J. Elbers, B. Longdoz, D. Epron, J.-M. Guehl, and A. Granier. Impact of severe dry season on net ecosystem exchange in the Neotropical rainforest of French Guiana. *Global Change Biology*, 14(8):1917–1933, Aug. 2008. ISSN 13541013. doi: 10.1111/j.1365-2486.2008.01610.x. URL https://onlinelibrary.wiley.com/doi/10.1111/j.1365-2486.2008.01610.x.

G. B. Bonan. *Ecological climatology: concepts and applications*. Cambridge University Press, New York, NY, USA, third edition edition, 2016. ISBN 978-1-107-04377-0 978-1-107-61905-0.

D. D. Breshears, N. S. Cobb, P. M. Rich, K. P. Price, C. D. Allen, R. G. Balice, W. H. Romme, J. H. Kastens, M. L. Floyd, J. Belnap, J. J. Anderson, O. B. Myers, and C. W. Meyer. Regional vegetation die-off in response to global-change-type drought. *Proceedings of the National Academy of Sciences*, 102(42):15144–15148, Oct. 2005. ISSN 0027-8424, 1091-6490. doi: 10.1073/pnas.0505734102. URL https://pnas.org/doi/full/10.1073/pnas.0505734102.

P. D. Brooks, J. Chorover, Y. Fan, S. E. Godsey, R. M. Maxwell, J. P. McNamara, and C. Tague. Hydrological partitioning in the critical zone: Recent advances and opportunities for developing transferable understanding of water cycle dynamics. *Water Resources Research*, 51(9):6973–6987, Sept. 2015. ISSN 00431397. doi: 10.1002/2015WR017039. URL http://doi.wiley.com/10.1002/2015WR017039.

W. Brutsaert. *Evaporation into the Atmosphere: Theory, History and Applications*. Springer Netherlands, Dordrecht, 1982. ISBN 978-94-017-1497-6. OCLC: 851369228.

M. Béland and D. Baldocchi. Is foliage clumping an outcome of resource limitations within forests? *Agricultural and Forest Meteorology*, 295:108185, Dec. 2020. ISSN 01681923. doi: 10.1016/j.agrformet.2020.108185. URL `https://linkinghub.elsevier.com/retrieve/pii/S0168192320302872`.

M. Béland and D. D. Baldocchi. Vertical structure heterogeneity in broadleaf forests: Effects on light interception and canopy photosynthesis. *Agricultural and Forest Meteorology*, 307:108525, Sept. 2021. ISSN 01681923. doi: 10.1016/j.agrformet.2021.108525. URL `https://linkinghub.elsevier.com/retrieve/pii/S0168192321002094`.

M. Béland and H. Kobayashi. Mapping forest leaf area density from multiview terrestrial lidar. *Methods in Ecology and Evolution*, 12(4):619–633, Apr. 2021. ISSN 2041-210X, 2041-210X. doi: 10.1111/2041-210X.13550. URL `https://onlinelibrary.wiley.com/doi/10.1111/2041-210X.13550`.

F. E. Carswell, P. Meir, E. V. Wandelli, L. C. M. Bonates, B. Kruijt, E. M. Barbosa, A. D. Nobre, J. Grace, and P. G. Jarvis. Photosynthetic capacity in a central Amazonian rain forest. *Tree Physiology*, 20(3):179–186, Feb. 2000. ISSN 0829-318X, 1758-4469. doi: 10.1093/treephys/20.3.179. URL `https://academic.oup.com/treephys/article-lookup/doi/10.1093/treephys/20.3.179`.

M. A. Cavaleri. Cold-blooded forests in a warming world. *New Phytologist*, 228(5): 1455–1457, Dec. 2020. ISSN 0028-646X, 1469-8137. doi: 10.1111/nph.16916. URL `https://onlinelibrary.wiley.com/doi/10.1111/nph.16916`.

J. Chen, P. Blanken, T. Black, M. Guilbeault, and S. Chen. Radiation regime and canopy architecture in a boreal aspen forest. *Agricultural and Forest Meteorology*, 86 (1-2):107–125, Aug. 1997. ISSN 01681923. doi: 10.1016/S0168-1923(96)02402-1. URL `https://linkinghub.elsevier.com/retrieve/pii/S0168192396024021`.

H. Chu, X. Luo, Z. Ouyang, W. S. Chan, S. Dengel, S. C. Biraud, M. S. Torn, S. Metzger, J. Kumar, M. A. Arain, T. J. Arkebauer, D. Baldocchi, C. Bernacchi, D. Billesbach, T. A. Black, P. D. Blanken, G. Bohrer, R. Bracho, S. Brown, N. A. Brunsell, J. Chen, X. Chen, K. Clark, A. R. Desai, T. Duman, D. Durden, S. Fares, I. Forbrich, J. A. Gamon, C. M. Gough, T. Griffis, M. Helbig, D. Hollinger, E. Humphreys, H. Ikawa, H. Iwata, Y. Ju, J. F. Knowles, S. H. Knox, H. Kobayashi, T. Kolb, B. Law, X. Lee, M. Litvak, H. Liu, J. W. Munger, A. Noormets, K. Novick, S. F. Oberbauer, W. Oechel, P. Oikawa, S. A. Papuga, E. Pendall, P. Prajapati, J. Prueger, W. L. Quinton, A. D. Richardson, E. S. Russell, R. L. Scott, G. Starr, R. Staebler, P. C. Stoy, E. Stuart-Haëntjens, O. Sonnentag, R. C. Sullivan, A. Suyker, M. Ueyama, R. Vargas, J. D. Wood, and D. Zona. Representativeness of Eddy-Covariance flux footprints for areas surrounding AmeriFlux sites. *Agricultural and Forest Meteorology*, 301-302:108350, May 2021. ISSN 01681923. doi: 10.1016/j.agrformet.2021.108350. URL `https://linkinghub.elsevier.com/retrieve/pii/S0168192321000332`.

R. M. Cionco. A wind-profile index for canopy flow. *Boundary-Layer Meteorology*, 3 (2):255–263, Dec. 1972. ISSN 0006-8314, 1573-1472. doi: 10.1007/BF02033923. URL `http://link.springer.com/10.1007/BF02033923`.

R. M. Cionco. Analysis of canopy index values for various canopy densities. *Boundary-Layer Meteorology*, 15(1):81–93, Aug. 1978. ISSN 0006-8314, 1573-1472. doi: 10.1007/BF00165507. URL `http://link.springer.com/10.1007/BF00165507`.

A. M. Cook, N. Berry, K. V. Milner, and A. Leigh. Water availability influences thermal safety margins for leaves. *Functional Ecology*, 35(10):2179–2189, Oct. 2021. ISSN 0269-8463, 1365-2435. doi: 10.1111/1365-2435.13868. URL `https://onlinelibrary.wiley.com/doi/10.1111/1365-2435.13868`.

B. D. Cook, K. J. Davis, W. Wang, A. Desai, B. W. Berger, R. M. Teclaw, J. G. Martin, P. V. Bolstad, P. S. Bakwin, C. Yi, and W. Heilman. Carbon exchange and venting anomalies in an upland deciduous forest in northern Wisconsin, USA. *Agricultural and Forest Meteorology*, 126(3-4):271–295, Nov. 2004. ISSN 01681923. doi: 10.1016/j.agrformet.2004.06.008. URL `https://linkinghub.elsevier.com/retrieve/pii/S0168192304001601`.

B. I. Cook, J. S. Mankin, K. Marvel, A. P. Williams, J. E. Smerdon, and K. J. Anchukaitis. Twenty-First Century Drought Projections in the CMIP6 Forcing Scenarios. *Earth's Future*, 8(6), June 2020. ISSN 2328-4277, 2328-4277. doi: 10.1029/2019EF001461. URL `https://onlinelibrary.wiley.com/doi/10.1029/2019EF001461`.

D. J. Cooper, D. R. D'Amico, and M. L. Scott. Physiological and Morphological Response Patterns of Populus deltoides to Alluvial Groundwater Pumping. *Environmental Management*, 31(2):215–226, Feb. 2003. ISSN 0364-152X, 1432-1009. doi: 10.1007/s00267-002-2808-2. URL `http://link.springer.com/10.1007/s00267-002-2808-2`.

I. R. Cowan and G. D. Farquhar. Stomatal function in relation to leaf metabolism and environment: Stomatal function in the regulation of gas exchange. page 19, Jan. 1977.

R. D. Crago. Conservation and variability of the evaporative fraction during the daytime. *Journal of Hydrology*, 180(1-4):173–194, May 1996. ISSN 00221694. doi: 10.1016/0022-1694(95)02903-6. URL `https://linkinghub.elsevier.com/retrieve/pii/0022169495029036`.

M. J. De Azevedo Falcão, B. Marland Torke, and V. De Freitas Mansano. A Taxonomic Revision of the Amazonian Genus Dicorynia (Fabaceae: Dialioideae). *Phytotaxa*, 554 (1):1–31, July 2022. ISSN 1179-3163, 1179-3155. doi: 10.11646/phytotaxa.554.1.1. URL `https://www.biotaxa.org/Phytotaxa/article/view/phytotaxa.554.1.1`.

P. De Frenne, J. Lenoir, M. Luoto, B. R. Scheffers, F. Zellweger, J. Aalto, M. B. Ashcroft, D. M. Christiansen, G. Decocq, K. De Pauw, S. Govaert, C. Greiser, E. Gril, A. Hampe, T. Jucker, D. H. Klinges, I. A. Koelemeijer, J. J. Lembrechts, R. Marrec, C. Meeussen, J. Ogée, V. Tyystjärvi, P. Vangansbeke, and K. Hylander. Forest microclimates and climate change: Importance, drivers and future research agenda. *Global Change Biology*, 27(11):2279–2297, June 2021. ISSN 1354-1013, 1365-2486. doi: 10.1111/gcb.15569. URL `https://onlinelibrary.wiley.com/doi/10.1111/gcb.15569`.

M. G. De Kauwe, B. E. Medlyn, A. J. Pitman, J. E. Drake, A. Ukkola, A. Griebel, E. Pendall, S. Prober, and M. Roderick. Examining the evidence for decoupling between photosynthesis and transpiration during heat extremes. *Biogeosciences*, 16(4):903–916, Feb. 2019. ISSN 1726-4189. doi: 10.5194/bg-16-903-2019. URL `https://bg.copernicus.org/articles/16/903/2019/`.

P. E. Dennison and D. A. Roberts. Endmember selection for multiple endmember spectral mixture analysis using endmember average RMSE. *Remote Sensing of Environment*, 87(2-3):123–135, Oct. 2003. ISSN 00344257. doi: 10.1016/S0034-4257(03)00135-4. URL `http://linkinghub.elsevier.com/retrieve/pii/S0034425703001354`.

N. S. Diffenbaugh and M. Ashfaq. Intensification of hot extremes in the United States. *Geophysical Research Letters*, 37(15):n/a–n/a, Aug. 2010. ISSN 00948276. doi: 10.1029/2010GL043888. URL `http://doi.wiley.com/10.1029/2010GL043888`.

N. S. Diffenbaugh, D. L. Swain, and D. Touma. Anthropogenic warming has increased drought risk in California. *Proceedings of the National Academy of Sciences*, 112(13): 3931–3936, Mar. 2015. ISSN 0027-8424, 1091-6490. doi: 10.1073/pnas.1422385112. URL `http://www.pnas.org/lookup/doi/10.1073/pnas.1422385112`.

C. Dong, G. M. MacDonald, K. Willis, T. W. Gillespie, G. S. Okin, and A. P. Williams. Vegetation Responses to 2012–2016 Drought in Northern and Southern California. *Geophysical Research Letters*, 46(7):3810–3821, Apr. 2019. ISSN 0094-8276, 1944-8007. doi: 10.1029/2019GL082137. URL `https://onlinelibrary.wiley.com/doi/abs/10.1029/2019GL082137`.

P. W. Downs, S. R. Dusterhoff, and W. A. Sears. Reach-scale channel sensitivity to multiple human activities and natural events: Lower Santa Clara River, California, USA. *Geomorphology*, 189:121–134, May 2013. ISSN 0169555X. doi: 10.1016/j.geomorph.2013.01.023. URL `http://linkinghub.elsevier.com/retrieve/pii/S0169555X13000603`.

J. E. Drake, M. G. Tjoelker, A. Vårhammar, B. Medlyn, P. B. Reich, A. Leigh, S. Pfautsch, C. J. Blackman, R. López, M. J. Aspinwall, K. Y. Crous, R. A. Duursma, D. Kumarathunge, M. G. De Kauwe, M. Jiang, A. B. Nicotra, D. T. Tissue, B. Choat, O. K. Atkin, and C. V. M. Barton. Trees tolerate an extreme heatwave via sustained transpirational cooling and increased leaf thermal tolerance. *Global Change Biology*, 24

(6):2390–2402, June 2018. ISSN 1354-1013, 1365-2486. doi: 10.1111/gcb.14037. URL `https://onlinelibrary.wiley.com/doi/10.1111/gcb.14037`.

J. E. Drake, R. Harwood, A. Va, P. B. Reich, C. V. M. Barton, and M. G. Tjoelker. No evidence of homeostatic regulation of leaf temperature in Eucalyptus parramattensis trees: integration of CO2 flux and oxygen isotope methodologies. *New Phytologist*, page 13, 2020.

P. L. Drake, R. H. Froend, and P. J. Franks. Smaller, faster stomata: scaling of stomatal size, rate of response, and stomatal conductance. *Journal of Experimental Botany*, 64 (2):495–505, Jan. 2013. ISSN 1460-2431, 0022-0957. doi: 10.1093/jxb/ers347. URL `https://academic.oup.com/jxb/article-lookup/doi/10.1093/jxb/ers347`.

S. Dufour, E. Muller, M. Straatsma, and S. Corgne. Image Utilisation for the Study and Management of Riparian Vegetation: Overview and Applications. In P. Carbonneau and H. Piégay, editors, *Fluvial remote sensing for science and management*, Advancing river restoration and management. Wiley-Blackwell, Chichester, West Sussex ; Hoboken, NJ, 2012. ISBN 978-0-470-71427-0.

K. E. Dybala, V. Matzek, T. Gardali, and N. E. Seavy. Carbon sequestration in riparian forests: A global synthesis and meta-analysis. *Global Change Biology*, 25(1):57–67, Jan. 2019. ISSN 1354-1013, 1365-2486. doi: 10.1111/gcb.14475. URL `https://onlinelibrary.wiley.com/doi/abs/10.1111/gcb.14475`.

M. M. Farella, J. B. Fisher, W. Jiao, K. B. Key, and M. L. Barnes. Thermal remote sensing for plant ecology from leaf to globe. *Journal of Ecology*, pages 1365–2745.13957, July 2022. ISSN 0022-0477, 1365-2745. doi: 10.1111/1365-2745.13957. URL `https://onlinelibrary.wiley.com/doi/10.1111/1365-2745.13957`.

G. D. Farquhar, S. von Caemmerer, and J. A. Berry. A biochemical model of photosynthetic CO2 assimilation in leaves of C3 species. *Planta*, 149(1):78–90, June 1980. ISSN 0032-0935, 1432-2048. doi: 10.1007/BF00386231. URL `http://link.springer.com/10.1007/BF00386231`.

R. Fichot, F. Brignolas, H. Cochard, and R. Ceulemans. Vulnerability to drought-induced cavitation in poplars: synthesis and future opportunities. *Plant, Cell & Environment*, 38(7):1233–1251, July 2015. ISSN 01407791. doi: 10.1111/pce.12491. URL `http://doi.wiley.com/10.1111/pce.12491`.

J. B. Fisher, R. J. Whittaker, and Y. Malhi. ET come home: potential evapotranspiration in geographical ecology: ET come home. *Global Ecology and Biogeography*, 20(1):1–18, Jan. 2011. ISSN 1466822X. doi: 10.1111/j.1466-8238.2010.00578.x. URL `http://doi.wiley.com/10.1111/j.1466-8238.2010.00578.x`.

A. T. Fotis and P. S. Curtis. Effects of structural complexity on within-canopy light environments and leaf traits in a northern mixed deciduous forest. *Tree Physiology*, page treephys;tpw124v1, Jan. 2017. ISSN 0829-318X, 1758-4469. doi: 10.1093/treephys/tpw124. URL `https://academic.oup.com/treephys/article-lookup/doi/10.1093/treephys/tpw124`.

E. Ganivet and R. Gaspard. Growth responses of neotropical trees to resource availability and individual condition : an innovative method using LIDAR canopy height model, 2013. URL `http://www.ecofog.gf/IMG/pdf/ganivet-gaspard.pdf`.

H. L. Gary. Root distribution of five-stamen tamarisk, seepwillow, and arrowweed. *Forest Science*, 9(3):311–314, 1963.

D. Gaumont-Guay, T. A. Black, H. Mccaughey, A. G. Barr, P. Krishnan, R. S. Jassal, and Z. Nesic. Soil CO_2 efflux in contrasting boreal deciduous and coniferous stands and its contribution to the ecosystem carbon balance. *Global Change Biology*, 15(5):1302–1319, May 2009. ISSN 13541013, 13652486. doi: 10.1111/j.1365-2486.2008.01830.x. URL `https://onlinelibrary.wiley.com/doi/10.1111/j.1365-2486.2008.01830.x`.

A. Gelman and J. Hill. *Data analysis using regression and multilevel/hierarchical models*. Analytical methods for social research. Cambridge University Press, New York, 2007. ISBN 978-0-521-86706-1 978-0-521-68689-1.

P. Gentine, D. Entekhabi, A. Chehbouni, G. Boulet, and B. Duchemin. Analysis of evaporative fraction diurnal behaviour. *Agricultural and Forest Meteorology*, 143(1-2):13–29, Mar. 2007. ISSN 01681923. doi: 10.1016/j.agrformet.2006.11.002. URL `https://linkinghub.elsevier.com/retrieve/pii/S016819230600339X`.

P. Gentine, D. Entekhabi, and J. Polcher. The Diurnal Behavior of Evaporative Fraction in the Soil–Vegetation–Atmospheric Boundary Layer Continuum. *Journal of Hydrometeorology*, 12(6):1530–1546, Dec. 2011. ISSN 1525-755X, 1525-7541. doi: 10.1175/2011JHM1261.1. URL `http://journals.ametsoc.org/doi/10.1175/2011JHM1261.1`.

M. L. Goulden and R. C. Bales. California forest die-off linked to multi-year deep soil drying in 2012–2015 drought. *Nature Geoscience*, 12(8):632–637, Aug. 2019. ISSN 1752-0894, 1752-0908. doi: 10.1038/s41561-019-0388-5. URL `http://www.nature.com/articles/s41561-019-0388-5`.

R. O. Green, M. L. Eastwood, C. M. Sarture, T. G. Chrien, M. Aronsson, B. J. Chippendale, J. A. Faust, B. E. Pavri, C. J. Chovit, M. Solis, M. R. Olah, and O. Williams. Imaging Spectroscopy and the Airborne Visible/Infrared Imaging Spectrometer (AVIRIS). *Remote Sensing of Environment*, 65(3):227–248, Sept. 1998. ISSN 00344257. doi: 10.1016/S0034-4257(98)00064-9. URL `https://linkinghub.elsevier.com/retrieve/pii/S0034425798000649`.

C. Grossiord, T. N. Buckley, L. A. Cernusak, K. A. Novick, B. Poulter, R. T. W. Siegwolf, J. S. Sperry, and N. G. McDowell. Plant responses to rising vapor pressure deficit. *New Phytologist*, 226(6):1550–1566, June 2020. ISSN 0028-646X, 1469-8137. doi: 10.1111/ nph.16485. URL `https://onlinelibrary.wiley.com/doi/10.1111/nph.16485`.

J. Gurevitch and P. H. Schuepp. Boundary layer properties of highly dissected leaves: an investigation using an electrochemical fluid tunnel. *Plant, Cell and Environment*, 13(8):783–792, Nov. 1990. ISSN 0140-7791, 1365-3040. doi: 10.1111/j.1365-3040.1990. tb01094.x. URL `https://onlinelibrary.wiley.com/doi/10.1111/j.1365-3040. 1990.tb01094.x`.

R. Hanson, P. Martin, and K. Koczot. Simulation of Ground-Water/Surface-Water Flow in the Santa Clara–Calleguas Ground-Water Basin, Ventura County, California. Water-Resources Investigations Report 02-4136, U.S. Geological Survey, Sacramento, California, 2003. URL `https://pubs.usgs.gov/wri/wri024136/text.html`.

J. Harlow and B. Hagedorn. SWB Modeling of Groundwater Recharge on Catalina Island, California, during a Period of Severe Drought. *Water*, 11(1):58, Dec. 2018. ISSN 2073-4441. doi: 10.3390/w11010058. URL `http://www.mdpi.com/2073-4441/11/1/58`.

C. R. Harris, K. J. Millman, S. J. van der Walt, R. Gommers, P. Virtanen, D. Cournapeau, E. Wieser, J. Taylor, S. Berg, N. J. Smith, R. Kern, M. Picus, S. Hoyer, M. H. van Kerkwijk, M. Brett, A. Haldane, J. F. del Río, M. Wiebe, P. Peterson, P. Gérard-Marchant, K. Sheppard, T. Reddy, W. Weckesser, H. Abbasi, C. Gohlke, and T. E. Oliphant. Array programming with NumPy. *Nature*, 585(7825):357–362, Sept. 2020. ISSN 0028-0836, 1476-4687. doi: 10.1038/s41586-020-2649-2. URL `https://www.nature.com/articles/s41586-020-2649-2`.

M. Havaux. Stress Tolerance of Photosystem II in Vivo. 100, 1992.

M. A. Heskel, O. K. Atkin, M. H. Turnbull, and K. L. Griffin. Bringing the Kok effect to light: A review on the integration of daytime respiration and net ecosystem exchange. *Ecosphere*, 4(8):art98, Aug. 2013. ISSN 2150-8925. doi: 10.1890/ES13-00120.1. URL `http://doi.wiley.com/10.1890/ES13-00120.1`.

M. A. Heskel, O. S. O'Sullivan, P. B. Reich, M. G. Tjoelker, L. K. Weerasinghe, A. Penillard, J. J. G. Egerton, D. Creek, K. J. Bloomfield, J. Xiang, F. Sinca, Z. R. Stangl, A. Martinez-de la Torre, K. L. Griffin, C. Huntingford, V. Hurry, P. Meir, M. H. Turnbull, and O. K. Atkin. Convergence in the temperature response of leaf respiration across biomes and plant functional types. *Proceedings of the National Academy of Sciences*, 113(14):3832–3837, Apr. 2016. ISSN 0027-8424, 1091-6490. doi: 10.1073/pnas. 1520282113. URL `https://pnas.org/doi/full/10.1073/pnas.1520282113`.

R. W. Higgins, Y. Yao, and X. L. Wang. Influence of the North American Monsoon System on the U.S. Summer Precipitation Regime. *Journal of Climate*, 10(10):

2600–2622, Oct. 1997. ISSN 0894-8755, 1520-0442. doi: 10.1175/1520-0442(1997)
010⟨2600:IOTNAM⟩2.0.CO;2. URL `http://journals.ametsoc.org/doi/10.1175/1520-0442(1997)010<2600:IOTNAM>2.0.CO;2`.

E. H. Hogg and P. A. Hurdle. Sap flow in trembling aspen: implications for stomatal responses to vapor pressure deficit. *Tree Physiology*, 17(8-9):501–509, Aug. 1997. ISSN 0829-318X, 1758-4469. doi: 10.1093/treephys/17.8-9.501. URL `https://academic.oup.com/treephys/article-lookup/doi/10.1093/treephys/17.8-9.501`.

J. Hong, J. Kim, and Y. H. Byun. Uncertainty in carbon exchange modelling in a forest canopy due to kB-1 Parametrizations on Carbon Exchange Modelling. *Quarterly Journal of the Royal Meteorological Society*, 138(664):699–706, Apr. 2012. ISSN 00359009. doi: 10.1002/qj.944. URL `https://onlinelibrary.wiley.com/doi/10.1002/qj.944`.

J. L. Horton, T. E. Kolb, and S. C. Hart. Responses of riparian trees to interannual variation in ground water depth in a semi-arid river basin. *Plant, Cell and Environment*, 24(3):293–304, Mar. 2001. ISSN 0140-7791, 1365-3040. doi: 10.1046/j.1365-3040.2001.00681.x. URL `http://doi.wiley.com/10.1046/j.1365-3040.2001.00681.x`.

Z. H. Hoylman, K. G. Jencso, J. Hu, Z. A. Holden, B. Allred, S. Dobrowski, N. Robinson, J. T. Martin, D. Affleck, and C. Seielstad. The Topographic Signature of Ecosystem Climate Sensitivity in the Western United States. *Geophysical Research Letters*, 46(24): 14508–14520, Dec. 2019. ISSN 0094-8276, 1944-8007. doi: 10.1029/2019GL085546. URL `https://onlinelibrary.wiley.com/doi/10.1029/2019GL085546`.

C.-y. Huang, W. R. Anderegg, and G. P. Asner. Remote sensing of forest die-off in the Anthropocene: From plant ecophysiology to canopy structure. *Remote Sensing of Environment*, 231:111233, Sept. 2019. ISSN 00344257. doi: 10.1016/j.rse.2019.111233. URL `https://linkinghub.elsevier.com/retrieve/pii/S0034425719302524`.

K. R. Hultine, R. Froend, D. Blasini, S. E. Bush, M. Karlinski, and D. F. Koepke. Hydraulic traits that buffer deep-rooted plants from changes in hydrology and climate. *Hydrological Processes*, 34(2):209–222, Jan. 2020. ISSN 0885-6087, 1099-1085. doi: 10.1002/hyp.13587. URL `https://onlinelibrary.wiley.com/doi/10.1002/hyp.13587`.

J. Huntington, K. McGwire, C. Morton, K. Snyder, S. Peterson, T. Erickson, R. Niswonger, R. Carroll, G. Smith, and R. Allen. Assessing the role of climate and resource management on groundwater dependent ecosystem changes in arid environments with the Landsat archive. *Remote Sensing of Environment*, 185:186–197, Nov. 2016. ISSN 00344257. doi: 10.1016/j.rse.2016.07.004. URL `https://linkinghub.elsevier.com/retrieve/pii/S0034425716302619`.

J. L. Huntington, K. C. Hegewisch, B. Daudert, C. G. Morton, J. T. Abatzoglou, D. J. McEvoy, and T. Erickson. Climate Engine: Cloud Computing and Visualization of Climate and Remote Sensing Data for Advanced Natural Resource Monitoring and Process Understanding. *Bulletin of the American Meteorological Society*, 98(11):2397–2410, Nov. 2017. ISSN 0003-0007, 1520-0477. doi: 10.1175/BAMS-D-15-00324.1. URL `https://journals.ametsoc.org/doi/10.1175/BAMS-D-15-00324.1`.

S. Idso, R. Jackson, P. Pinter, R. Reginato, and J. Hatfield. Normalizing the stress-degree-day parameter for environmental variability. *Agricultural Meteorology*, 24:45–55, Jan. 1981. ISSN 00021571. doi: 10.1016/0002-1571(81)90032-7. URL `https://linkinghub.elsevier.com/retrieve/pii/0002157181900327`.

R. D. Jackson, S. B. Idso, R. J. Reginato, and P. J. Pinter. Canopy temperature as a crop water stress indicator. *Water Resources Research*, 17(4):1133–1138, Aug. 1981. ISSN 00431397. doi: 10.1029/WR017i004p01133. URL `http://doi.wiley.com/10.1029/WR017i004p01133`.

K. G. Jencso and B. L. McGlynn. Hierarchical controls on runoff generation: Topographically driven hydrologic connectivity, geology, and vegetation. *Water Resources Research*, 47(11), Nov. 2011. ISSN 00431397. doi: 10.1029/2011WR010666. URL `http://doi.wiley.com/10.1029/2011WR010666`.

H. G. Jones. *Plants and microclimate: a quantitative approach to environmental plant physiology*. Cambridge University Press, Cambridge ; New York, third edition edition, 2014. ISBN 978-0-521-27959-8.

H. G. Jones, R. Serraj, B. R. Loveys, L. Xiong, A. Wheaton, and A. H. Price. Thermal infrared imaging of crop canopies for the remote diagnosis and quantification of plant responses to water stress in the field. *Functional Plant Biology*, 36(11):978, 2009. ISSN 1445-4408. doi: 10.1071/FP09123. URL `http://www.publish.csiro.au/?paper=FP09123`.

M. Kanda, M. Kanega, T. Kawai, R. Moriwaki, and H. Sugawara. Roughness Lengths for Momentum and Heat Derived from Outdoor Urban Scale Models. *Journal of Applied Meteorology and Climatology*, 46(7):1067–1079, July 2007. ISSN 1558-8432, 1558-8424. doi: 10.1175/JAM2500.1. URL `https://journals.ametsoc.org/doi/10.1175/JAM2500.1`.

G. Kar and A. Kumar. Surface energy fluxes and crop water stress index in groundnut under irrigated ecosystem. *Agricultural and Forest Meteorology*, 146(1-2):94–106, Sept. 2007. ISSN 01681923. doi: 10.1016/j.agrformet.2007.05.008. URL `https://linkinghub.elsevier.com/retrieve/pii/S016819230700144X`.

C. L. Kibler, A.-M. L. Parkinson, S. H. Peterson, D. A. Roberts, C. M. D'Antonio, S. K. Meerdink, and S. H. Sweeney. Monitoring Post-Fire Recovery of Chaparral

and Conifer Species Using Field Surveys and Landsat Time Series. *Remote Sensing*, 11(24):2963, Dec. 2019. ISSN 2072-4292. doi: 10.3390/rs11242963. URL `https://www.mdpi.com/2072-4292/11/24/2963`.

C. L. Kibler, E. C. Schmidt, D. A. Roberts, J. C. Stella, L. Kui, A. M. Lambert, and M. B. Singer. A brown wave of riparian woodland mortality following groundwater declines during the 2012–2019 California drought. *Environmental Research Letters*, 16(8):084030, Aug. 2021. ISSN 1748-9326. doi: 10.1088/1748-9326/ac1377. URL `https://iopscience.iop.org/article/10.1088/1748-9326/ac1377`.

C. L. Kibler, A. T. Trugman, D. A. Roberts, K. K. Caylor, J. C. Stella, and M. B. Singer. Evapotranspiration regulates leaf temperature and respiration in dryland vegetation, 2023.

H. Kim, B. C. McComb, S. J. K. Frey, D. M. Bell, and M. G. Betts. Forest microclimate and composition mediate long-term trends of breeding bird populations. *Global Change Biology*, 28(21):6180–6193, Nov. 2022. ISSN 1354-1013, 1365-2486. doi: 10.1111/gcb.16353. URL `https://onlinelibrary.wiley.com/doi/10.1111/gcb.16353`.

M. G. Klich. Leaf variations in Elaeagnus angustifolia related to environmental heterogeneity. *Environmental and Experimental Botany*, 44(3):171–183, Nov. 2000. ISSN 00988472. doi: 10.1016/S0098-8472(00)00056-3. URL `https://linkinghub.elsevier.com/retrieve/pii/S0098847200000563`.

J. Knauer, S. Zaehle, B. E. Medlyn, M. Reichstein, C. A. Williams, M. Migliavacca, M. G. De Kauwe, C. Werner, C. Keitel, P. Kolari, J. Limousin, and M. Linderson. Towards physiologically meaningful water-use efficiency estimates from eddy covariance data. *Global Change Biology*, 24(2):694–710, Feb. 2018. ISSN 1354-1013, 1365-2486. doi: 10.1111/gcb.13893. URL `https://onlinelibrary.wiley.com/doi/10.1111/gcb.13893`.

B. Kok. A critical consideration of the quantum yield of Chlorella-photosynthesis. *Enzymologia*, 13:1–56, 1948.

J. Kondo. Air-sea bulk transfer coefficients in diabatic conditions. *Boundary-Layer Meteorology*, 9(1):91–112, Aug. 1975. ISSN 0006-8314, 1573-1472. doi: 10.1007/BF00232256. URL `http://link.springer.com/10.1007/BF00232256`.

W. Konrad, G. Katul, and A. Roth-Nebelsick. Leaf temperature and its dependence on atmospheric CO_2 and leaf size. *Geological Journal*, 56(2):866–885, Feb. 2021. ISSN 0072-1050, 1099-1034. doi: 10.1002/gj.3757. URL `https://onlinelibrary.wiley.com/doi/10.1002/gj.3757`.

R. P. Kovach, J. B. Dunham, R. Al-Chokhachy, C. D. Snyder, B. H. Letcher, J. A. Young, E. A. Beever, G. T. Pederson, A. J. Lynch, N. P. Hitt, C. P. Konrad, K. L.

Jaeger, A. H. Rea, A. J. Sepulveda, P. M. Lambert, J. Stoker, J. J. Giersch, and C. C. Muhlfeld. An Integrated Framework for Ecological Drought across Riverscapes of North America. *BioScience*, 69(6):418–431, June 2019. ISSN 0006-3568, 1525-3244. doi: 10.1093/biosci/biz040. URL `https://academic.oup.com/bioscience/article/69/6/418/5482300`.

C. Krich, M. D. Mahecha, M. Migliavacca, M. G. De Kauwe, A. Griebel, J. Runge, and D. G. Miralles. Decoupling between ecosystem photosynthesis and transpiration: a last resort against overheating. *Environmental Research Letters*, 17(4):044013, Apr. 2022. ISSN 1748-9326. doi: 10.1088/1748-9326/ac583e. URL `https://iopscience.iop.org/article/10.1088/1748-9326/ac583e`.

B. E. Kus. Use of Restored Riparian Habitat by the Endangered Least Bell's Vireo (Vireo bellii pusillus). *Restoration Ecology*, 6(1):75–82, Mar. 1998. ISSN 1061-2971, 1526-100X. doi: 10.1046/j.1526-100x.1998.06110.x. URL `https://onlinelibrary.wiley.com/doi/abs/10.1046/j.1526-100x.1998.06110.x`.

J. Lamour, K. J. Davidson, K. S. Ely, G. Le Moguédec, J. A. Anderson, Q. Li, O. Calderón, C. D. Koven, S. J. Wright, A. P. Walker, S. P. Serbin, and A. Rogers. The effect of the vertical gradients of photosynthetic parameters on the CO_2 assimilation and transpiration of a Panamanian tropical forest. *New Phytologist*, 238(6):2345–2362, June 2023. ISSN 0028-646X, 1469-8137. doi: 10.1111/nph.18901. URL `https://nph.onlinelibrary.wiley.com/doi/10.1111/nph.18901`.

C. M. Lee, M. L. Cable, S. J. Hook, R. O. Green, S. L. Ustin, D. J. Mandl, and E. M. Middleton. An introduction to the NASA Hyperspectral InfraRed Imager (HyspIRI) mission and preparatory activities. *Remote Sensing of Environment*, 167:6–19, Sept. 2015. ISSN 00344257. doi: 10.1016/j.rse.2015.06.012. URL `https://linkinghub.elsevier.com/retrieve/pii/S0034425715300419`.

A. J. Leffler, L. E. England, and J. Naito. Vulnerability of Fremont cottonwood (Populus fremontii Wats.) individuals to xylem cavitation. *Western North American Naturalist*, 60(2):204–210, Apr. 2000.

A. Leigh, S. Sevanto, J. Close, and A. Nicotra. The influence of leaf size and shape on leaf thermal dynamics: does theory hold up under natural conditions? *Plant, Cell & Environment*, 40(2):237–248, Feb. 2017. ISSN 0140-7791, 1365-3040. doi: 10.1111/pce.12857. URL `https://onlinelibrary.wiley.com/doi/10.1111/pce.12857`.

S. Lite and J. Stromberg. Surface water and ground-water thresholds for maintaining Populus–Salix forests, San Pedro River, Arizona. *Biological Conservation*, 125(2):153–167, Sept. 2005. ISSN 00063207. doi: 10.1016/j.biocon.2005.01.020. URL `https://linkinghub.elsevier.com/retrieve/pii/S0006320705000455`.

W. H. Maes and K. Steppe. Estimating evapotranspiration and drought stress with ground-based thermal remote sensing in agriculture: a review. *Journal of Experimental Botany*, 63(13):4671–4712, Aug. 2012. ISSN 1460-2431, 0022-0957. doi: 10.1093/jxb/ers165. URL `https://academic.oup.com/jxb/article-lookup/doi/10.1093/jxb/ers165`.

J. M. Mahoney and S. B. Rood. Streamflow requirements for cottonwood seedling recruitment—An integrative model. *Wetlands*, 18(4):634–645, Dec. 1998. ISSN 0277-5212, 1943-6246. doi: 10.1007/BF03161678. URL `http://link.springer.com/10.1007/BF03161678`.

K. Mallick, D. Baldocchi, A. Jarvis, T. Hu, I. Trebs, M. Sulis, N. Bhattarai, C. Bossung, Y. Eid, J. Cleverly, J. Beringer, W. Woodgate, R. Silberstein, N. Hinko-Najera, W. S. Meyer, D. Ghent, Z. Szantoi, G. Boulet, and W. P. Kustas. Insights Into the Aerodynamic Versus Radiometric Surface Temperature Debate in Thermal-Based Evaporation Modeling. *Geophysical Research Letters*, 49(15), Aug. 2022. ISSN 0094-8276, 1944-8007. doi: 10.1029/2021GL097568. URL `https://onlinelibrary.wiley.com/doi/10.1029/2021GL097568`.

J. F. Mann. Preliminary Outline of Groundwater Conditions Near State Fish Hatchery. Technical report, Dec. 1958.

B. Markham, J. Storey, D. Williams, and J. Irons. Landsat sensor performance: history and current status. *IEEE Transactions on Geoscience and Remote Sensing*, 42(12):2691–2694, Dec. 2004. ISSN 0196-2892. doi: 10.1109/TGRS.2004.840720. URL `http://ieeexplore.ieee.org/document/1369366/`.

J. M. Mathias and A. T. Trugman. Climate change impacts plant carbon balance, increasing mean future carbon use efficiency but decreasing total forest extent at dry range edges. *Ecology Letters*, 25(2):498–508, Feb. 2022. ISSN 1461-023X, 1461-0248. doi: 10.1111/ele.13945. URL `https://onlinelibrary.wiley.com/doi/10.1111/ele.13945`.

V. Matzek, J. Stella, and P. Ropion. Development of a carbon calculator tool for riparian forest restoration. *Applied Vegetation Science*, 21(4):584–594, Oct. 2018. ISSN 14022001. doi: 10.1111/avsc.12400. URL `http://doi.wiley.com/10.1111/avsc.12400`.

M. Mauder, T. Foken, and J. Cuxart. Surface-Energy-Balance Closure over Land: A Review. *Boundary-Layer Meteorology*, 177(2-3):395–426, Dec. 2020. ISSN 0006-8314, 1573-1472. doi: 10.1007/s10546-020-00529-6. URL `https://link.springer.com/10.1007/s10546-020-00529-6`.

M. Mayes, K. K. Caylor, M. B. Singer, J. C. Stella, D. Roberts, and P. Nagler. Climate sensitivity of water use by riparian woodlands at landscape scales. *Hydrological Processes*, 34(25):4884–4903, Dec. 2020. ISSN 0885-6087, 1099-1085. doi: 10.1002/hyp. 13942. URL `https://onlinelibrary.wiley.com/doi/10.1002/hyp.13942`.

N. G. McDowell, A. P. Williams, C. Xu, W. T. Pockman, L. T. Dickman, S. Sevanto, R. Pangle, J. Limousin, J. Plaut, D. S. Mackay, J. Ogee, J. C. Domec, C. D. Allen, R. A. Fisher, X. Jiang, J. D. Muss, D. D. Breshears, S. A. Rauscher, and C. Koven. Multi-scale predictions of massive conifer mortality due to chronic temperature rise. *Nature Climate Change*, 6(3):295–300, Mar. 2016. ISSN 1758-678X, 1758-6798. doi: 10.1038/nclimate2873. URL `http://www.nature.com/articles/nclimate2873`.

N. G. McDowell, C. D. Allen, K. Anderson-Teixeira, B. H. Aukema, B. Bond-Lamberty, L. Chini, J. S. Clark, M. Dietze, C. Grossiord, A. Hanbury-Brown, G. C. Hurtt, R. B. Jackson, D. J. Johnson, L. Kueppers, J. W. Lichstein, K. Ogle, B. Poulter, T. A. M. Pugh, R. Seidl, M. G. Turner, M. Uriarte, A. P. Walker, and C. Xu. Pervasive shifts in forest dynamics in a changing world. *Science*, 368(6494):eaaz9463, May 2020. ISSN 0036-8075, 1095-9203. doi: 10.1126/science.aaz9463. URL `https://www.science.org/doi/10.1126/science.aaz9463`.

D. McFadden. Quantitative methods for analysing travel behaviour of individuals: some recent developments. Cowles Foundation Discussion Paper 474, Cowles Foundation for Research in Economics at Yale University, New Haven, Connecticut, Nov. 1977.

B. E. Medlyn, E. Dreyer, D. Ellsworth, M. Forstreuter, P. C. Harley, M. U. F. Kirschbaum, X. Le Roux, P. Montpied, J. Strassemeyer, A. Walcroft, K. Wang, and D. Loustau. Temperature response of parameters of a biochemically based model of photosynthesis. II. A review of experimental data: Temperature response of photosynthetic parameters - review. *Plant, Cell & Environment*, 25(9):1167–1179, Sept. 2002. ISSN 01407791. doi: 10.1046/j.1365-3040.2002.00891.x. URL `http://doi.wiley.com/10.1046/j.1365-3040.2002.00891.x`.

B. E. Medlyn, R. A. Duursma, D. Eamus, D. S. Ellsworth, I. C. Prentice, C. V. M. Barton, K. Y. Crous, P. De Angelis, M. Freeman, and L. Wingate. Reconciling the optimal and empirical approaches to modelling stomatal conductance. *Global Change Biology*, 17(6):2134–2144, June 2011. ISSN 13541013. doi: 10.1111/j.1365-2486.2010.02375.x. URL `https://onlinelibrary.wiley.com/doi/10.1111/j.1365-2486.2010.02375.x`.

T. Meixner, A. H. Manning, D. A. Stonestrom, D. M. Allen, H. Ajami, K. W. Blasch, A. E. Brookfield, C. L. Castro, J. F. Clark, D. J. Gochis, A. L. Flint, K. L. Neff, R. Niraula, M. Rodell, B. R. Scanlon, K. Singha, and M. A. Walvoord. Implications of projected climate change for groundwater recharge in the western United States. *Journal of Hydrology*, 534:124–138, Mar. 2016. ISSN 00221694. doi: 10.1016/j.jhydrol.2015.12.027. URL `https://linkinghub.elsevier.com/retrieve/pii/S0022169415009750`.

M. Mencuccini, S. Manzoni, and B. Christoffersen. Modelling water fluxes in plants: from tissues to biosphere. *New Phytologist*, 222(3):1207–1222, May 2019. ISSN 0028-646X, 1469-8137. doi: 10.1111/nph.15681. URL `https://onlinelibrary.wiley.com/doi/10.1111/nph.15681`.

D. M. Merritt and H. L. Bateman. Linking stream flow and groundwater to avian habitat in a desert riparian system. *Ecological Applications*, 22(7):16, 2012.

D. M. Merritt and N. L. R. Poff. Shifting dominance of riparian Populus and Tamarix along gradients of flow alteration in western North American rivers. *Ecological Applications*, 20(1):135–152, Jan. 2010. ISSN 1051-0761. doi: 10.1890/08-2251.1. URL `http://doi.wiley.com/10.1890/08-2251.1`.

S. T. Michaletz, M. D. Weiser, J. Zhou, M. Kaspari, B. R. Helliker, and B. J. Enquist. Plant Thermoregulation: Energetics, Trait–Environment Interactions, and Carbon Economics. *Trends in Ecology & Evolution*, 30(12):714–724, Dec. 2015. ISSN 01695347. doi: 10.1016/j.tree.2015.09.006. URL `https://linkinghub.elsevier.com/retrieve/pii/S0169534715002396`.

S. T. Michaletz, M. D. Weiser, N. G. McDowell, J. Zhou, M. Kaspari, B. R. Helliker, and B. J. Enquist. The energetic and carbon economic origins of leaf thermoregulation. *Nature Plants*, 2(9):16129, Sept. 2016. ISSN 2055-0278. doi: 10.1038/nplants.2016.129. URL `http://www.nature.com/articles/nplants2016129`.

B. D. Miller, K. R. Carter, S. C. Reed, T. E. Wood, and M. A. Cavaleri. Only sunlit leaves of the uppermost canopy exceed both air temperature and photosynthetic thermal optima in a wet tropical forest. *Agricultural and Forest Meteorology*, 301-302:108347, May 2021. ISSN 01681923. doi: 10.1016/j.agrformet.2021.108347. URL `https://linkinghub.elsevier.com/retrieve/pii/S0168192321000307`.

J. E. C. Missik, H. Liu, Z. Gao, M. Huang, X. Chen, E. Arntzen, D. P. Mcfarland, and B. Verbeke. Groundwater Regulates Interannual Variations in Evapotranspiration in a Riparian Semiarid Ecosystem. *Journal of Geophysical Research: Atmospheres*, 126(7), Apr. 2021. ISSN 2169-897X, 2169-8996. doi: 10.1029/2020JD033078. URL `https://onlinelibrary.wiley.com/doi/10.1029/2020JD033078`.

J. L. Monteith and M. H. Unsworth. *Principles of environmental physics: plants, animals, and the atmosphere*. Elsevier/Academic Press, Boston, 4th ed edition, 2013. ISBN 978-0-12-386910-4. OCLC: ocn858967864.

K. Moon, T. Duff, and K. Tolhurst. Sub-canopy forest winds: understanding wind profiles for fire behaviour simulation. *Fire Safety Journal*, 105:320–329, Apr. 2019. ISSN 03797112. doi: 10.1016/j.firesaf.2016.02.005. URL `https://linkinghub.elsevier.com/retrieve/pii/S0379711216300285`.

J. D. Muller, E. Rotenberg, F. Tatarinov, I. Oz, and D. Yakir. Evidence for efficient nonevaporative leaf-to-air heat dissipation in a pine forest under drought conditions. *New Phytologist*, 232(6):2254–2266, Dec. 2021. ISSN 0028-646X, 1469-8137. doi: 10.1111/nph.17742. URL `https://onlinelibrary.wiley.com/doi/10.1111/nph.17742`.

J. D. Muller, E. Rotenberg, F. Tatarinov, I. Oz, and D. Yakir. Detailed in situ leaf energy budget permits the assessment of leaf aerodynamic resistance as a key to enhance non-evaporative cooling under drought. *Plant, Cell & Environment*, page pce.14571, Feb. 2023. ISSN 0140-7791, 1365-3040. doi: 10.1111/pce.14571. URL `https://onlinelibrary.wiley.com/doi/10.1111/pce.14571`.

S. M. Munson, J. B. Bradford, and K. R. Hultine. An Integrative Ecological Drought Framework to Span Plant Stress to Ecosystem Transformation. *Ecosystems*, Sept. 2020. ISSN 1432-9840, 1435-0629. doi: 10.1007/s10021-020-00555-y. URL `http://link.springer.com/10.1007/s10021-020-00555-y`.

J. Muñoz-Sabater, E. Dutra, A. Agustí-Panareda, C. Albergel, G. Arduini, G. Balsamo, S. Boussetta, M. Choulga, S. Harrigan, H. Hersbach, B. Martens, D. G. Miralles, M. Piles, N. J. Rodríguez-Fernández, E. Zsoter, C. Buontempo, and J.-N. Thépaut. ERA5-Land: a state-of-the-art global reanalysis dataset for land applications. *Earth System Science Data*, 13(9):4349–4383, Sept. 2021. ISSN 1866-3516. doi: 10.5194/essd-13-4349-2021. URL `https://essd.copernicus.org/articles/13/4349/2021/`.

J. Nelson, N. Carvalhais, M. Cuntz, N. Delpierre, J. Knauer, J. Ogée, M. Migliavacca, M. Reichstein, and M. Jung. Coupling Water and Carbon Fluxes to Constrain Estimates of Transpiration: The TEA Algorithm. *Journal of Geophysical Research: Biogeosciences*, 123(12):3617–3632, Dec. 2018. ISSN 2169-8953, 2169-8961. doi: 10.1029/2018JG004727. URL `https://onlinelibrary.wiley.com/doi/abs/10.1029/2018JG004727`.

J. A. Nelson, O. Perez-Priego, and Z. Sha. Ecosystem Transpiration from FLUXNET, Aug. 2020a. URL `https://zenodo.org/record/3978408`. Version Number: v1.0 Type: dataset.

J. A. Nelson, O. Pérez-Priego, S. Zhou, R. Poyatos, Y. Zhang, P. D. Blanken, T. E. Gimeno, G. Wohlfahrt, A. R. Desai, B. Gioli, J. Limousin, D. Bonal, E. Paul-Limoges, R. L. Scott, A. Varlagin, K. Fuchs, L. Montagnani, S. Wolf, N. Delpierre, D. Berveiller, M. Gharun, L. Belelli Marchesini, D. Gianelle, L. Šigut, I. Mammarella, L. Siebicke, T. Andrew Black, A. Knohl, L. Hörtnagl, V. Magliulo, S. Besnard, U. Weber, N. Carvalhais, M. Migliavacca, M. Reichstein, and M. Jung. Ecosystem transpiration and evaporation: Insights from three water flux partitioning methods across FLUXNET sites. *Global Change Biology*, 26(12):6916–6930, Dec. 2020b. ISSN 1354-1013, 1365-2486. doi: 10.1111/gcb.15314. URL `https://onlinelibrary.wiley.com/doi/10.1111/gcb.15314`.

Niinemets. A review of light interception in plant stands from leaf to canopy in different plant functional types and in species with varying shade tolerance. *Ecological Research*, 25(4):693–714, July 2010. ISSN 0912-3814, 1440-1703. doi: 10.1007/s11284-010-0712-4. URL http://doi.wiley.com/10.1007/s11284-010-0712-4.

G. S. Okin, C. Dong, K. S. Willis, T. W. Gillespie, and G. M. MacDonald. The Impact of Drought on Native Southern California Vegetation: Remote Sensing Analysis Using MODIS-Derived Time Series. *Journal of Geophysical Research: Biogeosciences*, 123 (6):1927–1939, June 2018. ISSN 21698953. doi: 10.1029/2018JG004485. URL http://doi.wiley.com/10.1029/2018JG004485.

O. S. O'Sullivan, M. A. Heskel, P. B. Reich, M. G. Tjoelker, L. K. Weerasinghe, A. Penillard, L. Zhu, J. J. G. Egerton, K. J. Bloomfield, D. Creek, N. H. A. Bahar, K. L. Griffin, V. Hurry, P. Meir, M. H. Turnbull, and O. K. Atkin. Thermal limits of leaf metabolism across biomes. *Global Change Biology*, 23(1):209–223, Jan. 2017. ISSN 1354-1013, 1365-2486. doi: 10.1111/gcb.13477. URL https://onlinelibrary.wiley.com/doi/10.1111/gcb.13477.

P. R. Owen and W. R. Thomson. Heat transfer across rough surfaces. *Journal of Fluid Mechanics*, 15(3):321–334, Mar. 1963. ISSN 0022-1120, 1469-7645. doi: 10.1017/S0022112063000288. URL https://www.cambridge.org/core/product/identifier/S0022112063000288/type/journal_article.

A. Panwar, M. Renner, and A. Kleidon. Imprints of evaporative conditions and vegetation type in diurnal temperature variations. *Hydrology and Earth System Sciences*, 24 (10):4923–4942, Oct. 2020. ISSN 1607-7938. doi: 10.5194/hess-24-4923-2020. URL https://hess.copernicus.org/articles/24/4923/2020/.

S. Pau, M. Detto, Y. Kim, and C. J. Still. Tropical forest temperature thresholds for gross primary productivity. *Ecosphere*, 9(7), July 2018. ISSN 2150-8925, 2150-8925. doi: 10.1002/ecs2.2311. URL https://onlinelibrary.wiley.com/doi/10.1002/ecs2.2311.

N. E. Pettit and R. H. Froend. How important is groundwater availability and stream perenniality to riparian and floodplain tree growth? *Hydrological Processes*, 32(10): 1502–1514, May 2018. ISSN 08856087. doi: 10.1002/hyp.11510. URL http://doi.wiley.com/10.1002/hyp.11510.

A. L. Pivovaroff, V. M. Cook, and L. S. Santiago. Stomatal behaviour and stem xylem traits are coordinated for woody plant species under exceptional drought conditions. *Plant, Cell & Environment*, 41(11):2617–2626, Nov. 2018. ISSN 01407791. doi: 10.1111/pce.13367. URL http://doi.wiley.com/10.1111/pce.13367.

B. Poulter, D. Frank, P. Ciais, R. B. Myneni, N. Andela, J. Bi, G. Broquet, J. G. Canadell, F. Chevallier, Y. Y. Liu, S. W. Running, S. Sitch, and G. R. Van Der Werf.

Contribution of semi-arid ecosystems to interannual variability of the global carbon cycle. *Nature*, 509(7502):600–603, May 2014. ISSN 0028-0836, 1476-4687. doi: 10. 1038/nature13376. URL http://www.nature.com/articles/nature13376.

R. Powell, D. Roberts, P. Dennison, and L. Hess. Sub-pixel mapping of urban land cover using multiple endmember spectral mixture analysis: Manaus, Brazil. *Remote Sensing of Environment*, 106(2):253–267, Jan. 2007. ISSN 00344257. doi: 10.1016/j.rse.2006.09. 005. URL https://linkinghub.elsevier.com/retrieve/pii/S0034425706003142.

PRISM Climate Group. Monthly Climate Data, Nov. 2021. URL https://prism. oregonstate.edu.

R Core Team. R: A language and environment for statistical computing, 2020. URL https://www.R-project.org.

J. A. Ramirez-Valiente, D. Sanchez-Gomez, I. Aranda, and F. Valladares. Phenotypic plasticity and local adaptation in leaf ecophysiological traits of 13 contrasting cork oak populations under different water availabilities. *Tree Physiology*, 30(5):618–627, May 2010. ISSN 0829-318X, 1758-4469. doi: 10.1093/treephys/tpq013. URL https: //academic.oup.com/treephys/article-lookup/doi/10.1093/treephys/tpq013.

A. Rateb, B. R. Scanlon, D. R. Pool, A. Sun, Z. Zhang, J. Chen, B. Clark, C. C. Faunt, C. J. Haugh, M. Hill, C. Hobza, V. L. McGuire, M. Reitz, H. Müller Schmied, E. H. Sutanudjaja, S. Swenson, D. Wiese, Y. Xia, and W. Zell. Comparison of Groundwater Storage Changes From GRACE Satellites With Monitoring and Modeling of Major U.S. Aquifers. *Water Resources Research*, 56(12), Dec. 2020. ISSN 0043-1397, 1944-7973. doi: 10.1029/2020WR027556. URL https://onlinelibrary.wiley.com/doi/ 10.1029/2020WR027556.

P. B. Reich, M. B. Walters, D. S. Ellsworth, J. M. Vose, J. C. Volin, C. Gresham, and W. D. Bowman. Relationships of leaf dark respiration to leaf nitrogen, specific leaf area and leaf life-span: a test across biomes and functional groups. *Oecologia*, 114(4): 471–482, May 1998. ISSN 0029-8549, 1432-1939. doi: 10.1007/s004420050471. URL http://link.springer.com/10.1007/s004420050471.

E. G. Reichard, S. M. Crawford, K. S. Paybins, P. Martin, M. Land, and T. Nishikawa. Evaluation of Surface-Water/Ground-Water Interactions in the Santa Clara River Valley, Ventura County, California. Water-Resources Investigations Report 98-4208, U.S. Geological Survey, Sacramento, California, 1999. URL https://pubs.er.usgs.gov/ publication/wri984208.

A. Rigden, D. Li, and G. Salvucci. Dependence of thermal roughness length on friction velocity across land cover types: A synthesis analysis using AmeriFlux data. *Agricultural and Forest Meteorology*, 249:512–519, Feb. 2018. ISSN 01681923. doi: 10.1016/

j.agrformet.2017.06.003. URL `https://linkinghub.elsevier.com/retrieve/pii/S0168192317302022`.

D. Roberts, M. Gardner, R. Church, S. Ustin, G. Scheer, and R. Green. Mapping Chaparral in the Santa Monica Mountains Using Multiple Endmember Spectral Mixture Models. *Remote Sensing of Environment*, 65(3):267–279, Sept. 1998. ISSN 00344257. doi: 10.1016/S0034-4257(98)00037-6. URL `http://linkinghub.elsevier.com/retrieve/pii/S0034425798000376`.

D. A. Roberts, M. O. Smith, and J. B. Adams. Green vegetation, nonphotosynthetic vegetation, and soils in AVIRIS data. *Remote Sensing of Environment*, 44 (2-3):255–269, 1993. URL `http://www.sciencedirect.com/science/article/pii/003442579390020X`.

D. A. Roberts, S. L. Ustin, S. Ogunjemiyo, J. Greenberg, S. Z. Dobrowski, J. Chen, and T. M. Hinckley. Spectral and Structural Measures of Northwest Forest Vegetation at Leaf to Landscape Scales. *Ecosystems*, 7(5), Aug. 2004. ISSN 1432-9840, 1435-0629. doi: 10.1007/s10021-004-0144-5. URL `http://link.springer.com/10.1007/s10021-004-0144-5`.

D. A. Roberts, D. A. Quattrochi, G. C. Hulley, S. J. Hook, and R. O. Green. Synergies between VSWIR and TIR data for the urban environment: An evaluation of the potential for the Hyperspectral Infrared Imager (HyspIRI) Decadal Survey mission. *Remote Sensing of Environment*, 117:83–101, Feb. 2012. ISSN 00344257. doi: 10.1016/j.rse.2011.07.021. URL `https://linkinghub.elsevier.com/retrieve/pii/S0034425711002859`.

S. M. Robeson. Revisiting the recent California drought as an extreme value. *Geophysical Research Letters*, 42(16):6771–6779, Aug. 2015. ISSN 0094-8276, 1944-8007. doi: 10.1002/2015GL064593. URL `https://onlinelibrary.wiley.com/doi/abs/10.1002/2015GL064593`.

J. S. Roden and R. W. Pearcy. The effect of flutter on the temperature of poplar leaves and its implications for carbon gain. *Plant, Cell and Environment*, 16(5):571–577, June 1993. ISSN 0140-7791, 1365-3040. doi: 10.1111/j.1365-3040.1993.tb00905.x. URL `https://onlinelibrary.wiley.com/doi/10.1111/j.1365-3040.1993.tb00905.x`.

M. M. Rohde, R. Froend, and J. Howard. A Global Synthesis of Managing Groundwater Dependent Ecosystems Under Sustainable Groundwater Policy. *Groundwater*, 55(3): 293–301, May 2017. ISSN 0017467X. doi: 10.1111/gwat.12511. URL `http://doi.wiley.com/10.1111/gwat.12511`.

M. M. Rohde, J. C. Stella, D. A. Roberts, and M. B. Singer. Groundwater dependence of riparian woodlands and the disrupting effect of anthropogenically altered streamflow. *Proceedings of the National Academy of Sciences*, 118(25):e2026453118, June 2021.

ISSN 0027-8424, 1091-6490. doi: 10.1073/pnas.2026453118. URL `http://www.pnas.org/lookup/doi/10.1073/pnas.2026453118`.

S. Rood, S. Patiño, K. Coombs, and M. Tyree. Branch sacrifice: cavitation-associated drought adaptation of riparian cottonwoods. *Trees*, 14(5):0248–0257, Mar. 2000. ISSN 09311890. doi: 10.1007/s004680050010. URL `http://link.springer.com/10.1007/s004680050010`.

S. B. Rood, J. H. Braatne, and F. M. R. Hughes. Ecophysiology of riparian cottonwoods: stream flow dependency, water relations and restoration. *Tree Physiology*, 23(16): 1113–1124, Nov. 2003. ISSN 0829-318X, 1758-4469. doi: 10.1093/treephys/23.16.1113. URL `https://academic.oup.com/treephys/article-lookup/doi/10.1093/treephys/23.16.1113`.

S. B. Rood, S. G. Bigelow, and A. A. Hall. Root architecture of riparian trees: river cut-banks provide natural hydraulic excavation, revealing that cottonwoods are facultative phreatophytes. *Trees*, 25(5):907–917, Oct. 2011. ISSN 0931-1890, 1432-2285. doi: 10.1007/s00468-011-0565-7. URL `http://link.springer.com/10.1007/s00468-011-0565-7`.

K. L. Roth, P. E. Dennison, and D. A. Roberts. Comparing endmember selection techniques for accurate mapping of plant species and land cover using imaging spectrometer data. *Remote Sensing of Environment*, 127:139–152, Dec. 2012. ISSN 00344257. doi: 10.1016/j.rse.2012.08.030. URL `http://linkinghub.elsevier.com/retrieve/pii/S0034425712003495`.

R. Sabathier, M. B. Singer, J. C. Stella, D. A. Roberts, and K. K. Caylor. Vegetation responses to climatic and geologic controls on water availability in southeastern Arizona. *Environmental Research Letters*, 16(6):064029, June 2021. ISSN 1748-9326. doi: 10.1088/1748-9326/abfe8c. URL `https://iopscience.iop.org/article/10.1088/1748-9326/abfe8c`.

F. B. Salisbury and G. G. Spomer. Leaf temperatures of alpine plants in the field. *Planta*, 60(5):497–505, Sept. 1964. ISSN 0032-0935, 1432-2048. doi: 10.1007/BF01894807. URL `http://link.springer.com/10.1007/BF01894807`.

C. I. Sargeant and M. B. Singer. Sub-annual variability in historical water source use by Mediterranean riparian trees. *Ecohydrology*, 9(7):1328–1345, Oct. 2016. ISSN 19360584. doi: 10.1002/eco.1730. URL `http://doi.wiley.com/10.1002/eco.1730`.

A. N. Schaaf, P. E. Dennison, G. K. Fryer, K. L. Roth, and D. A. Roberts. Mapping Plant Functional Types at Multiple Spatial Resolutions Using Imaging Spectrometer Data. *GIScience & Remote Sensing*, 48(3):324–344, July 2011. ISSN 1548-1603. doi: 10.2747/1548-1603.48.3.324. URL `http://bellwether.metapress.com/openurl.asp?genre=article&id=doi:10.2747/1548-1603.48.3.324`.

M. L. Scott, P. B. Shafroth, and G. T. Auble. Responses of Riparian Cottonwoods to Alluvial Water Table Declines. *Environmental Management*, 23(3):347–358, Apr. 1999. ISSN 0364-152X, 1432-1009. doi: 10.1007/s002679900191. URL `http://link.springer.com/10.1007/s002679900191`.

M. L. Scott, G. C. Lines, and G. T. Auble. Channel incision and patterns of cottonwood stress and mortality along the Mojave River, California. *Journal of Arid Environments*, 44(4):399–414, Apr. 2000. ISSN 01401963. doi: 10.1006/jare.1999.0614. URL `https://linkinghub.elsevier.com/retrieve/pii/S0140196399906146`.

R. L. Scott. Using watershed water balance to evaluate the accuracy of eddy covariance evaporation measurements for three semiarid ecosystems. *Agricultural and Forest Meteorology*, 150(2):219–225, Feb. 2010. ISSN 01681923. doi: 10.1016/j.agrformet.2009.11.002. URL `https://linkinghub.elsevier.com/retrieve/pii/S0168192309002512`.

R. L. Scott. AmeriFlux BASE US-CMW Charleston Mesquite Woodland, Ver. 1-5, 2021a. URL `https://doi.org/10.17190/AMF/1660339`.

R. L. Scott. AmeriFlux BASE US-SRM Santa Rita Mesquite, Ver. 22-5, 2021b. URL `https://doi.org/10.17190/AMF/1246104`.

R. L. Scott, E. A. Edwards, W. Shuttleworth, T. E. Huxman, C. Watts, and D. C. Goodrich. Interannual and seasonal variation in fluxes of water and carbon dioxide from a riparian woodland ecosystem. *Agricultural and Forest Meteorology*, 122(1-2):65–84, Mar. 2004. ISSN 01681923. doi: 10.1016/j.agrformet.2003.09.001. URL `https://linkinghub.elsevier.com/retrieve/pii/S0168192303002211`.

R. L. Scott, G. D. Jenerette, D. L. Potts, and T. E. Huxman. Effects of seasonal drought on net carbon dioxide exchange from a woody-plant-encroached semiarid grassland. *Journal of Geophysical Research*, 114(G4):G04004, Nov. 2009. ISSN 0148-0227. doi: 10.1029/2008JG000900. URL `http://doi.wiley.com/10.1029/2008JG000900`.

R. L. Scott, J. F. Knowles, J. A. Nelson, P. Gentine, X. Li, G. Barron-Gafford, R. Bryant, and J. A. Biederman. Water Availability Impacts on Evapotranspiration Partitioning. *Agricultural and Forest Meteorology*, 297:108251, Feb. 2021. ISSN 01681923. doi: 10.1016/j.agrformet.2020.108251. URL `https://linkinghub.elsevier.com/retrieve/pii/S0168192320303531`.

P. Sellers, J. Berry, G. Collatz, C. Field, and F. Hall. Canopy reflectance, photosynthesis, and transpiration. III. A reanalysis using improved leaf models and a new canopy integration scheme. *Remote Sensing of Environment*, 42(3):187–216, Dec. 1992. ISSN 00344257. doi: 10.1016/0034-4257(92)90102-P. URL `https://linkinghub.elsevier.com/retrieve/pii/003442579290102P`.

B. Seyednasrollah, A. M. Young, K. Hufkens, T. Milliman, M. A. Friedl, S. Frolking, and A. D. Richardson. Tracking vegetation phenology across diverse biomes using Version 2.0 of the PhenoCam Dataset. *Scientific Data*, 6(1):222, Dec. 2019. ISSN 2052-4463. doi: 10.1038/s41597-019-0229-9. URL `http://www.nature.com/articles/s41597-019-0229-9`.

P. B. Shafroth, J. C. Stromberg, and D. T. Patten. Woody riparian vegetation response to different alluvial water table regimes. *Western North American Naturalist*, 60(1): 66–76, Jan. 2000. URL `https://www.jstor.org/stable/41717015`.

P. A. Sheppard. Transfer across the earth's surface and through the air above. *Quarterly Journal of the Royal Meteorological Society*, 84(361):205–224, July 1958. ISSN 00359009, 1477870X. doi: 10.1002/qj.49708436102. URL `https://onlinelibrary.wiley.com/doi/10.1002/qj.49708436102`.

M. B. Singer and K. Michaelides. Deciphering the expression of climate change within the Lower Colorado River basin by stochastic simulation of convective rainfall. *Environmental Research Letters*, 12(10):104011, Oct. 2017. ISSN 1748-9326. doi: 10.1088/1748-9326/aa8e50. URL `https://iopscience.iop.org/article/10.1088/1748-9326/aa8e50`.

M. B. Singer, J. C. Stella, S. Dufour, H. Piégay, R. J. Wilson, and L. Johnstone. Contrasting water-uptake and growth responses to drought in co-occurring riparian tree species. *Ecohydrology*, 6(3):402–412, June 2013. ISSN 19360584. doi: 10.1002/eco.1283. URL `http://doi.wiley.com/10.1002/eco.1283`.

M. B. Singer, C. I. Sargeant, H. Piégay, J. Riquier, R. J. S. Wilson, and C. M. Evans. Floodplain ecohydrology: Climatic, anthropogenic, and local physical controls on partitioning of water sources to riparian trees. *Water Resources Research*, 50(5):4490–4513, May 2014. ISSN 00431397. doi: 10.1002/2014WR015581. URL `http://doi.wiley.com/10.1002/2014WR015581`.

G. Skiadaresis, J. Schwarz, K. Stahl, and J. Bauhus. Groundwater extraction reduces tree vitality, growth and xylem hydraulic capacity in Quercus robur during and after drought events. *Scientific Reports*, 11(1):5149, Dec. 2021. ISSN 2045-2322. doi: 10.1038/s41598-021-84322-6. URL `http://www.nature.com/articles/s41598-021-84322-6`.

M. O. Smith, S. L. Ustin, J. B. Adams, and A. R. Gillespie. Vegetation in deserts: I. A regional measure of abundance from multispectral images. *Remote Sensing of Environment*, 31(1):1–26, Jan. 1990. ISSN 00344257. doi: 10.1016/0034-4257(90)90074-V. URL `http://linkinghub.elsevier.com/retrieve/pii/003442579090074V`.

J. Song, G. R. Miller, A. T. Cahill, L. M. T. Aparecido, and G. W. Moore. Modeling Profiles of Micrometeorological Variables in a Tropical Premontane Rainforest Using

Multi-Layered CLM (CLM-ML). *Journal of Advances in Modeling Earth Systems*, 13(5), May 2021. ISSN 1942-2466, 1942-2466. doi: 10.1029/2020MS002259. URL `https://onlinelibrary.wiley.com/doi/10.1029/2020MS002259`.

J. S. Sperry, M. D. Venturas, W. R. L. Anderegg, M. Mencuccini, D. S. Mackay, Y. Wang, and D. M. Love. Predicting stomatal responses to the environment from the optimization of photosynthetic gain and hydraulic cost: A stomatal optimization model. *Plant, Cell & Environment*, 40(6):816–830, June 2017. ISSN 01407791. doi: 10.1111/pce. 12852. URL `https://onlinelibrary.wiley.com/doi/10.1111/pce.12852`.

S. C. Stark, V. Leitold, J. L. Wu, M. O. Hunter, C. V. de Castilho, F. R. C. Costa, S. M. McMahon, G. G. Parker, M. T. Shimabukuro, M. A. Lefsky, M. Keller, L. F. Alves, J. Schietti, Y. E. Shimabukuro, D. O. Brandão, T. K. Woodcock, N. Higuchi, P. B. de Camargo, R. C. de Oliveira, and S. R. Saleska. Amazon forest carbon dynamics predicted by profiles of canopy leaf area and light environment. *Ecology Letters*, 15(12): 1406–1414, Dec. 2012. ISSN 1461023X. doi: 10.1111/j.1461-0248.2012.01864.x. URL `https://onlinelibrary.wiley.com/doi/10.1111/j.1461-0248.2012.01864.x`.

J. C. Stella and J. J. Battles. How do riparian woody seedlings survive seasonal drought? *Oecologia*, 164(3):579–590, Nov. 2010. ISSN 0029-8549, 1432-1939. doi: 10.1007/s00442-010-1657-6. URL `http://link.springer.com/10.1007/s00442-010-1657-6`.

J. C. Stella, J. J. Battles, B. K. Orr, and J. R. McBride. Synchrony of Seed Dispersal, Hydrology and Local Climate in a Semi-arid River Reach in California. *Ecosystems*, 9(7): 1200–1214, Nov. 2006. ISSN 1432-9840, 1435-6629. doi: 10.1007/s10021-005-0138-y. URL `http://link.springer.com/10.1007/s10021-005-0138-y`.

J. C. Stella, J. J. Battles, J. R. McBride, and B. K. Orr. Riparian Seedling Mortality from Simulated Water Table Recession, and the Design of Sustainable Flow Regimes on Regulated Rivers. *Restoration Ecology*, 18:284–294, Nov. 2010. ISSN 10612971. doi: 10.1111/j.1526-100X.2010.00651.x. URL `http://doi.wiley.com/10.1111/j.1526-100X.2010.00651.x`.

G. L. Stephens and T. L'Ecuyer. The Earth's energy balance. *Atmospheric Research*, 166:195–203, Dec. 2015. ISSN 01698095. doi: 10.1016/j.atmosres.2015.06.024. URL `https://linkinghub.elsevier.com/retrieve/pii/S0169809515002070`.

C. Still, R. Powell, D. Aubrecht, Y. Kim, B. Helliker, D. Roberts, A. D. Richardson, and M. Goulden. Thermal imaging in plant and ecosystem ecology: applications and challenges. *Ecosphere*, 10(6), June 2019a. ISSN 2150-8925, 2150-8925. doi: 10.1002/ ecs2.2768. URL `https://onlinelibrary.wiley.com/doi/abs/10.1002/ecs2.2768`.

C. J. Still, A. Sibley, G. Page, F. C. Meinzer, and S. Sevanto. When a cuvette is not a canopy: A caution about measuring leaf temperature during gas exchange measurements. *Agricultural and Forest Meteorology*, 279:107737, Dec. 2019b. ISSN 01681923.

doi: 10.1016/j.agrformet.2019.107737. URL `https://linkinghub.elsevier.com/retrieve/pii/S0168192319303533`.

C. J. Still, B. Rastogi, G. F. M. Page, D. M. Griffith, A. Sibley, M. Schulze, L. Hawkins, S. Pau, M. Detto, and B. R. Helliker. Imaging canopy temperature: shedding (thermal) light on ecosystem processes. *New Phytologist*, 230(5):1746–1753, June 2021. ISSN 0028-646X, 1469-8137. doi: 10.1111/nph.17321. URL `https://onlinelibrary.wiley.com/doi/10.1111/nph.17321`.

C. J. Still, G. Page, B. Rastogi, D. M. Griffith, D. M. Aubrecht, Y. Kim, S. P. Burns, C. V. Hanson, H. Kwon, L. Hawkins, F. C. Meinzer, S. Sevanto, D. Roberts, M. Goulden, S. Pau, M. Detto, B. Helliker, and A. D. Richardson. No evidence of canopy-scale leaf thermoregulation to cool leaves below air temperature across a range of forest ecosystems. *Proceedings of the National Academy of Sciences*, 119(38):e2205682119, Sept. 2022. ISSN 0027-8424, 1091-6490. doi: 10.1073/pnas.2205682119. URL `https://pnas.org/doi/full/10.1073/pnas.2205682119`.

J. Stover, E. Keller, T. Dudley, and E. Langendoen. Fluvial Geomorphology, Root Distribution, and Tensile Strength of the Invasive Giant Reed, Arundo Donax and Its Role on Stream Bank Stability in the Santa Clara River, Southern California. *Geosciences*, 8(8):304, Aug. 2018. ISSN 2076-3263. doi: 10.3390/geosciences8080304. URL `http://www.mdpi.com/2076-3263/8/8/304`.

P. C. Stoy, M. Mauder, T. Foken, B. Marcolla, E. Boegh, A. Ibrom, M. A. Arain, A. Arneth, M. Aurela, C. Bernhofer, A. Cescatti, E. Dellwik, P. Duce, D. Gianelle, E. van Gorsel, G. Kiely, A. Knohl, H. Margolis, H. McCaughey, L. Merbold, L. Montagnani, D. Papale, M. Reichstein, M. Saunders, P. Serrano-Ortiz, M. Sottocornola, D. Spano, F. Vaccari, and A. Varlagin. A data-driven analysis of energy balance closure across FLUXNET research sites: The role of landscape scale heterogeneity. *Agricultural and Forest Meteorology*, 171-172:137–152, Apr. 2013. ISSN 01681923. doi: 10.1016/j.agrformet.2012.11.004. URL `https://linkinghub.elsevier.com/retrieve/pii/S0168192312003413`.

P. C. Stoy, T. S. El-Madany, J. B. Fisher, P. Gentine, T. Gerken, S. P. Good, A. Klosterhalfen, S. Liu, D. G. Miralles, O. Perez-Priego, A. J. Rigden, T. H. Skaggs, G. Wohlfahrt, R. G. Anderson, A. M. J. Coenders-Gerrits, M. Jung, W. H. Maes, I. Mammarella, M. Mauder, M. Migliavacca, J. A. Nelson, R. Poyatos, M. Reichstein, R. L. Scott, and S. Wolf. Reviews and syntheses: Turning the challenges of partitioning ecosystem evaporation and transpiration into opportunities. *Biogeosciences*, 16(19):3747–3775, Oct. 2019. ISSN 1726-4189. doi: 10.5194/bg-16-3747-2019. URL `https://bg.copernicus.org/articles/16/3747/2019/`.

J. Stromberg. Root patterns and hydrogeomorphic niches of riparian plants in the American Southwest. *Journal of Arid Environments*, 94:1–9, July 2013. ISSN

01401963. doi: 10.1016/j.jaridenv.2013.02.004. URL `https://linkinghub.elsevier.com/retrieve/pii/S0140196313000220`.

J. C. Stromberg and D. M. Merritt. Riparian plant guilds of ephemeral, intermittent and perennial rivers. *Freshwater Biology*, 61(8):1259–1275, Aug. 2016. ISSN 00465070. doi: 10.1111/fwb.12686. URL `http://doi.wiley.com/10.1111/fwb.12686`.

J. C. Stromberg, S. D. Wilkins, and J. A. Tress. Vegetation-Hydrology Models: Implications for Management of Prosopis Velutina (Velvet Mesquite) Riparian Ecosystems. *Ecological Applications*, 3(2):307–314, May 1993. ISSN 10510761. doi: 10.2307/1941833. URL `http://doi.wiley.com/10.2307/1941833`.

J. C. Stromberg, R. Tiller, and B. Richter. Effects of Groundwater Decline on Riparian Vegetation of Semiarid Regions: The San Pedro, Arizona. *Ecological Applications*, 6 (1):113–131, Feb. 1996. ISSN 10510761. doi: 10.2307/2269558. URL `http://doi.wiley.com/10.2307/2269558`.

B. N. Sulman, D. T. Roman, T. M. Scanlon, L. Wang, and K. A. Novick. Comparing methods for partitioning a decade of carbon dioxide and water vapor fluxes in a temperate forest. *Agricultural and Forest Meteorology*, 226-227:229–245, Oct. 2016. ISSN 01681923. doi: 10.1016/j.agrformet.2016.06.002. URL `https://linkinghub.elsevier.com/retrieve/pii/S0168192316302994`.

E. Sumargo, H. McMillan, R. Weihs, C. J. Ellis, A. M. Wilson, and F. M. Ralph. A soil moisture monitoring network to assess controls on runoff generation during atmospheric river events. *Hydrological Processes*, 35(1), Jan. 2021. ISSN 0885-6087, 1099-1085. doi: 10.1002/hyp.13998. URL `https://onlinelibrary.wiley.com/doi/10.1002/hyp.13998`.

T. L. Swetnam, P. D. Brooks, H. R. Barnard, A. A. Harpold, and E. L. Gallo. Topographically driven differences in energy and water constrain climatic control on forest carbon sequestration. *Ecosphere*, 8(4):e01797, Apr. 2017. ISSN 21508925. doi: 10.1002/ecs2.1797. URL `http://doi.wiley.com/10.1002/ecs2.1797`.

X. Tai, D. S. Mackay, J. S. Sperry, P. Brooks, W. R. L. Anderegg, L. B. Flanagan, S. B. Rood, and C. Hopkinson. Distributed Plant Hydraulic and Hydrological Modeling to Understand the Susceptibility of Riparian Woodland Trees to Drought-Induced Mortality. *Water Resources Research*, 54(7):4901–4915, July 2018. ISSN 0043-1397, 1944-7973. doi: 10.1029/2018WR022801. URL `https://onlinelibrary.wiley.com/doi/abs/10.1029/2018WR022801`.

R. G. Taylor, B. Scanlon, P. Döll, M. Rodell, R. van Beek, Y. Wada, L. Longuevergne, M. Leblanc, J. S. Famiglietti, M. Edmunds, L. Konikow, T. R. Green, J. Chen, M. Taniguchi, M. F. P. Bierkens, A. MacDonald, Y. Fan, R. M. Maxwell, Y. Yechieli, J. J. Gurdak, D. M. Allen, M. Shamsudduha, K. Hiscock, P. J.-F. Yeh, I. Holman,

and H. Treidel. Ground water and climate change. *Nature Climate Change*, 3(4): 322–329, Apr. 2013. ISSN 1758-678X, 1758-6798. doi: 10.1038/nclimate1744. URL `http://www.nature.com/articles/nclimate1744`.

A. S. Thom. Momentum, mass and heat exchange of vegetation. *Quarterly Journal of the Royal Meteorological Society*, 98(415):124–134, Jan. 1972. ISSN 00359009, 1477870X. doi: 10.1002/qj.49709841510. URL `https://onlinelibrary.wiley.com/doi/10.1002/qj.49709841510`.

B. E. Thomas and D. R. Pool. Trends in Streamflow of the San Pedro River, Southeastern Arizona, and Regional Trends in Precipitation and Streamflow in Southeastern Arizona and Southwestern New Mexico. Professional Paper 1712, U.S. Geological Survey, Reston, Virginia, 2006.

B. F. Thomas, J. S. Famiglietti, F. W. Landerer, D. N. Wiese, N. P. Molotch, and D. F. Argus. GRACE Groundwater Drought Index: Evaluation of California Central Valley groundwater drought. *Remote Sensing of Environment*, 198:384–392, Sept. 2017. ISSN 00344257. doi: 10.1016/j.rse.2017.06.026. URL `https://linkinghub.elsevier.com/retrieve/pii/S0034425717302869`.

S. Tian, G. Zheng, J. U. Eitel, and Q. Zhang. A Lidar-Based 3-D Photosynthetically Active Radiation Model Reveals the Spatiotemporal Variations of Forest Sunlit and Shaded Leaves. *Remote Sensing*, 13(5):1002, Mar. 2021. ISSN 2072-4292. doi: 10.3390/rs13051002. URL `https://www.mdpi.com/2072-4292/13/5/1002`.

A. T. Trugman, M. Detto, M. K. Bartlett, D. Medvigy, W. R. L. Anderegg, C. Schwalm, B. Schaffer, and S. W. Pacala. Tree carbon allocation explains forest drought-kill and recovery patterns. *Ecology Letters*, 21(10):1552–1560, Oct. 2018. ISSN 1461023X. doi: 10.1111/ele.13136. URL `http://doi.wiley.com/10.1111/ele.13136`.

A. T. Trugman, L. D. L. Anderegg, B. T. Wolfe, B. Birami, N. K. Ruehr, M. Detto, M. K. Bartlett, and W. R. L. Anderegg. Climate and plant trait strategies determine tree carbon allocation to leaves and mediate future forest productivity. *Global Change Biology*, 25(10):3395–3405, Oct. 2019. ISSN 1354-1013, 1365-2486. doi: 10.1111/gcb.14680. URL `https://onlinelibrary.wiley.com/doi/10.1111/gcb.14680`.

T. Twine, W. Kustas, J. Norman, D. Cook, P. Houser, T. Meyers, J. Prueger, P. Starks, and M. Wesely. Correcting eddy-covariance flux underestimates over a grassland. *Agricultural and Forest Meteorology*, 103(3):279–300, June 2000. ISSN 01681923. doi: 10.1016/S0168-1923(00)00123-4. URL `https://linkinghub.elsevier.com/retrieve/pii/S0168192300001234`.

D. Uni, E. Sheffer, G. Winters, A. C. Lima, H. Fox, and T. Klein. Peak photosynthesis at summer midday in Acacia trees growing in a hyper-arid habitat. *Trees*, Oct. 2022.

ISSN 0931-1890, 1432-2285. doi: 10.1007/s00468-022-02344-7. URL `https://link.springer.com/10.1007/s00468-022-02344-7`.

United Water Conservation District. Groundwater and Surface Water Conditions Report - 2015. Open-File Report 2017-01, Oxnard, California, Mar. 2017. URL `https://www.unitedwater.org/key-documents/#groundwater-conditions`.

U.S. Drought Monitor. Time series for the Santa Clara River watershed. `https://https://droughtmonitor.unl.edu`, 2021. Accessed: 2021-04-08.

USDA. National Agricultural Imagery Program. Aerial imagery of the Santa Clara River watershed. `https://nrcs.app.box.com/v/naip/folder/17936490251`, 2012. Accessed: 2021-04-08.

USDA. The PLANTS database. National Plant Data Team, Greensboro, NC. `https://plants.sc.egov.usda.gov/java`, 2021. Accessed: 2021-04-08.

A. F. Van Loon. Hydrological drought explained. *Wiley Interdisciplinary Reviews: Water*, 2(4):359–392, July 2015. ISSN 20491948. doi: 10.1002/wat2.1085. URL `http://doi.wiley.com/10.1002/wat2.1085`.

A. Verhoef, H. De Bruin, and B. Van Den Hurk. Some Practical Notes on the Parameter kB-1 for Sparse Vegetation. *Journal of Applied Meteorology*, 36(5):560–572, May 1997. URL `https://www.jstor.org/stable/26182252`.

S. M. Vicente-Serrano, S. Beguería, and J. I. López-Moreno. A Multiscalar Drought Index Sensitive to Global Warming: The Standardized Precipitation Evapotranspiration Index. *Journal of Climate*, 23(7):1696–1718, Apr. 2010. ISSN 1520-0442, 0894-8755. doi: 10.1175/2009JCLI2909.1. URL `http://journals.ametsoc.org/doi/10.1175/2009JCLI2909.1`.

N. Vinod, M. Slot, I. R. McGregor, E. M. Ordway, M. N. Smith, T. C. Taylor, L. Sack, T. N. Buckley, and K. J. Anderson-Teixeira. Thermal sensitivity across forest vertical profiles: patterns, mechanisms, and ecological implications. *New Phytologist*, 237(1): 22–47, Jan. 2023. ISSN 0028-646X, 1469-8137. doi: 10.1111/nph.18539. URL `https://onlinelibrary.wiley.com/doi/10.1111/nph.18539`.

M. M. Warter, M. B. Singer, M. O. Cuthbert, D. Roberts, K. K. Caylor, R. Sabathier, and J. Stella. Drought onset and propagation into soil moisture and grassland vegetation responses during the 2012–2019 major drought in Southern California. *Hydrology and Earth System Sciences*, 25(6):3713–3729, July 2021. ISSN 1607-7938. doi: 10.5194/hess-25-3713-2021. URL `https://hess.copernicus.org/articles/25/3713/2021/`.

D. A. Way, C. Holly, D. Bruhn, M. C. Ball, and O. K. Atkin. Diurnal and seasonal variation in light and dark respiration in field-grown Eucalyptus pauciflora. *Tree*

Physiology, 35(8):840–849, Aug. 2015. ISSN 0829-318X, 1758-4469. doi: 10.1093/treephys/tpv065. URL `https://academic.oup.com/treephys/article-lookup/doi/10.1093/treephys/tpv065`.

E. B. Wetherley, D. A. Roberts, and J. P. McFadden. Mapping spectrally similar urban materials at sub-pixel scales. *Remote Sensing of Environment*, 195:170–183, June 2017. ISSN 00344257. doi: 10.1016/j.rse.2017.04.013. URL `https://linkinghub.elsevier.com/retrieve/pii/S0034425717301633`.

A. P. Williams, E. R. Cook, J. E. Smerdon, B. I. Cook, J. T. Abatzoglou, K. Bolles, S. H. Baek, A. M. Badger, and B. Livneh. Large contribution from anthropogenic warming to an emerging North American megadrought. *Science*, 368(6488):314–318, Apr. 2020. ISSN 0036-8075, 1095-9203. doi: 10.1126/science.aaz9600. URL `https://www.sciencemag.org/lookup/doi/10.1126/science.aaz9600`.

J. Williams, J. C. Stella, S. L. Voelker, A. M. Lambert, L. M. Pelletier, J. E. Drake, J. M. Friedman, D. A. Roberts, and M. B. Singer. Local groundwater decline exacerbates response of dryland riparian woodlands to climatic drought. *Global Change Biology*, 28 (22):6771–6788, Nov. 2022. ISSN 1354-1013, 1365-2486. doi: 10.1111/gcb.16376. URL `https://onlinelibrary.wiley.com/doi/10.1111/gcb.16376`.

A. Wolf, W. R. L. Anderegg, and S. W. Pacala. Optimal stomatal behavior with competition for water and risk of hydraulic impairment. *Proceedings of the National Academy of Sciences*, 113(46), Nov. 2016. ISSN 0027-8424, 1091-6490. doi: 10.1073/pnas.1615144113. URL `https://pnas.org/doi/full/10.1073/pnas.1615144113`.

C. Wolf, D. M. Bell, H. Kim, M. P. Nelson, M. Schulze, and M. G. Betts. Temporal consistency of undercanopy thermal refugia in old-growth forest. *Agricultural and Forest Meteorology*, 307:108520, Sept. 2021. ISSN 01681923. doi: 10.1016/j.agrformet.2021.108520. URL `https://linkinghub.elsevier.com/retrieve/pii/S0168192321002045`.

I. J. Wright, N. Dong, V. Maire, I. C. Prentice, M. Westoby, S. Díaz, R. V. Gallagher, B. F. Jacobs, R. Kooyman, E. A. Law, M. R. Leishman, Niinemets, P. B. Reich, L. Sack, R. Villar, H. Wang, and P. Wilf. Global climatic drivers of leaf size. *Science*, 357(6354):917–921, Sept. 2017. ISSN 0036-8075, 1095-9203. doi: 10.1126/science.aal4760. URL `https://www.science.org/doi/10.1126/science.aal4760`.

R. Yang and M. A. Friedl. Determination of Roughness Lengths for Heat and Momentum Over Boreal Forests. *Boundary-Layer Meteorology*, 107(3):581–603, June 2003. ISSN 0006-8314, 1573-1472. doi: 10.1023/A:1022880530523. URL `http://link.springer.com/10.1023/A:1022880530523`.

X. Yang, R. Li, A. Jablonski, A. Stovall, J. Kim, K. Yi, Y. Ma, D. Beverly, R. Phillips, K. Novick, X. Xu, and M. Lerdau. Leaf angle as a leaf and canopy trait: Rejuvenating

its role in ecology with new technology. *Ecology Letters*, page ele.14215, Apr. 2023. ISSN 1461-023X, 1461-0248. doi: 10.1111/ele.14215. URL https://onlinelibrary.wiley.com/doi/10.1111/ele.14215.

C. Yi. Momentum Transfer within Canopies. *Journal of Applied Meteorology and Climatology*, 47(1):262–275, Jan. 2008. ISSN 1558-8432, 1558-8424. doi: 10.1175/2007JAMC1667.1. URL https://journals.ametsoc.org/doi/10.1175/2007JAMC1667.1.

A. M. Young, M. A. Friedl, B. Seyednasrollah, E. Beamesderfer, C. M. Carrillo, X. Li, M. Moon, M. A. Arain, D. D. Baldocchi, P. D. Blanken, G. Bohrer, S. P. Burns, H. Chu, A. R. Desai, T. J. Griffis, D. Y. Hollinger, M. E. Litvak, K. Novick, R. L. Scott, A. E. Suyker, J. Verfaillie, J. D. Wood, and A. D. Richardson. Seasonality in aerodynamic resistance across a range of North American ecosystems. *Agricultural and Forest Meteorology*, 310:108613, Nov. 2021. ISSN 01681923. doi: 10.1016/j.agrformet.2021.108613. URL https://linkinghub.elsevier.com/retrieve/pii/S0168192321002999.

X. Zeng and R. E. Dickinson. Effect of Surface Sublayer on Surface Skin Temperature and Fluxes. *Journal of Climate*, 11(4):537–550, Apr. 1998. ISSN 0894-8755, 1520-0442. doi: 10.1175/1520-0442(1998)011⟨0537:EOSSOS⟩2.0.CO;2. URL http://journals.ametsoc.org/doi/10.1175/1520-0442(1998)011<0537:EOSSOS>2.0.CO;2.

Z. Zhu, M. A. Wulder, D. P. Roy, C. E. Woodcock, M. C. Hansen, V. C. Radeloff, S. P. Healey, C. Schaaf, P. Hostert, P. Strobl, J.-F. Pekel, L. Lymburner, N. Pahlevan, and T. A. Scambos. Benefits of the free and open Landsat data policy. *Remote Sensing of Environment*, 224:382–385, Apr. 2019. ISSN 00344257. doi: 10.1016/j.rse.2019.02.016. URL https://linkinghub.elsevier.com/retrieve/pii/S0034425719300719.

S. Zilitinkevich. Non-local Turbulent Transport: Pollution Dispersion Aspects Of Coherent Structure Of Connective Flows. In *WIT Transactions on Ecology and the Environment*, pages 53–60, Porto Carras, Greece, Sept. 1995. doi: 10.2495/AIR950071. URL http://library.witpress.com/viewpaper.asp?pcode=AIR95-007-1.

R. C. Zimmerman. Plant Ecology of an Arid Basin: Tres Alamos-Redington Area, Southeastern Arizona. Geological Survey Professional Paper 485-D, U.S. Department of the Interior, Washington, DC, 1969. URL https://pubs.usgs.gov/pp/0485d/report.pdf.

M. A. Zwieniecki, C. K. Boyce, and N. M. Holbrook. Hydraulic limitations imposed by crown placement determine final size and shape of Quercus rubra L. leaves. *Plant, Cell and Environment*, 27(3):357–365, Feb. 2004. ISSN 0140-7791, 1365-3040. doi: 10.1111/j.1365-3040.2003.01153.x. URL https://onlinelibrary.wiley.com/doi/10.1111/j.1365-3040.2003.01153.x.